

# Study of background gas collisions in atomic traps

by

Janelle Van Dongen

A THESIS SUBMITTED IN PARTIAL FULFILMENT OF  
THE REQUIREMENTS FOR THE DEGREE OF

Doctor of Philosophy

in

The Faculty of Graduate and Postdoctoral Studies

(Physics)

The University Of British Columbia

June, 2014

© Janelle Van Dongen 2014

# Abstract

This thesis describes an investigation and application of the loss of laser-cooled atoms from a trap induced by background collisions. The loss rate constant depends on the density of background gas and the velocity averaged collisional loss cross section due to collisions. The velocity averaged collisional loss cross section can be calculated and its dependence on trap depth was verified using a magneto-optical trap. This verification involved measurements of the loss rate constant for a quadrupole magnetic and a magneto-optical trap and measurement of the density of Ar background gas using a residual gas analyzer. The second part of the thesis focuses on an application of these measurements of the loss rate constant to measure the pressure of the background gas. The experimental progress to date on the atom pressure sensor is provided.

# Preface

The work described in chapter 3 led to the publication titled ‘Trap-depth determination from residual gas collisions’ published in *Phys. Rev. A* 84, 022708 (2011). My contribution to the publication was experimental setup, taking data and correcting the manuscript after the reviewer’s initial comments. Fig. 1.6 was produced by Dr. Daniel Steck. Fig. 2.4, 3.2 - 3.5, and 3.8 - 3.13 are reproduced from that publication and were originally made by Dr. James Booth. Tables 3.1 and 3.2 are also from this publication and data analysis performed for these tables was performed by Dr. James Booth.

Chapters 4-7 describe work leading to a pressure sensor using trapped atoms. I was directly involved in the experimental design of the apparatus, ordering and assembly of the apparatus, and taking and analyzing precursory data. Fig. 4.4 is attributed to MKS Instruments and is used with permission. Fig. 6.2 was produced by an image processing code written by Dr. James Booth.

Appendix A led to a publication titled ‘Magneto-optical trap loading rate dependence on trap depth and vapor density’ published in *JOSA B*, Vol. 29, Issue 3, pp. 475-483 (2012). I was listed as an author for background support on the experimental apparatus. The figures and tables in the appendix are reproduced from that work and were originally made by Dr. James Booth.

# Table of Contents

<b>Abstract</b>	ii
<b>Preface</b>	iii
<b>Table of Contents</b>	iv
<b>List of Tables</b>	vii
<b>List of Figures</b>	viii
<b>List of Abbreviations</b>	xi
<b>Acknowledgements</b>	xii
<b>1 Introduction</b>	1
1.1 Thesis overview	1
1.2 Atomic traps	2
1.2.1 3D magneto-optical trap	3
1.2.2 Magnetic traps	7
1.3 Trap dynamics	12
1.3.1 Magneto-optical trap dynamics	12
1.3.2 Magnetic trap dynamics	16
<b>2 Background gas collision induced loss</b>	18
2.1 A brief review of necessary scattering theory	18
2.2 The velocity averaged collisional loss cross section	23
2.2.1 Calculation of $\langle \sigma_{\text{loss}} v_i \rangle_{X,i}$	23
2.2.2 Convergence criteria	27
2.2.3 Interaction potential	28
2.2.4 The dependence of $\langle \sigma_{\text{loss}} v_i \rangle_{X,i}$ on trap depth, $U$	30

*Table of Contents*

---

<b>3</b>	<b>Experimental verification of the dependence of the loss cross section on trap depth</b>	34
3.1	Experimental apparatus	34
3.2	Measurement of $\langle\sigma v_{\text{Ar}}\rangle_{^{87}\text{Rb},^{40}\text{Ar}}$	36
3.2.1	Measurement of $\Gamma$ for a MOT	37
3.2.2	Measurement of $\Gamma$ for a magnetic trap	37
3.2.3	Results of $\Gamma$ vs $n_{\text{Ar}}$ measurement	39
3.3	MOT trap depth determination by the ‘catalysis method’	43
3.4	Comparison of measurement with theory	49
3.4.1	Magnetic trap data	49
3.4.2	Magneto-optical trap data	51
3.4.3	Discussion	52
3.5	Proposal for a trap depth measurement technique	53
<b>4</b>	<b>Proposal for a cold atom based pressure sensor</b>	57
4.1	Pressure gauges	58
4.1.1	Capacitance diaphragm gauge	58
4.1.2	Spinning rotor gauge	60
4.1.3	Bayard-Alpert ionization gauge	62
4.1.4	Residual gas analyzer	64
4.1.5	Pirani gauge	65
4.2	Existing pressure standards	65
4.2.1	Static expansion method	65
4.2.2	Orifice flow method	66
4.3	A proposed density/pressure standard using trapped atoms	68
4.3.1	Existing proposals for total vacuum pressure measurement using trapped atoms	72
4.3.2	Magneto-optical trap versus magnetic-trap for a pressure sensor	73
4.3.3	Estimated uncertainty	74
<b>5</b>	<b>Experimental apparatus for the pressure sensor experiment</b>	76
5.1	High vacuum pumps	80
5.2	2D MOT section	81
5.2.1	2D MOT chamber region	81
5.2.2	2D MOT coils	82
5.3	3D MOT section	87
5.4	UHV pumps and diagnostics	87
5.5	Vacuum apparatus assembly	89
5.6	Bakeout Procedure	92

*Table of Contents*

---

5.6.1	Oven . . . . .	92
5.6.2	Pre-bake preparation . . . . .	93
5.6.3	Baking . . . . .	94
5.6.4	Cooling . . . . .	95
5.7	Rb release from the ampoule . . . . .	95
5.8	Optics . . . . .	97
5.8.1	2D MOT optics . . . . .	99
5.8.2	3D MOT optics . . . . .	100
<b>6</b>	<b>2D MOT characterization . . . . .</b>	<b>104</b>
6.1	Rubidium atomic beam divergence characterization . . . . .	104
6.2	Atomic speed distribution characterization . . . . .	105
<b>7</b>	<b>Loss rate measurements in a 3D MOT . . . . .</b>	<b>112</b>
7.1	Loss rate variation with the total pressure of residual back-ground gas . . . . .	112
7.2	Loss rate variation with the pressure of Ar background gas . . . . .	114
<b>8</b>	<b>Future outlook and conclusions . . . . .</b>	<b>118</b>
8.1	Future outlook . . . . .	118
8.1.1	Magnetic trapping coils . . . . .	118
8.1.2	NIST gauges . . . . .	120
8.1.3	Technical challenges . . . . .	121
8.2	Conclusions . . . . .	121
	<b>Bibliography . . . . .</b>	<b>123</b>
 <b>Appendices</b>		
<b>A</b>	<b>Loading rate investigation . . . . .</b>	<b>132</b>
A.1	Reif model . . . . .	132
A.2	Experimental observables . . . . .	133
A.3	The dependence of loading rate on MOT trap depth . . . . .	134
A.4	Trap depth determination using loading rates . . . . .	135
A.5	The dependence of loading rate on rubidium density . . . . .	136
A.6	Determination of $b$ . . . . .	138

# List of Tables

3.1	Measurements of the velocity averaged collisional loss cross section, $\langle\sigma v_{\text{Ar}}\rangle_{^{87}\text{Rb},^{40}\text{Ar}}$ , for various MOT pump intensities and detunings. The velocity averaged collisional loss cross section is the slope of the linear fit to measurements of the loss rate constant $\Gamma$ of a $^{87}\text{Rb}$ MOT versus the density of $^{40}\text{Ar}$ in the background gas. The values of the velocity averaged cross section and errors quoted are from the linear fit results.	55
3.2	3D MOT trap depths for various pump detunings and intensities. The trap depths, $U_{\text{cat}}$ , were determined using the catalysis method described in section 3.3. As a comparison the trap depths were also obtained by fitting the numerically calculated $\langle\sigma v_{\text{Ar}}\rangle_{^{87}\text{Rb},^{40}\text{Ar}}$ vs $U$ and then determining trap depth from measured values of $\langle\sigma v_{\text{Ar}}\rangle_{^{87}\text{Rb},^{40}\text{Ar}}$ . Trap depths determined numerically are denoted $U_{\langle\sigma v\rangle}$ .	55
4.1	Percentage changes for the value of $\langle\sigma_{\text{loss}} v_{\text{Ar}}\rangle_{^{87}\text{Rb},^{40}\text{Ar}}$ due to 10, 50 and 100% increases in the values of $C_6$ , well depth $\epsilon$ , temperature ( $T$ ), and trap depth ( $U$ ). While one parameter changed the other parameters were held fixed at $T = 294$ K, $C_6 = 336.4$ a.u., $\epsilon = 50\text{cm}^{-1}$ , and $U = 5$ mK	74
5.1	Optical Components used in Fig. 5.9	99
A.1	MOT trap depths measured using the ‘catalysis method’ for various MOT settings.	136
A.2	Parameters used in the calculation of $b$ , the proportionality constant between the capture velocity $v_c$ and the escape velocity $v_e$ .	139

# List of Figures

1.1	A magneto-optical trap. . . . .	4
1.2	Magnetic field lines from coils in anti-Helmholtz configuration. . . . .	5
1.3	Principle of how a magneto-optical trap traps atoms. . . . .	6
1.4	The energy levels of the D <sub>2</sub> transition for <sup>87</sup> Rb. . . . .	7
1.5	The energy levels of the D <sub>2</sub> transition for <sup>85</sup> Rb. . . . .	8
1.6	Hyperfine energies as a function of magnetic field for <sup>87</sup> Rb in its 5 <sup>2</sup> S <sub>1/2</sub> ground state. . . . .	10
1.7	Explanation of an ‘RF knife’. . . . .	12
1.8	Intra-trap loss mechanisms in a magneto-optical trap. . . . .	13
1.9	Shape of atom number loading versus time in a MOT. . . . .	15
2.1	Collision of two particles in the center of mass frame . . . . .	20
2.2	Classical collision picture. . . . .	28
2.3	Cartoon drawing of protons and electrons for two hydrogen atoms. . . . .	29
2.4	Velocity averaged collisional loss cross section versus trap depth. . . . .	32
3.1	Schematic of the optical setup for the the pump and repump light of the MOT used for loss cross section measurements. . . . .	35
3.2	Flourescence signal of a MOT loading. . . . .	38
3.3	Example of experimental data taken to determine the loss rate in a magnetic trap. . . . .	40
3.4	A decay curve for a magnetic trap. . . . .	41
3.5	A plot of velocity averaged collisional loss cross section as a function of argon density for a MOT and a magnetic trap. . . . .	42
3.6	Excitation of ground state atoms to a repulsive excited molecular potential with a ‘catalysis’ laser can cause loss of trapped atoms. . . . .	43
3.7	The experimental setup used to measure the trap depth of a MOT using a catalysis laser. . . . .	45
3.8	$J = \frac{N_{ss}^0}{N_{ss}} - 1$ vs the catalysis laser duty factor $d$ . . . . .	46

*List of Figures*

---

3.9	$J$ vs $d$ shown in the linear region (i.e. small values of the duty factor, $d$ ). . . . .	47
3.10	A measure of the loss rate constant due to catalysis plotted versus detuning of the catalysis laser. . . . .	48
3.11	Measurement of three different MOT trap depths. . . . .	50
3.12	Velocity averaged collisional loss cross section versus trap depth. . . . .	51
3.13	Velocity averaged collisional loss cross section versus trap depth for the data taken with a MOT. . . . .	52
4.1	A mercury manometer. . . . .	58
4.2	A capacitance diaphragm gauge. . . . .	59
4.3	An AC bridge . . . . .	60
4.4	A schematic of a spinning rotary gauge . . . . .	61
4.5	An ionization gauge. . . . .	63
4.6	Schematic of an orifice-flow pressure standard. . . . .	67
4.7	A constant pressure flow meter. . . . .	69
5.1	Vacuum apparatus for the pressure sensor experiment. . . . .	78
5.2	A different perspective of the vacuum apparatus for the pressure sensor experiment. . . . .	79
5.3	The 2D MOT chamber. . . . .	83
5.4	A cutaway of the differential pumping section. . . . .	84
5.5	The 2D MOT coils installed on the 2D MOT chamber. . . . .	85
5.6	A drawing of the frame used to wind the 2D MOT coils. . . . .	86
5.7	A picture of the titanium sublimation pump. . . . .	88
5.8	A picture of the bakeout oven. . . . .	92
5.9	The schematic of the optical setup used for the pressure sensor experiment. . . . .	98
5.10	A picture of the 2D MOT optics along one arm. . . . .	101
5.11	A picture of the 2D MOT cloud. . . . .	102
5.12	A picture of the 3D MOT. . . . .	103
6.1	Experimental setup of atomic beam divergence measurement. . . . .	105
6.2	A fluorescence image of the Rb beam. . . . .	106
6.3	Initial fluorescence signal in the 3D MOT from initial turn-on of 2D MOT. . . . .	107
6.4	The capturable speed distribution of the atomic beam coming from the 2D MOT. . . . .	110

*List of Figures*

---

7.1	An example loading curve taken with a 3D magneto-optical trap at a residual background pressure of $1.79 \times 10^{-5}$ Pa ( $1.34 \times 10^{-7}$ Torr). . . . .	113
7.2	The loss rate constant due to background collisions versus total background pressure. . . . .	114
7.3	An example decay curve of a 3D MOT in the presence of Ar background gas. . . . .	115
7.4	The MOT loss rate constant due to background collisions versus background pressure of Ar. . . . .	116
8.1	A magnetic coil for the 3D MOT and magnetic trap. . . . .	119
8.2	Drawing of apparatus with the NIST gauges. . . . .	120
A.1	Evidence that loading rate of a MOT is proportional to the square of trap depth. . . . .	135
A.2	Predicted MOT trap depth using the ratio of loading rates versus measured MOT trap depth. . . . .	137
A.3	Evidence that the loading rate of a vapour loaded Rb MOT is proportional to the background density of Rb. . . . .	138
A.4	Measurement of $M_i$ versus the density of background gas, $n_{\text{Rb}}$ . . . . .	140
A.5	A plot of $\frac{M_i}{n_{\text{Rb}}}$ versus $U_i^2$ . . . . .	141

# List of Abbreviations

**3D** three dimensional

**2D** two dimensional

**MOT** magneto-optical trap

**RF** radio-frequency

**UHV** ultra-high vacuum

**CDG** capacitance diaphragm gauge

**SRG** spinning rotary gauge

**RGA** residual gas analyzer

**TSP** titanium sublimation pump

**NEG** non-evaporable getter

**CF** ConFlat

**TA** tapered amplifier

**AOM** acousto-optical modulator

**NIST** National Institute of Standards and Technology

# Acknowledgements

Thank you to Dr. Kirk Madison for allowing me to be a part of the lab, for patience in teaching, and for much help given to me. I thank you greatly for being my supervisor. Thank you to Dr. James Booth for participation in every aspect of this thesis and the work described in it. Thank you very much for the time you spend helping me and others in the lab. Thank you to Dr. Bruce Klappauf for getting the lab off to a good start and helping me many times. Thank you to Dr. Arthur Mills for help many times. Thank you to Dr. Benjamin Deh for the important work he performed.

Thank you to my committee members Dr. Mona Berciu, Dr. Taka Mose and Dr. Valery Milner for their time, help, and useful commentary. Thank you to the external examiner Dr. Paul Haljan for extremely useful suggestions and revisions, and for the time spent in reading and correcting this thesis. Thank you to my university examiners, Dr Fei Zhou and Dr. Ed Grant, for the time spent reading my thesis, and useful commentary during the final oral exam. Thank you to the chair, Dr. Ezra Kwok, for his time spent. Thank you again to Dr. Mona Berciu and to Dr. Ovi Toader for help many times. Thank you to Dr. James Fedchak for the time spent collaborating with our lab and for sending us calibrated gauges from NIST.

Thank you to my physics professors and teachers: Mr. Bergen, Dr. Williams, Dr. Hayden, Dr. Ozier, Dr. Axen, Dr. McCutcheon, Dr. Halpern, Dr. Van Raamsdonk, Dr. Michal, Dr. Kiefl, Dr. Berciu, Dr. Zhou, Dr. Milner, Dr. Jones, Dr. Madison, Dr. Franz, Dr. Mattison, Dr. McKenna, Dr. Gay, Dr. Affleck, Dr. Hardy, Dr. Krems, Dr. Schleich, Dr. Rozali, Dr. Hickson, Dr. Rieger, Dr. Waltham, Dr. Kotlicki, and Dr. Carolan. Thank you to Dr. Blades. Thank you to Dr. Bates, Dr. Koster, Dr. Turrell, and Dr. Ives. A special thank you to Dr. Lam and Dr. Gerry for their support and encouragement.

Thank you to the physics electronics shop: Pavel, Stan, Richard, Gar, Marcel, Dave, Victor and Tom. Thank you to the physics machine shop: Martin, Dan, Nick, Matt, and Steve. Thank you to Domenic. Thank you to Doug, Joseph, and Tongkai. Thank you to the physics stores staff: Brian, Geoffrey, and Mark. Thank you to the physics department staff, especially

## *Acknowledgements*

---

Oliva, Bridget, Theresa, and Anilu. Thank you to the EngPhys project lab: Dr. Marziali, Dr. Nakane, and Bernhard. Thank you to the IT physics department: Ron, Mary Ann, Gerry, Hongyun, and Tom. Thank you to the chemistry electronics shop staff: Brian, Benny, and Tony. Thank you to the chemistry stores staff: John, Karen, Pat, Nate, Xin-Hui, and Sabrina. Thank you to the machinists at BCIT: Ernie and Glenn. Thank you to the custodial staff, Harry, UBC security, UBC plant-ops, UBC building operations, and building management for their help and encouragement.

Thank you to all members of the lab, as well as thesis or project students, past and present. In particular, thank you to Tao, Jordan, Amy, Swati, Sylvan, Keith, Paul, Ray, Davey, Pavle, Bastian, Nina, Peter, Aviv, David, Alan, Bo, Magnus, Dallas, Chenchong, Gabriel, Tino, Theo, Ian, Weiqi, Haotian, Kousha, Nathan, Nam, Kais, Troy, Greg, Will, Will, Jon-Paul, Damien, Joshua, Kyle, Alec, Alysson, Brendan, Daniel, Mariusz, Gene, Tom, Zhiying, Felipe, Victor, Adrian, Glenn, Kahan, Kai, Koko, Steve, Calvin, Paul, Julien, Fumiei, Forrest, Blake, and Jeffrey. A special thanks to Mariusz, Will, Will, Gene, Tom, and Kais, who are the current core graduate group and have helped greatly. Another special thanks to Ian, Weiqi, Haotian, Kousha, Victor, Adrian, Dr. James Booth, Dr. Kirk Madison, Kais, Jeffrey, Blake and Forrest who have greatly contributed to the pressure measurement experiment. Thank you to the members past and present of Dr. Momose's group, Dr. Jones's group, Dr. Milner's group, Dr. Krem's group, Dr. Shapiro's group, and Dr. Grant's group. Thank you to Dr. David Jones, T.J., Rob, Sybil, Matt, Yifei, Egor, Joshua, Emily, Carolyn, Marc, and Graeme. Thank you to Pavle for help many times. Thank you to those that attended my doctoral exams for their support. Thank you to the undergraduate and graduate students I have met, especially Lionel, Raveen, Anand, Dan, Sergei, Ryan, Jeff, Mandy, Eva, Adrian from chemistry, Lara, Jasmine, Cecile, and Karla. Thank you to the Graduate Studies staff. Thank you to Murray McEwan at Agilent. Thank you to Randy, Jomy, Jinshan, Maria, Ian, Claire, and Patricia. Thank you to my Dad. Thank you to Jesus and Our Father.

# Chapter 1

## Introduction

### 1.1 Thesis overview

Loss of ultracold trapped atoms due to collisions with background (non trapped) particles can be an unwanted feature that reduces the sample size of the trapped atoms to be studied. This thesis, however, shows that the loss rate of trapped atoms due to background gas collisions can be an important and useful experimental observable. The first part of this thesis (chapters 1-3) describes how the velocity averaged collisional loss cross section,  $\langle\sigma v_i\rangle_{X,i}$ , due to collisions between trapped atoms of type  $X$  and background gas of species  $i$ , is calculated and measured. This quantity is related to the loss rate due to background collisions and is shown to have significant trap depth dependence when comparing trap depths of several mK to several K. This trap depth dependence can be important to take into account for collision cross section measurements which use loss of trapped atoms due to collisions as their measurement observable. A wide variety of such experiments exist involving trapped ions [1–3], electron beams [4, 5], and atoms and molecules [6–10]. Photoionization cross sections have also been measured [11–13] using trapped atoms. As shown in Ref. [9] and Ref. [14], the measured collision cross section based on loss from a trap can be lower than the total cross section. This is because not all collisions impart sufficient kinetic energy to the trapped atoms to cause loss from the trap.

In our experiments  $^{87}\text{Rb}$  was used as the trapped species,  $X$ , and  $^{40}\text{Ar}$  as the background species  $i$ . The velocity averaged collisional loss cross section  $\langle\sigma v_{\text{Ar}}\rangle_{^{87}\text{Rb},^{40}\text{Ar}}$  was calculated for a range of trap depths and measured previously by members of our lab using a magnetic trap [14, 15]. The magnetic trap used could obtain trap depths up to 10 mK. The work performed for this thesis was an extension of the measurement of  $\langle\sigma v_{\text{Ar}}\rangle_{^{87}\text{Rb},^{40}\text{Ar}}$  to larger trap depths (0.5 to 2.2 K) using a magneto-optical trap (MOT). A technique was adapted from Hoffmann et al. [16] to measure the trap depth of a MOT. In this way a verification of the shape of the calculated  $\langle\sigma v_{\text{Ar}}\rangle_{^{87}\text{Rb},^{40}\text{Ar}}$  versus trap depth curve was performed for the trap depths attainable with our magnetic trap and magneto-optical trap. The results of this work are also

reported in [17].

Chapter 1 provides necessary background information on the atomic traps used in this work. Chapter 2 gives a basic understanding of the calculation of the velocity averaged collisional loss cross section. Chapter 3.1 explains and presents results for the measurement of the velocity averaged collisional loss cross section using a MOT. The measurement of the MOT trap depth is also described in this chapter.

The second, and related, topic covered in this thesis (chapters 4 - 8) is the progress made towards using the background collision induced loss rate to determine the density of the background gas. Using trapped atoms as a density (pressure) sensor would be a novel approach for a pressure standard in the range of  $10^{-5}$  to  $10^{-8}$  Pa ( $10^{-7}$  to  $10^{-10}$  Torr). The potential advantages of such a standard are reproducibility from lab to lab, the potential of miniaturization and portability, and the possibility of externally calibrated gauges not being needed, or needed only seldomly.

Chapter 4 gives background information on the commercial pressure gauges installed in our apparatus and existing pressure standards. Chapter 5 gives a description of our experimental apparatus for pressure measurement and details about the assembly of this apparatus to date are provided. Chapter 6 describes characterization performed of the two dimensional magneto-optical trap that is part of the apparatus. Chapter 7 describes loss rate measurements using a 3D magneto-optical trap as pressure in the system varied. Chapter 8 contains conclusions as well as the future outlook for the pressure experiment.

## 1.2 Atomic traps

The “trapping of atoms” means to spatially confine them with light, electric fields, or magnetic fields so that the atoms are held in vacuum and thereby isolated from the walls of the vacuum chamber. The average temperature,  $T$ , of the trapped atoms is defined by the average kinetic energy of the atoms as  $k_B T$ . Typical temperatures are in the  $\mu\text{K}$  to  $\text{mK}$  range. Every trap has an associated trap depth,  $U_{\text{trap}} = \frac{1}{2} m v_e^2$ , where  $v_e$  is the escape speed needed for an atom to leave the trap. Trap depth will depend on the parameters of the confining fields such as light intensity, light frequency, and magnetic field gradient. Depending on what type of trap is being used, trap depths can go up to several K. This section will discuss the principle of a 3D magneto-optical trap and a quadrupole magnetic trap. Atom number dynamics in these traps is discussed in the next section.

### 1.2.1 3D magneto-optical trap

A magneto-optical trap (MOT) provides a means of obtaining a sample of ultracold atoms starting from a vapour or with a beam of atoms [18, 19]. A magneto-optical trap both slows (cools) and traps (confines) atoms. In a 3D MOT (see Fig. 1.1) three orthogonal counter-propagating pairs of laser beams with frequency,  $\omega$ , slightly tuned below an atomic resonance, perform laser cooling [19]. Laser cooling requires the light to be below atomic resonance because of the Doppler shift. In the Doppler effect an atom travelling with velocity  $\vec{v}$  will ‘see’ light with wavevector  $\vec{k}$  and frequency  $\omega$  as having frequency  $\omega' = \omega - \vec{k} \cdot \vec{v}$ . When an atom with velocity  $\vec{v}$  absorbs a photon with wavevector  $\vec{k}$ , the momentum of the atom is changed by  $\hbar\vec{k}$ . The atoms entering the intersection of the orthogonal laser beam pairs will be slowed down by photons with  $\vec{k} \cdot \vec{v} < 0$ . Photons with  $\vec{k} \cdot \vec{v} > 0$  would speed up the atoms. In the second case these photons have their frequency shifted farther away from resonance so that they have a smaller probability of being absorbed. In this manner the atoms preferentially absorb photons that slow them down. Atoms spontaneously emit the photons in random directions so that, averaging over many absorption and emission events, the momentum gain from emission is zero and the atoms are slowed down.

Laser cooling does not slow the atoms down completely to zero velocity. Momentum kicks imparted to the atoms from absorption and emission of photons result in residual motion of the atoms. Laser cooling also does not form a trap. The slowing force depends on their velocity and not their position so the atoms will diffuse out of the intersection of the laser beams. To provide a position dependent force for trapping, a magnetic field is added produced by two concentric coils in an anti-Helmholtz configuration. The anti-Helmholtz configuration consists of coils that are parallel and spaced by their own radii, and have equal current through the coils running in opposite directions. The direction concentric with the coils’ centers is called the axial direction. For the direction of current shown in Fig. 1.2 the magnetic field along a line parallel to, and half way in between, the two coils starts at zero magnitude at the origin and increases linearly outwards pointing away from the center along the radial direction. Along the axial direction in Fig. 1.2 the magnetic field points toward the center of the MOT and the axial magnetic field gradient,  $\frac{d|\vec{B}|}{dz}$  is double the gradient along the radial directions [20].

In a MOT the magnetic field in combination with the appropriate polarization choice of the laser beams provides confinement of the atoms. In a MOT atoms preferentially absorb light that pushes them to the magnetic field zero. The trapping region is at the intersection of the laser beams cen-

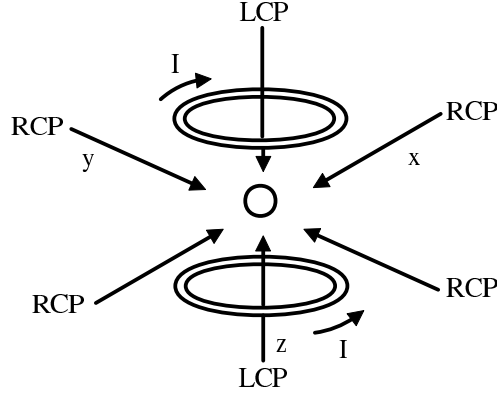


Figure 1.1: A magneto-optical trap (MOT). Three counterpropagating pairs of laser beams along three perpendicular axes are used along with two magnetic coils in anti-Helmholtz configuration. The laser polarization is right circularly polarized (RCP) for beams travelling along the radial direction where the magnetic field is pointing radially outwards. The laser polarization is left circularly polarized along the axial direction (concentric with the coils) where the B field is pointing towards the center of the MOT. The trapping region is formed at the intersection of the six beams centered on the zero of the magnetic field and a cloud of atoms will be collected there.

tered on the zero of the magnetic field. Figure 1.3 explains the principle of a MOT. The laser light with energy  $hf_L$  is detuned below the  $F = 0$  to  $F' = 1$  transition, taken as an example. In the presence of the weak magnetic field of magnitude  $B$  generated in a MOT, the hyperfine  $m_F$  sublevels change according to  $\Delta E = m_F g_F \mu_B B$ , where  $g_F$  is the Landé g-factor and  $\mu_B$  is the Bohr magneton [21, 22]. For  $g_{F'} > 0$  the  $m_{F'} = -1$  transition decreases in energy away from the magnetic field zero position.

Along the radial axes, right circularly polarized (RCP) light propagating in the same direction as the B-field will drive  $\Delta m_F = m_{F'} - m_F = +1$ , called  $\sigma^+$  transitions. Right circularly polarized (RCP) light propagating in the opposite direction to the B-field will drive  $\Delta m_F = m_{F'} - m_F = -1$ , called  $\sigma^-$  transitions. In Fig. 1.3 the  $m_F = 0$  to  $m_{F'} = -1$  transition is closest to the laser frequency so the atoms would preferentially absorb the  $\sigma^-$  light. If  $\sigma^-$  light is travelling toward the center on either side of the magnetic field zero then an atom which goes away from the center will be pushed back towards the center. Along the z axis, concentric with the coils, the B field is pointing inwards (as shown in Fig. 1.2). For this case left circularly polarized

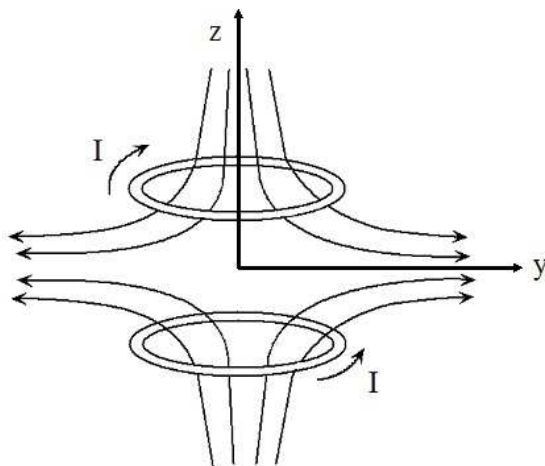


Figure 1.2: The magnetic field lines generated by passing current  $I$  in opposite directions through two coils spaced by their radii (known as anti-Helmholtz configuration). The magnetic field is zero at the center between the coils and increases linearly in magnitude pointing away from the center in the radial direction and towards the center in the axial direction. The  $z$ -axis is the axial direction. The  $x$ -axis (coming out of the page) and the  $y$ -axis are pointing radially.

light must be used along the  $z$  axis. Left circularly polarized light travelling in the same direction as the magnetic field will drive  $\Delta m_F = m_{F'} - m_F = -1$  transitions and  $\Delta m_F = m_{F'} - m_F = +1$  transitions when anti-aligned with the magnetic field.

For the work presented in the body of this thesis,  $^{87}\text{Rb}$  was primarily used as the trapped atom species. The system used also has the ability to trap  $^{85}\text{Rb}$ , which was used as the trapped atom of choice for the work presented in the appendix. The choice to use one species or the other is often a practical matter of availability of the lasers used for each species. For work involving magnetic trapping, as will be discussed in the next section, it is more convenient to use  $^{87}\text{Rb}$  in order to trap atoms that are all in the same hyperfine sublevel.

The laser light used for the trapping in the MOT is called the pump light. A secondary laser light, called the repump light, is also needed to prevent atoms from pooling in a hyperfine state that cannot be excited by the pump laser. The  $5^2S_{1/2}$  to  $5^2P_{3/2}$  transition is used for the pump and

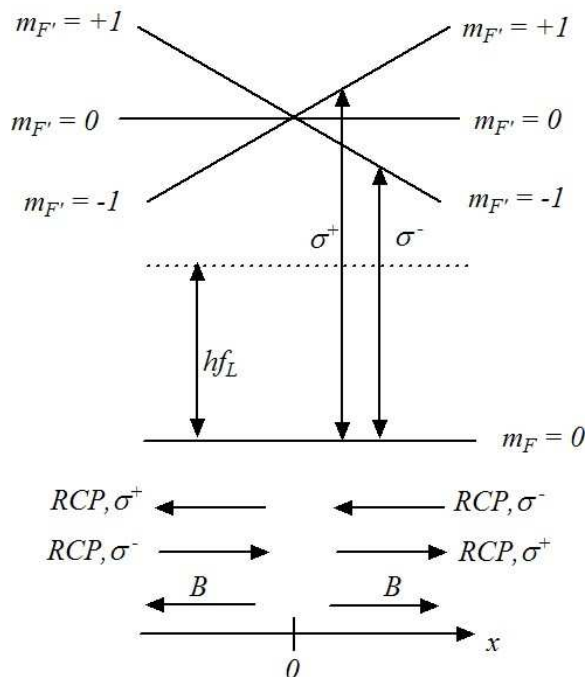


Figure 1.3: Hyperfine sublevels undergoing a continuous energy shift with changing magnetic field in a magneto-optical trap. The vertical axis, not labelled, is energy. Atoms that move to the right or left of the magnetic field zero have a greater probability of absorbing light on a  $\sigma^-$  transition that pushes the atoms back towards the magnetic field zero.

repump processes (see Figs. 1.4 and 1.5). The pump is chosen to be resonant with the  $F = 2$  to  $F' = 3$  transition for  $^{87}\text{Rb}$  and  $F = 3$  to  $F' = 4$  transition for  $^{85}\text{Rb}$ . The repump is chosen to be resonant with the  $F = 1$  to  $F' = 2$  transition for  $^{87}\text{Rb}$  and  $F = 2$  to  $F' = 3$  transition for  $^{85}\text{Rb}$ . Taking  $^{87}\text{Rb}$  as an example,  $F = 2$  to  $F' = 3$  light can also drive off-resonant transitions to the  $F' = 2$  or  $F' = 1$  hyperfine level. These levels can decay to the  $F = 1$  hyperfine state of the  $5^2S_{1/2}$  ground state. The atoms will not strongly absorb the pump light once in that state and laser cooling and trapping will not be accomplished. In order to get the atoms out of this ‘dark’ state, repump light driving the  $F = 1$  to  $F' = 2$  transition is needed so that there is some probability of atoms decaying back to the  $F = 2$  ground state.

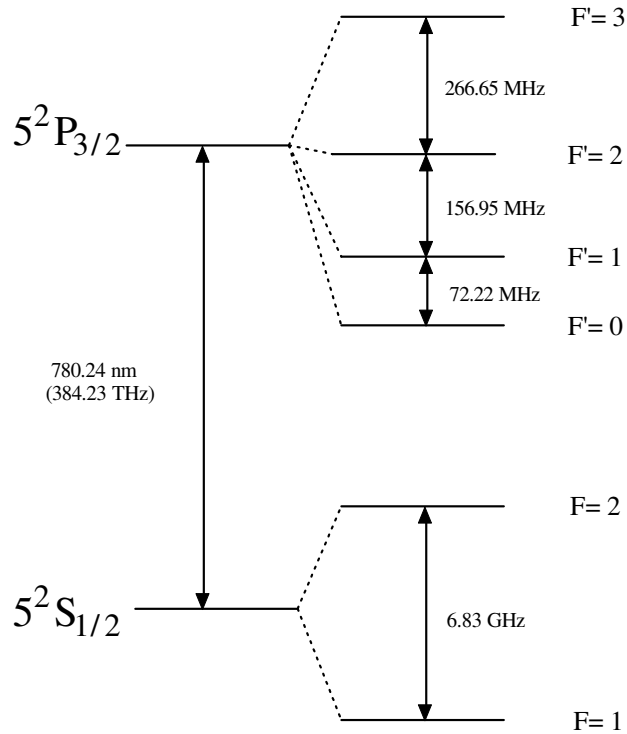


Figure 1.4: The energy levels for the  $D_2$  transition for  $^{87}\text{Rb}$ . The  $F = 2$  to  $F' = 3$  transition is used for the pump light of the magneto-optical trap. The  $F = 1$  to  $F' = 2$  transition is used for the repump light. Numerical values and concept of figure from [21].

## 1.2.2 Magnetic traps

### Principle of a magnetic trap

After cooling and collecting atoms in a MOT they can be transferred to a magnetic trap for further study or cooling. The initial cooling stage in a MOT is necessary because magnetic traps provide much weaker confinement forces than a MOT and do not provide cooling. A quadrupole magnetic trap can be formed using the same coils as used for the MOT. The laser light is shut off and a higher current than used for the MOT is run through the coils to produce a higher magnetic field gradient. The magnetic field zero is where the middle of the trap is. The magnetic field increases in magnitude away from where the magnetic field zero is located.

The contribution to the hamiltonian due to the electron spin,  $\vec{S}$ , elec-

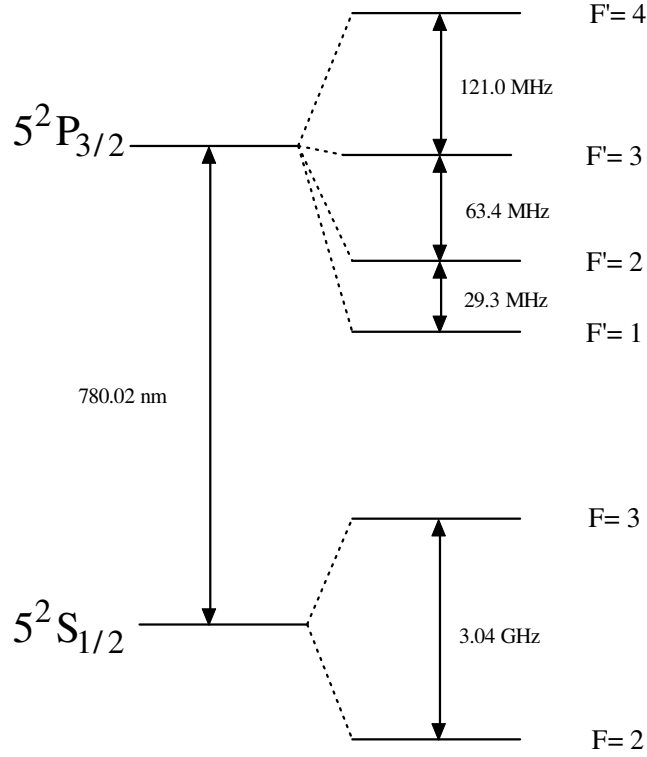


Figure 1.5: The energy levels for the  $D_2$  transition for  $^{85}\text{Rb}$ . The  $F = 3$  to  $F' = 4$  transition is used for the pump light of the magneto-optical trap. The  $F = 2$  to  $F' = 3$  transition is used for the repump light. Numerical values and concept of figure from [23].

tron orbital angular momentum,  $\vec{L}$ , and nuclear spin,  $\vec{I}$ , interacting with an external magnetic field,  $\vec{B}$ , is expressed as

$$H_B = \frac{\mu_B}{\hbar}(g_S\vec{S} + g_L\vec{L} + g_I\vec{I}) \cdot \vec{B}. \quad (1.1)$$

Here  $\mu_B = 9.274 \times 10^{-24}$  J/T is the Bohr magneton, and  $g_S$ ,  $g_L$ , and  $g_I$  are the spin, orbital and nuclear g-factors, respectively.

For weak magnetic fields,  $H_B$  is a perturbation to the hyperfine energy levels, and the hyperfine levels change according to  $\Delta E = g_F m_F \mu_B B$ . Atoms in states that have Zeeman shifts resulting in higher energy as magnetic field increases (states with  $g_F m_F > 0$ ) will tend to stay near the zero

of the field and are called ‘low field seekers’. Atoms that are ‘high field seekers’ will leave the trap.

Referring to the energy level diagram in Fig. 1.4, for example,  $g_F = -1/2$  for the  $F = 1$  hyperfine level of the  $5^2S_{1/2}$  ground state for  $^{87}\text{Rb}$  and  $g_F = +1/2$  for the  $F = 2$  hyperfine level. This means the trappable state for the  $F = 1$  level is  $m_F = -1$  and for the  $F = 2$  state the sublevels  $m_F = 1, 2$  can be trapped. The atoms can be prepared in the lower  $F = 1$  or upper  $F = 2$  state by the order of turn-off of the pump and repump when loading the magnetic trap. If the repump is turned off a few ms before the pump then the atoms will be in the lower hyperfine level. Conversely, if the pump is turned off first the atoms will be in the upper hyperfine level of the  $5^2S_{1/2}$  ground state.

$^{87}\text{Rb}$  is preferable for magnetic trapping since its lower hyperfine ground state ( $F = 1$ ) only has one trappable state ( $m_F = -1$ ). For  $^{85}\text{Rb}$ , the  $F = 2$  lower level of the  $5^2S_{1/2}$  ground state has  $g_F = -1/3$  and so both the  $m_F = -2$  and  $m_F = -1$  state are trappable. Trap depth depends on the  $m_F$  state and applications where trap depth is important requires a single  $m_F$  state to be trapped. Gravitational filtering can be used to isolate the  $F = 2, m_F = -2$  state for  $^{85}\text{Rb}$ . This is performed by lowering the magnetic field gradient (and hence trap depth) so that the  $m_F = -1$  state is not supported against gravity while the  $m_F = -2$  state is.

The expression  $\Delta E = g_F m_F \mu_B B$  for the energy change of the hyperfine levels with magnetic field is only valid for weak magnetic fields ( $\lesssim 0.001$  T or  $\lesssim 10$  G [22]). For larger magnetic fields where the  $H_B$  term of the hamiltonian is comparable to the hyperfine term, the two contributions together are a perturbation on the fine structure states. The energy shifts on the fine structure in this case are given by diagonalizing the hyperfine and magnetic field contribution. For  $J = 1/2$  the energy shift is conveniently given by the Breit-Rabi formula [22]. For strong fields the  $H_B$  term is treated as a perturbation on the fine structure which cause the energy of the fine structure states to change according to  $\Delta E = g_J m_J \mu_B B$ . The hyperfine term is a further perturbation on those fine structure states which causes further splitting and energy level change for different  $m_I$  values. Figure 1.6 shows the change in the hyperfine levels of  $^{87}\text{Rb}$  in the  $5^2S_{1/2}$  ground state [21]. For weak magnetic fields the energy shift is linear with magnetic field magnitude. For intermediate fields the energy levels can change non-linearly with magnetic field and states that were low field seeking at weak fields (for example the  $|F = 1, m_F = -1\rangle$  state) can become high field seeking. Similarly a state that was high field seeking at weak fields can become low field seeking at higher fields (for example the  $|F = 2, m_F = -1\rangle$  state). For

sufficiently large fields this must be taken into account when determining the trap depth and which states are trappable.

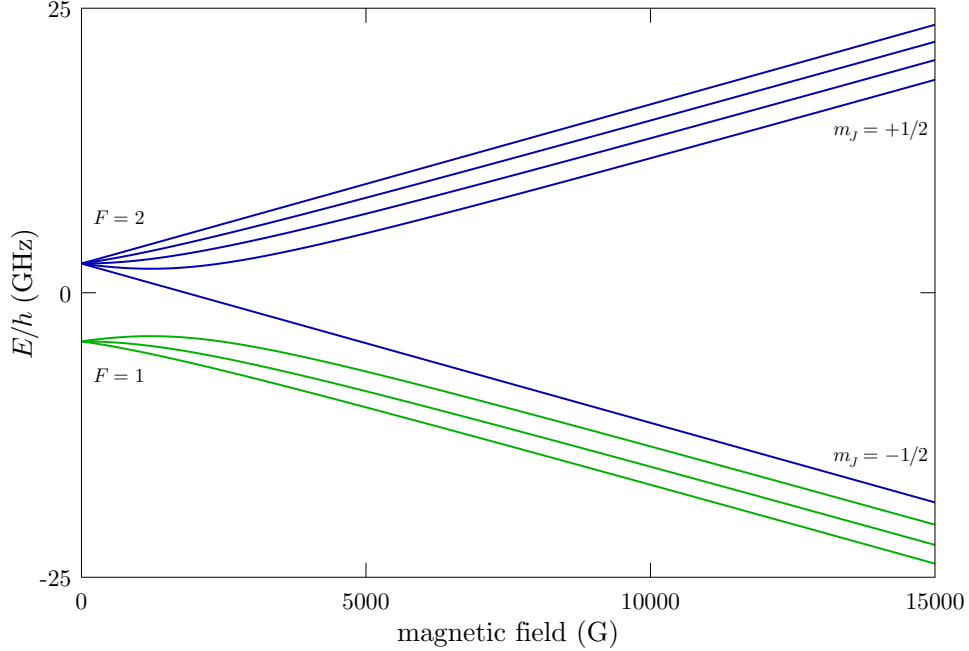


Figure 1.6: Energy level changes for the  $5^2S_{1/2}$  ground state of  $^{87}\text{Rb}$  as a function of increasing magnetic field. Reproduced with permission from Dr. Steck [21].

For this work we typically work at up to a maximum of 400 G in the weak and intermediate magnetic field regimes. Taking the weak field case, the trap depth of the magnetic trap, along a given direction, for an atom in state  $m_F$  will be  $\Delta E = g_F m_F \mu_B (B_{\max} - B_{\min})$  where  $B_{\max}(B_{\min})$  is the maximum (minimum) magnetic field a trapped atom can access along that direction. For quadrupole magnetic fields created by the coils in anti-Helmholtz configuration,  $B_{\min} = 0$  and  $B_{\max}$  is limited either by the size of the vacuum cell or the roll-off of the magnetic field. In our case the size of the cell walls limits the maximum magnetic field the trapped atoms can experience. The cell walls are at room temperature and so when a trapped atom hits the cell wall it gains a large amount of kinetic energy and will not be trapped anymore.

The magnetic field gradient is different in different directions away from

the magnetic field zero which means the trap depth is not the same in all directions. For the work described in chapter 3, the trap depth,  $U$ , assigned to the magnetic trap used was taken as an average of the maximum energies of a trapped atom along the downward axial direction and the radial direction.

$$k_B U = \frac{[E(B(z_w)) - mgz_w] + E(B(y_w))}{2} \quad (1.2)$$

Here  $z_w$  and  $y_w$  are the distances from the magnetic field zero to the cell wall along the axial and radial directions, respectively. For the work in chapter 3 these were both 0.5 cm.  $B(z_w)$  and  $B(y_w)$  are the magnetic field magnitudes at the cell wall along the axial and radial directions, respectively.  $E(B(z_w))$  and  $E(B(y_w))$  are the energies of the atoms at the cell wall along the axial and radial directions, respectively. The  $mgz_w$  term accounts for the decrease in trap depth along the downward axial direction where  $m$  is the mass of a trapped atom and  $g$  is the gravitational acceleration. For a distance of  $z_w = 0.5$  cm this gives  $mgz_w/k_B = 0.5$  mK, which lowers the trap depth along the downward axial direction for  $^{87}\text{Rb}$ . Magnetic traps have typical trap depths on the order of a few mK.

The magnetic field from a pair of coils in anti-Helmholtz configuration can be approximated as

$$B_z \approx 3\mu_0 \frac{DR^2}{(D^2 + R^2)^{5/2}} Iz \quad (1.3)$$

and

$$B_y \approx \frac{3}{2}\mu_0 \frac{DR^2}{(D^2 + R^2)^{5/2}} Iy. \quad (1.4)$$

Here  $\mu_0$  is the permeability of free space,  $2D$  is the spacing between the top and bottom coils,  $R$  is the coil radius, and  $I$  is the current. The coordinates  $y$  and  $z$  are the distances from the origin along the  $y$  and  $z$  directions, respectively, as shown in Fig 1.2. The predicted gradient along the axial direction,  $\frac{dB}{dz}$ , is double that along the radial direction,  $\frac{dB}{dy}$ . This means the trap depth along the axial direction is approximately double that of the radial direction.

For the expressions for magnetic field given in Eq. 1.3 and Eq. 1.4 the magnetic field increases linearly in magnitude away from the magnetic field zero. A more accurate non-linear expression for the magnetic field for a circular loop is given in Ref. [24]. A discussion of the error this introduces is given in section 3.4.1.

## RF knife

A useful way of controlling the trap depth of a magnetic trap is with a ‘Radio Frequency (RF) knife’ [25]. The concept is explained in Fig. 1.7. An RF frequency is introduced while the magnetic trap is on. When the

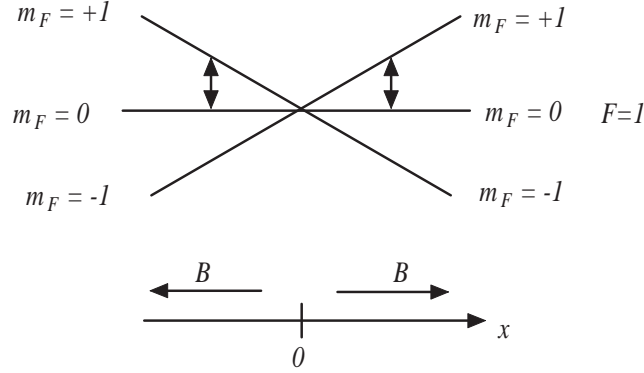


Figure 1.7: Hyperfine sublevels undergoing a continuous energy shift with changing magnetic field in a magnetic trap. The vertical axis, not labelled, is energy. The trappable state shown here is the  $m_F = 1$  state (assuming  $g_F > 0$  here). An RF frequency can cause transitions to the untrappable  $m_F = 0$  state and atoms will be lost from the trap.

splitting between levels of a trappable state (e.g.  $m_F = 1$  in Fig. 1.7) and an untrappable state (e.g.  $m_F = 0$  in Fig. 1.7) corresponds to the RF frequency, atoms that are in the trappable state can transition to an untrappable state. This limits the maximum energy an atom can have in the trap and therefore the trap depth.

## 1.3 Trap dynamics

### 1.3.1 Magneto-optical trap dynamics

In a magneto-optical trap the number of atoms in the trap as a function of time,  $N(t)$ , can be given as [26]

$$\frac{dN}{dt} = R - \Gamma N - \beta \int n^2(\vec{r}, t) d^3\vec{r} \quad (1.5)$$

with  $t = 0$  being when both the magnetic field and light have been turned on [27].  $R$  is the rate of capture, which is the number of atoms per second

entering the intersection of the six beams and being slowed down and confined.  $\Gamma N$  is the rate of loss due to collisions of background gas atoms with the trapped atoms.  $\Gamma$  has units of  $\text{s}^{-1}$  and is called the loss rate constant due to background collisions.  $\tau = 1/\Gamma$  is called the lifetime of the trap.  $\Gamma$  has typical values of 0.1 to 2  $\text{s}^{-1}$  for the experimental setup described in chapter 3 and the loading rate,  $R$ , is around  $10^6 \text{ s}^{-1}$  to  $10^7 \text{ s}^{-1}$ .

The last term of Eq. 1.5 describes losses due to the collision of two trapped atoms, where  $n(\vec{r}, t)$  is the density of the trapped atoms at position  $\vec{r}$  and time  $t$ . The origin is placed at the center of the trap where the atoms collect in a roughly spherical ball.  $\beta$  is the loss rate constant due to two-body ‘intra-trap’ collisions. It is on the order of  $10^{-11}$  to  $10^{-13} \text{ cm}^3 \text{ s}^{-1}$  and is mediated by radiative escape, fine-structure changing collisions and hyperfine changing collisions [27, 28]. Fig. 1.8 shows the mechanisms of

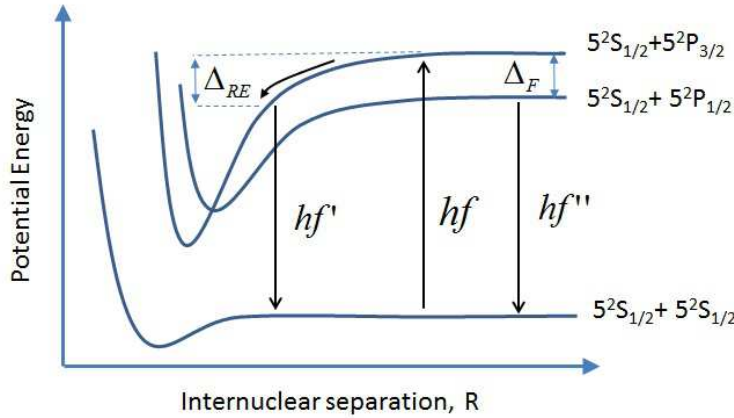


Figure 1.8: Radiative escape occurs when two ground state atoms are excited by a photon of energy  $hf$  and gain kinetic energy  $\Delta_{RE}$  before emitting a photon of energy  $hf' < hf$  to return to the ground state. Fine structure changing collisions occur when atoms in the  $5^2S_{1/2} + 5^2P_{3/2}$  excited state transfer over to the  $5^2S_{1/2} + 5^2P_{1/2}$  state. They then emit a photon of energy  $hf''$  to return to the ground state and gain kinetic energy  $\Delta_F$ . Figure patterned after Fig. 14 in [27].

radiative escape and fine-structure changing collisions. In the presence of light, ground state atoms (for example, both atoms in the  $5^2S_{1/2}$  state) can be excited by a photon of energy  $hf$  at a certain internuclear separation to an excited molecular potential (for example, the  $5^2S_{1/2} + 5^2P_{3/2}$  state).

The atoms can accelerate to an internuclear separation where the potential energy is lowered and emit a photon of lower energy  $hf'$  back to the ground state ( $5^2S_{1/2} + 5^2S_{1/2}$ ). The kinetic energy picked up by the atoms is  $\Delta_{RE} = hf - hf'$  and if the kinetic energy imparted to each atom is greater than the depth of the trap, loss will result. This mechanism of loss is called radiative escape [27, 28]. Fine-structure changing collisions occur when the atoms excited to the  $5^2S_{1/2} + 5^2P_{3/2}$  state switch over to the  $5^2S_{1/2} + 5^2P_{1/2}$  state at the cross-over between the two states. The atoms return to large internuclear separations along the  $5^2S_{1/2} + 5^2P_{1/2}$  state and emit a photon ( $hf''$ ) back to the ground state. In this process  $\Delta_F$  of energy is gained, which is the fine structure energy splitting between the  $5^2P_{1/2}$  state and the  $5^2P_{3/2}$  state. For homonuclear collisions each atom gains  $\Delta_F/2$  in kinetic energy. For  $^{87}\text{Rb}$  the energy gained by each atom in a fine-structure changing collision, in terms of temperature, is  $\frac{\Delta_F}{2k_B} = 171\text{K}$ . This kinetic energy gain far exceeds typical MOT trap depths of several K.

A loss mechanism that can also occur is hyperfine changing collisions where atoms colliding can change their hyperfine state, i.e. their  $F$  level. For example (referring to Fig. 1.4) two  $^{87}\text{Rb}$  atoms colliding in the  $F = 2$  state of the  $5^2S_{1/2}$  ground state can during a collision change to the  $F = 1$  level. The  $F = 1$  level is lower in energy than the  $F = 2$  level and the energy difference goes to the kinetic energy of the atoms. One or both of the colliding atoms can change their  $F$  level [27] while the sum of the  $m_F$  values remains the same.

If  $\beta \int n^2(\vec{r}, t) d^3\vec{r}$  is negligible compared to the background loss rate term then the solution to Eq. 1.5 is

$$N(t) = \frac{R}{\Gamma} (1 - e^{-\Gamma t}). \quad (1.6)$$

The steady state solution in this case is  $N(t = \infty) = \frac{R}{\Gamma}$ . Typically for a MOT operated in this regime the steady state number in a MOT is around  $10^7$  to  $10^{10}$  atoms. An example plot of  $N(t)$ , given by Eq. 1.6, is shown in Fig. 1.9.

Another case to consider is when  $\beta \int n^2(\vec{r}, t) d^3\vec{r}$  is not negligible, but the atom number density is less than approximately  $10^{10}$  atoms per  $\text{cm}^3$  [29]. In this case the atom cloud in the MOT has a gaussian density profile of  $n(\vec{r}, t) = n_0(t)e^{-\left(\frac{|\vec{r}|}{w}\right)^2}$ , where  $n_0(t)$  is the peak density at  $|\vec{r}| = 0$ , and  $w$  is the width of the gaussian distribution which is taken to be time-independent. For this density profile the integral in Eq. 1.5 is  $\int n^2(\vec{r}, t) d^3\vec{r} = [n_0(t)]^2 (w\sqrt{\frac{\pi}{2}})^3$ . The total number in the trap taken by integrating the den-

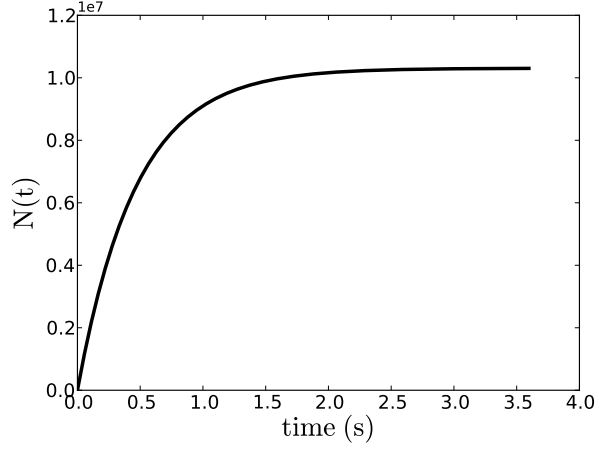


Figure 1.9: A plot of atom number,  $N(t)$ , versus time,  $t$ , from initial MOT loading. The plot uses the model given in Eq. 1.6 with  $R = 2.2 \times 10^7$  atoms/s and  $\Gamma = 2.1 \text{ s}^{-1}$ . The steady-state atom number is  $N(\infty) = \frac{R}{\Gamma} = 1.05 \times 10^7$ .

sity is  $N(t) = n_0(t) (w\sqrt{\pi})^3$ . Using these results Eq. 1.5 simplifies to

$$\frac{dN}{dt} = R - \Gamma N - aN^2 \quad (1.7)$$

where  $a = \frac{\beta}{(w\sqrt{2\pi})^3}$ . The solution to Eq. 1.7 is

$$N(t) = N_{\text{ss}} \left( \frac{1 - e^{-\gamma t}}{1 + \xi e^{-\gamma t}} \right) \quad (1.8)$$

where  $\gamma = \Gamma + 2\beta n_{\text{ss}}$  and  $\xi = \frac{\beta n_{\text{ss}}}{\Gamma + \beta n_{\text{ss}}}$  [17]. The steady state number  $N_{\text{ss}}$  is

$$N_{\text{ss}} = \frac{R}{\Gamma + \beta n_{\text{ss}}} \quad (1.9)$$

where the average steady state density of the MOT,  $n_{\text{ss}}$ , is

$$n_{\text{ss}} = \left( \frac{\int n^2 d^3r}{\int n d^3r} \right)_{\text{ss}}. \quad (1.10)$$

When the density of trapped atoms in a MOT is large the probability increases for the trapped atoms to absorb photons emitted by other trapped

atoms (called multiple scattering [29]). This results in an outward force on the trapped atoms which sets a limit on the maximum density of the trapped atoms at around  $10^{10} - 10^{11} \text{ cm}^{-3}$  [30]. One approximation used in this regime is that the trapped atom density is a constant,  $n$ , and Eq. 1.5 becomes

$$\frac{dN}{dt} = R - \Gamma N - \beta n N. \quad (1.11)$$

The solution to this equation can be solved as

$$N(t) = \frac{R}{\Gamma_{\text{eff}}} (1 - e^{-\Gamma_{\text{eff}} t}) \quad (1.12)$$

where

$$\Gamma_{\text{eff}} = \Gamma + \beta n. \quad (1.13)$$

To determine the background pressure range at which the intra-trap term can be neglected we use approximate values of  $\beta = 10^{-11} \text{ cm}^3 \text{ s}^{-1}$ , a total atom number  $N = 10^8$ , and a trapped atom density of  $n = 10^{10} \text{ cm}^{-3}$ . This gives  $\beta n N \approx 10^7 \text{ s}^{-1}$ . In order for  $\Gamma N$  to be an order of magnitude greater this means  $\Gamma > 1$  which corresponds to pressures in the mid  $10^{-6} \text{ Pa}$  ( $10^{-8} \text{ Torr}$ ) range and above.

### 1.3.2 Magnetic trap dynamics

Magnetic traps are loaded once with an initial number of atoms that then decays due to losses such as background collision induced loss. The number of atoms,  $N$ , in a magnetic trap after a time,  $t$ , from initial loading follows

$$\frac{dN}{dt} = -\Gamma N - \beta \int n^2(\vec{r}, t) d^3\vec{r} - MN. \quad (1.14)$$

As in Eq. 1.5 for a MOT,  $\Gamma$  is the loss rate constant due to background collisions. The  $\beta$  term is the loss rate constant due to intra trap collisions where  $n$  is the density of the trapped atoms. Here this intra-trap term includes only hyperfine changing collisions. Fine structure changing collisions and radiative escape are not loss mechanisms in a magnetic trap because those mechanisms involve the presence of light.  $M$  is the loss rate constant due to Majorana spin flip losses. This loss mechanism can occur when a trapped atom travels past the zero in the magnetic field, present in a quadrupole trap, where the magnetic field changes directions. In this case the  $m_F$  value can change to the opposite sign and the atom will no longer be trappable [28].

The hyperfine collision loss rate for  $^{87}\text{Rb}$  for the  $F = 2$ ,  $m_F = 2$  ground state is estimated to be on the order of  $10^{-15}\text{cm}^3/\text{s}$  [31]. To compare the size of the intra-trap loss term to the background loss term, we estimate the initial number in the magnetic trap to be on the order of  $10^8$  atoms.  $\Gamma$  is approximately  $0.01\text{ s}^{-1}$  for background gas pressures in the mid  $10^{-8}\text{ Pa}$  ( $10^{-10}\text{ Torr}$ ) range. This gives  $\Gamma N \approx 10^6\text{ s}^{-1}$ . Assuming a  $1\text{ cm}^3$  magnetic trap size, an order of magnitude estimate for the intra-trap loss rate is  $\beta n N \approx 10^{-15}\frac{\text{cm}^3}{\text{s}} \times 10^8\text{cm}^{-3} \times 10^8 \approx 10\text{ s}^{-1}$ . The intra-trap loss rate is well below the background loss rate expected in the  $10^{-8}\text{ Pa}$  ( $10^{-10}\text{ Torr}$ ) range.

The decay time due to Majorana spin flips is estimated as  $\tau = \frac{ml^2}{3\hbar}$  where  $m$  is the mass of a trapped atom, and  $l$  is the radius of the trapped atoms [28]. Taking  $^{87}\text{Rb}$  as the trapped atom and the trap size to be  $l = 1\text{ cm}$ , this gives a decay time of around 12 hours, which is far greater than the typical decay time  $1/\Gamma \approx 100\text{ s}$  at the mid  $10^{-8}\text{ Pa}$  ( $10^{-10}\text{ Torr}$ ) range.

If we assume then that the intra-trap and Majorana loss terms are negligible, the solution to Eq. 1.14 becomes

$$N(t) = N(0)e^{-\Gamma t} \tag{1.15}$$

where  $N(0)$  is the initial number in the magnetic trap.

This thesis will focus on the loss rate constant due to background collisions,  $\Gamma$ . Its dependence on trap depth and density of background gas are the two main topics presented. A pressure standard based on measurements of  $\Gamma$  is proposed and the current experimental progress to that end is described. To start, the next chapter explains the loss rate constant  $\Gamma$  in terms of its dependence on density of background gas and its dependence on the collisional loss cross section.

## Chapter 2

# Background gas collision induced loss

The situation of interest is that of an elastic collision involving a background gas atom and a trapped atom. The background gas particle could be residual background gas from the outgassing of vacuum parts, atoms that are of the trapped species that are not trapped, or a purposefully introduced background species such as Ar, N<sub>2</sub> or He.

The loss rate constant due to background gas collisions,  $\Gamma$ , introduced in the last chapter, can be written as

$$\Gamma = \sum_i n_i \langle \sigma_{\text{loss}} v_i \rangle_{X,i} \quad (2.1)$$

where  $n_i$  denotes the density of a particular background species  $i$ . The symbol  $\sigma_{\text{loss}}$  is the collisional loss cross section between a trapped atom of type  $X$  and a background species particle of type  $i$  [32, 33]. As we will see later in this chapter  $\sigma_{\text{loss}}$  is dependent on the relative kinetic energy of the colliding particles. The background gas speed,  $v_i$ , should actually be the relative gas speed,  $v_r$ . For our case our trapped atoms are assumed to be stationary, in the lab frame, with respect to the background gas atoms. In this case, the relative speed,  $v_r$ , of a trapped atom and a background gas particle is the speed of the background gas particle before collision,  $v_i$ . The brackets indicate a Maxwell-Boltzmann average over all possible speeds,  $v_i = 0$  to  $v_i = \infty$ , of background species  $i$ . Because we are describing loss from a trap,  $\sigma_{\text{loss}}$  also depends on the depth of the trap. If the trap depth is anisotropic then an average trap depth is taken. The calculation of the velocity averaged collisional loss cross section,  $\langle \sigma_{\text{loss}} v_i \rangle_{X,i}$ , is described in detail in [14, 15]. This chapter serves as an overview of those works.

### 2.1 A brief review of necessary scattering theory

To properly describe the meaning and calculation of  $\langle \sigma_{\text{loss}} v_i \rangle_{X,i}$ , a basic review of quantum scattering theory is needed. The following is based pri-

marily on the honours thesis of David Fagnan [15] who performed the calculation of  $\langle \sigma_{\text{loss}} v_i \rangle_{X,i}$  for our group. The calculation was for  $^{87}\text{Rb}$  in its ground state as the trapped species and  $^{40}\text{Ar}$  in its ground state as the background species. The following quantum textbooks and scattering theory notes are also helpful: Refs. [34–38].

The hamiltonian describing two interacting particles of mass  $m_1$  and  $m_2$  is

$$H = \frac{|\vec{p}_1|^2}{2m_1} + \frac{|\vec{p}_2|^2}{2m_2} + V(|\vec{r}_1 - \vec{r}_2|) \quad (2.2)$$

where  $\vec{r}_1, \vec{p}_1 = m_1\vec{v}_1, \vec{r}_2, \vec{p}_2 = m_2\vec{v}_2$  are the positions and momenta of particle 1 and 2 respectively.

The coordinate of the center of mass is

$$\vec{R} = \frac{m_1\vec{r}_1}{M} + \frac{m_2\vec{r}_2}{M} \quad (2.3)$$

and the velocity of the center of mass is

$$\vec{v}_R = \frac{m_1\vec{v}_1}{M} + \frac{m_2\vec{v}_2}{M} \quad (2.4)$$

where  $M = m_1 + m_2$  so that  $M\vec{v}_R = \vec{p}_1 + \vec{p}_2 = \vec{P}$  where  $\vec{P}$  is the total momentum. By conservation of total momentum  $\vec{v}_R$  is a constant. In the center of mass frame  $\vec{v}_R = 0$  so that the total momentum is zero and the particles have equal and opposite momenta. It is also useful to use the relative coordinate  $\vec{r} = \vec{r}_1 - \vec{r}_2$  and the relative velocity  $\vec{v}_r = \vec{v}_1 - \vec{v}_2$ . The relative velocity vector is the same in the lab and in the center of mass frame. Under conservation of momentum and total kinetic energy the magnitude of the relative velocity,  $|\vec{v}_r| = |\vec{v}_1 - \vec{v}_2|$ , is a constant before and after collision. This is most easily seen in the center of mass frame where the speeds of particles 1 and 2 are unchanged by an elastic collision. The direction of  $\vec{v}_r$  does change before and after collision. Using the center of mass coordinate and the relative coordinate the hamiltonian given in Eq. 2.2 can be connected to quantum mechanical operator form:

$$H = -\frac{\hbar^2}{2M}\nabla_R^2 - \frac{\hbar^2}{2\mu}\nabla_r^2 + V(r) \quad (2.5)$$

where  $\mu = \frac{m_1m_2}{m_1+m_2}$  is the reduced mass and  $\nabla_R^2$  and  $\nabla_r^2$  are the laplacians with respect to the center of mass and relative coordinates, respectively. In this form the hamiltonian is composed of a sum of a center of mass part and a relative part.

A time independent approach will be used because a time dependent wavepacket treatment given in [36] gives the same result for the differential collision cross section that is derived later in this chapter. A solution to the time independent Schrödinger equation,  $H\psi = E\psi$ , is  $\psi = \psi_R\psi_r$  where  $\psi_R$  satisfies the equation

$$-\frac{\hbar^2}{2M}\nabla_R^2\psi_R = E_R\psi_R \quad (2.6)$$

and  $\psi_r$  satisfies

$$\left[-\frac{\hbar^2}{2\mu}\nabla_r^2 + V(r)\right]\psi_r = E_r\psi_r \quad (2.7)$$

where  $E = E_R + E_r$ . The equation involving the center of mass coordinate is just that of a free particle of mass  $M$  where  $E_R = \frac{P_R^2}{2M}$  and  $P_R$  is the magnitude of the momentum of the center of mass. In the center of mass frame with  $P_R = 0$  we have  $E_R = 0$  and  $E = E_r$ . It also suffices to have  $P_R$  to be a constant so that  $E_R$  is a constant. The second equation has the form of a single particle of reduced mass  $\mu$  that is subject to a spherically symmetric potential  $V(r)$ . A collision of two particles is shown in the center

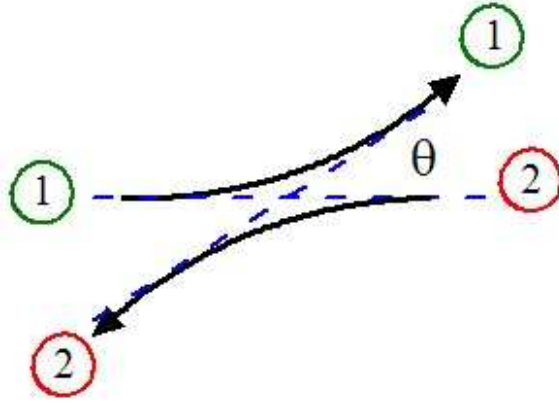


Figure 2.1: In the center of mass frame particles 1 and 2 travel with equal and opposite momenta. After collision they travel along a line that makes an angle  $\theta$  with respect to the original line of incidence.

of mass frame in Fig. 2.1 where the two particles approach each other with equal and opposite momenta, interact and then recede from each other with equal and opposite momenta. The path of the receding particles makes an angle  $\theta$  in the center of mass frame with respect to the original line of

incidence. Note the angle  $\theta$  is the angle between the relative velocity vectors before and after collision and is the same in both the lab and center of mass frames.

The assumption is now made that the change in speed (in the lab frame) of the trapped atom due to collision is much greater than the initial speed of the trapped atom before collision. With this assumption the kinetic energy imparted to the trapped atom with mass  $m_1$  in the lab frame is [15]

$$\Delta E \approx \frac{\mu^2}{m_1} |\vec{v}_r|^2 (1 - \cos(\theta)). \quad (2.8)$$

If  $\Delta E$  is greater than the trap depth,  $U_0$ , then the trapped atom involved in the collision will be lost from the trap. According to Eq. 2.8 this corresponds to collisional angles,  $\theta$ , greater than

$$\theta_{\min} = \cos^{-1} \left( 1 - \frac{U_0 m_1}{\mu^2 |\vec{v}_r|^2} \right) \quad (2.9)$$

As discussed above, in the center of mass frame the collision between the two particles can be equivalently thought of as a single particle of reduced mass  $\mu$  approaching a radially symmetric potential which goes to zero as  $r \rightarrow \infty$ . The solution  $\psi_r$  is expected to have the form

$$\psi_r \sim e^{i\vec{k}\cdot\vec{r}} + f(k, \theta, \phi) \frac{e^{ikr}}{r} \quad (2.10)$$

to describe the particle when it is far from the potential region after collision [38]. The first term describes that the particle is initially free, having plane wave behaviour. The second term describes scattering as a spherical wave where the probability of scattering into angles  $\theta$  and  $\phi$  is dependent on the scattering amplitude,  $f(k, \theta, \phi)$ . The wavevector  $\vec{k}$  is related to the energy in the relative motion (i.e. the energy of the incident reduced mass particle) given by  $E_r = \frac{\hbar^2 k^2}{2\mu}$  where  $k = \mu |\vec{v}_r| / \hbar$ . Note this is the energy for the incident particle approximated as a free particle when it is far away from the potential region. We are interested in the situation after an elastic collision when the particle is again far from the potential region so that the energy  $E_r$  is the same as the incident energy. The second term in Eq. 2.10 describes scattering as a spherical wave, where  $f(k, \theta, \phi)$  indicates that there is a different probability of scattering in different directions,  $(\theta, \phi)$ .

Classically one considers an incident beam of finite width consisting of many incoming particles centered on the target region. A detector collects any scattered particles that travel into some solid angle, defined by the area

of the detector, in the direction  $[\theta, \phi]$ . The differential cross-section,  $\frac{d\sigma}{d\Omega}$ , is defined as

$$\frac{d\sigma}{d\Omega} = \frac{\text{flux scattered into the direction } \theta, \phi \text{ per unit solid angle}}{\text{flux in the incident beam per unit area}} \quad (2.11)$$

where the differential solid angle element is  $d\Omega = \sin\theta d\theta d\phi$ . Classically, flux here has units of number of atoms per second. The number of atoms per second passing through a differential area  $d\vec{S}$  is  $\vec{J} \cdot d\vec{S}$  where  $\vec{J}$  is the mass current density, which describes the number of particles passing through a unit area per unit time. In the absence of sources or sinks (no particles are created or destroyed)  $\vec{J}$  obeys the continuity equation

$$\frac{d\rho}{dt} + \vec{\nabla} \cdot \vec{J} = 0 \quad (2.12)$$

where  $\rho$  is the density of particles (the number of particles per unit volume).

To determine a quantum mechanical expression for the differential cross section, consider again our case of a single particle subject to some localized potential.  $|\psi_r|^2$  is a probability density (the probability of finding the particle at a particular place per unit volume) and can replace the classical density  $\rho$  in Eq. 2.12. In this case since  $|\psi_r|^2$  has units of probability per unit volume,  $\vec{J}$  will have units of probability per unit time per unit area. With this interpretation it can be shown [38] that  $\vec{J}$  for a particle of mass  $\mu$  has the form

$$\begin{aligned} \vec{J} &= \frac{\hbar}{2\mu i} (\psi^* \nabla \psi - \psi \nabla \psi^*) \\ &= \frac{\hbar}{\mu} \text{Im}(\psi^* \nabla \psi) \end{aligned} \quad (2.13)$$

The denominator of Eq. 2.11, using a plane wave  $\psi_r = e^{ikz}$  in Eq. 2.13 and  $d\vec{S} = dx dy \hat{z}$ , is

$$\frac{\vec{J} \cdot d\vec{S}}{dS} = \frac{\hbar k}{\mu}. \quad (2.14)$$

The numerator of Eq. 2.11 can be found using  $\psi_r = f(k, \theta, \phi) \frac{e^{ikr}}{r}$  in Eq. 2.13 and  $d\vec{S} = r^2 \sin\theta d\theta d\phi \hat{r} = r^2 d\Omega \hat{r}$  as

$$\frac{\vec{J} \cdot d\vec{S}}{d\Omega} = \frac{\hbar k |f(k, \theta, \phi)|^2}{\mu}. \quad (2.15)$$

Taking the ratio of Eq. 2.15 and Eq. 2.14 the differential cross section is

$$\frac{d\sigma}{d\Omega} = |f(k, \theta, \phi)|^2. \quad (2.16)$$

Hereafter cylindrical symmetry is assumed so  $f$  is not a function of  $\phi$ .

The total cross section is given by integrating the differential cross section over all solid angles

$$\sigma = 2\pi \int_0^\pi |f(k, \theta)|^2 \sin \theta d\theta. \quad (2.17)$$

The collisional loss cross section given in Eq. 2.1 for the loss rate constant,  $\Gamma$ , is similar to the total cross section but only accounts for collisions that induce loss from the trap. This means that instead of starting at zero for the scattering angle  $\theta$  we start from the minimum scattering angle that results in loss. This was expressed as  $\theta_{\min}$  in Eq. 2.9 and gives a cross section for loss as

$$\sigma_{\text{loss}} = 2\pi \int_{\theta_{\min}}^\pi |f(k, \theta)|^2 \sin \theta d\theta. \quad (2.18)$$

The cross section for heating collisions that do not result in trap loss is given as

$$\sigma_{\text{heat}} = 2\pi \int_0^{\theta_{\min}} |f(k, \theta)|^2 \sin \theta d\theta. \quad (2.19)$$

Note that the expressions given in Eq. 2.18 and Eq. 2.18 depend on the relative speed of collision through  $k = \mu|\vec{v}_r|/\hbar$ . For our consideration of a room temperature background gas interacting with an ultra-cold atomic cloud, there are many possible  $k$  values for collisions between a background gas particle and a trapped atom.

## 2.2 The velocity averaged collisional loss cross section

This section explains: the calculation of the velocity averaged collisional loss cross section,  $\langle \sigma_{\text{loss}} v_i \rangle_{X,i}$ ; the convergence criteria used in the calculation of the scattering amplitude,  $f(k, \theta)$ ; the form of the interaction potential; and the dependence of  $\langle \sigma_{\text{loss}} v_i \rangle_{X,i}$  on trap depth.

### 2.2.1 Calculation of $\langle \sigma_{\text{loss}} v_i \rangle_{X,i}$

The section explains how  $\langle \sigma_{\text{loss}} v_i \rangle_{X,i}$  is calculated. The beginning treatment follows Refs. [14, 15, 38]. According to Eq. 2.18, the calculation of  $\sigma_{\text{loss}}$  involves the scattering amplitude  $f(k, \theta)$ . The following consists of

a derivation for the expression given in Eq. 2.31 for the scattering amplitude. Eq. 2.7 for  $\psi_r(r, \theta, \phi)$  written in terms of spherical coordinates and the angular momentum operator squared,  $\hat{L}^2$ , is [34]

$$\frac{\hbar}{2\mu} \left[ -\frac{1}{r^2} \frac{\partial}{\partial r} \left( r^2 \frac{\partial \psi_r}{\partial r} \right) + \frac{\hat{L}^2}{r^2} \psi_r \right] + V(r) \psi_r = E \psi_r. \quad (2.20)$$

The solution  $\psi_r(r, \theta, \phi) = R_l(r) Y_{l,m}(\theta, \phi)$  is comprised of a radial and angular part. The angular part, called a spherical harmonic,  $Y_{l,m}(\theta, \phi)$ , is an eigenfunction of  $\hat{L}^2$  with  $\hat{L}^2 Y_{l,m} = l(l+1) Y_{l,m}$ . Substituting this solution for  $\psi_r(r, \theta, \phi)$  into Eq. 2.20 gives [34]

$$\frac{1}{r^2} \frac{d}{dr} \left( r^2 \frac{dR_l}{dr} \right) - \frac{l(l+1)}{r^2} R_l + \frac{2\mu}{\hbar^2} [E - V(r)] R_l = 0. \quad (2.21)$$

In our case we assume cylindrical symmetry so that  $\psi_r$  is a function of  $r$  and  $\theta$  only. For this case the spherical harmonics are proportional to the Legendre polynomials  $Y_{l,0} \propto P_l(\cos \theta)$ . Taking linear combinations for the most general solution of  $\psi_r(r, \theta)$  gives

$$\psi_r(r, \theta) = \sum_{l=0}^{\infty} (2l+1) i^l A_l R_l(r) P_l(\cos \theta) \quad (2.22)$$

where  $A_l = 1$  for a free particle and otherwise is a constant to be determined.

Eq. 2.21 for the radial part  $R_l$  can be expressed in terms of  $\psi_l(r) = kr R_l(r)$  as

$$\left[ \frac{d^2}{dr^2} + W(r) \right] \psi_l(r) = 0 \quad (2.23)$$

with

$$W(r) = k^2 - \frac{2\mu}{\hbar^2} V(r) - \frac{l(l+1)}{r^2}. \quad (2.24)$$

Note  $\psi_l(r)$  is not to be confused with  $\psi_r(r, \theta)$ .

When  $V(r) = 0$  the solution to Eq. 2.21 is [38]

$$R_l(r) = \cos(\delta_l) j_l(kr) - \sin(\delta_l) n_l(kr) \quad (2.25)$$

where  $j_l(kr)$  and  $n_l(kr)$  are the spherical Bessel and Neumann functions, respectively, and  $\delta_l$  is a real number called the partial-wave dependent phase shift. This phase shift is key for interpreting elastic scattering. For a free particle  $R_l(r) = j_l(kr)$  because the potential is zero at  $r = 0$  and the Neumann part of the function is discounted because it blows up as  $r$  approaches

zero. For our case we are interested in the solution for  $V(r) \rightarrow 0$  for  $r \rightarrow \infty$ . At  $r = 0$  we have  $V(r) \neq 0$  and so the Neumann term is retained. The asymptotic form of  $j_l(kr)$  as  $r \rightarrow \infty$  is

$$j_l(kr) \rightarrow \frac{\sin(kr - \frac{1}{2}\pi l)}{kr}. \quad (2.26)$$

The asymptotic form of  $n_l(kr)$  as  $r \rightarrow \infty$  is

$$n_l(kr) \rightarrow \frac{-\cos(kr - \frac{1}{2}\pi l)}{kr} \quad (2.27)$$

so that the asymptotic form of  $R_l(r)$  is

$$R_l(r) \rightarrow \frac{\sin(kr - \frac{1}{2}\pi l + \delta_l)}{kr}. \quad (2.28)$$

The asymptotic solution for  $\psi_r$  given in Eq. 2.10 can be matched with Eq. 2.22 with the form of  $R_l(r)$  given in Eq. 2.28. The free particle part of the solution  $e^{i\vec{k}\cdot\vec{r}}$  can be replaced by Eq. 2.22, with  $A_l = 1$  and with the form of  $R_l(r)$  given in Eq. 2.26. This gives

$$\begin{aligned} & \sum_{l=0}^{\infty} (2l+1) i^l P_l(\cos\theta) A_l \frac{\sin(kr - \frac{1}{2}\pi l + \delta_l)}{kr} \\ &= \sum_{l=0}^{\infty} (2l+1) i^l P_l(\cos\theta) \frac{\sin(kr - \frac{1}{2}\pi l)}{kr} + \frac{f(k, \theta, \phi) e^{ikr}}{r} \end{aligned} \quad (2.29)$$

The sin and cos functions can be expressed as complex exponentials and coefficients of  $e^{-ikr}$  and  $e^{ikr}$  can be matched on either side of the expression giving [38]

$$A_l = e^{i\delta_l} \quad (2.30)$$

and

$$f(k, \theta) = \frac{1}{k} \sum_{l=0}^{\infty} (2l+1) \sin(\delta_l) e^{i\delta_l} P_l(\cos\theta). \quad (2.31)$$

To determine  $f(k, \theta)$ , complex T-matrix elements need to be determined

$$T_l(k) \equiv e^{i\delta_l} \sin \delta_l. \quad (2.32)$$

The  $T_l(k)$  values can be found from the complex S-matrix elements

$$S_l(k) \equiv e^{2i\delta_l} = 1 + 2iT_l(k). \quad (2.33)$$

Finally  $S_l(k)$  can be found from the real K-matrix elements

$$K_l(k) \equiv \tan \delta_l(k). \quad (2.34)$$

The S-matrix and K-matrix elements are related by

$$S_l(k) = \frac{1 + iK_l(k)}{1 - iK_l(k)}. \quad (2.35)$$

To find  $K_l(k)$  Eq. 2.23 is expressed in terms of the logarithmic derivative

$$y_l(r) = \frac{\psi_l'(r)}{\psi_l(r)} \quad (2.36)$$

to give

$$y'(r) + y^2(r) + W(r) = 0. \quad (2.37)$$

Here the prime in Eq. 2.36 and Eq. 2.37 means differentiation with respect to  $r$ . The values  $y_l(r)$  are solved for in the limit of large  $r$  using numerical methods described in [15, 39]. The asymptotic form of the solution for  $\psi_l(r)$  given in Eq. 2.25 can be expressed in terms of  $K_l(k)$  as

$$\psi_l(r) = B_l \left[ \hat{j}_k(kr) - K_l(k) \hat{n}_l(kr) \right] \quad (2.38)$$

where  $B_l = \cos(\delta_l)$  and

$$\hat{j}_l(kr) = kr j_l(kr) \quad (2.39)$$

$$\hat{n}_l(kr) = kr n_l(kr). \quad (2.40)$$

$$(2.41)$$

Substituting Eq. 2.38 in the definition of  $y_l(r)$  given in Eq. 2.36 and solving for  $K_l(k)$  gives

$$K_l(k) = \frac{y_l(r) \hat{j}_l(kr) - \frac{d}{dr}(\hat{j}_l(kr))}{y_l(r) \hat{n}_l(kr) - \frac{d}{dr}(\hat{n}_l(kr))}. \quad (2.42)$$

Once  $K_l(k)$  is determined then  $S_l(k)$  can be found from Eq. 2.35.  $T_l(k)$  can then be found from Eq. 2.33. The scattering amplitude,  $f(k, \theta)$ , for a particular  $k$  and  $\theta$  can be found by substituting  $T_l(k)$  into Eq. 2.31 and summing over  $l$  until the convergence criteria mentioned below is met.  $f(k, \theta)$  is then substituted into Eq. 2.18 to obtain the loss cross section,  $\sigma_{\text{loss}}$ , and the integral is performed numerically over  $\theta$ . This gives  $\sigma_{\text{loss}}$  for one particular  $k = \mu v_r / \hbar \approx \mu v_i / \hbar$  value where  $v_i$  is the background particle speed

in the lab frame and we used the assumption that the trapped atom is initially stationary in the lab frame. To determine  $\langle \sigma_{\text{loss}} v_i \rangle_{X,i}$  for the trapped species  $X$  and background species  $i$  an average over all speeds  $v_i$  using a Maxwell-Boltzmann distribution is performed

$$\langle \sigma_{\text{loss}} v_i \rangle_{X,i} = 4\pi \left( \frac{m_i}{2\pi k_B T} \right)^{3/2} \int_0^\infty v_i^3 e^{-\frac{m_i v_i^2}{2k_B T}} \sigma_{\text{loss}} \left( \frac{\mu |v_i|}{\hbar} \right) dv_i \quad (2.43)$$

which requires another numerical integration over  $v_i$ . Here  $\sigma_{\text{loss}}$  given in Eq. 2.18 depends on the background gas speed  $v_i$  through  $\theta_{\text{min}}$  and the dependence of the scattering amplitude,  $f(k, \theta)$  on  $k$ .

In summary, the physical parameters to input into the calculation for  $\langle \sigma v \rangle$  are the masses of the background gas species and the trapped atom species, the interaction potential  $V(r)$ , the temperature of the background gas, and the trap depth. There are no free parameters in the calculation, however there are choices regarding convergence criteria for the summation of Eq. 2.31 and the integrals in Eq. 2.18 and Eq. 2.43. The starting and ending interatomic distance, typically 0.5 and 50 Bohr radii, respectively, and the number of steps, typically 10000, to use in the algorithm to solve for  $y_l(r)$  must also be specified in the code.

### 2.2.2 Convergence criteria

The total cross section can be expressed as [37]

$$\sigma_{\text{tot}} = \frac{4\pi}{k^2} \sum_{l=0}^{\infty} (2l+1) |T_l(k)|^2. \quad (2.44)$$

The total cross section is used to determine the maximum  $l$ , denoted  $l_{\text{max}}$ , that is needed for calculation of Eq. 2.31. Successive summations for the total cross section were compared as a convergence criterion using

$$\left( \sum_{l=0}^{l_{\text{max}}} (2l+1) |T_l(k)|^2 - \sum_{l=0}^{l_{\text{max}}-1} (2l+1) |T_l(k)|^2 \right) < 10^{-2} \sum_{l=0}^{l_{\text{max}}} (2l+1) |T_l(k)|^2. \quad (2.45)$$

Another convergence criterion used together with Eq. 2.45 to determine  $l_{\text{max}}$  for a given  $k$  is based on the argument found in [37]. Consider a classical particle coming towards the potential region with some impact parameter,  $b$ , as shown in Fig. 2.2. The angular momentum  $\vec{L} = \vec{r} \times \vec{p}$  has magnitude  $L = pb$ . Quantum mechanically  $L = \hbar \sqrt{l(l+1)} \approx \hbar l$  and the momentum  $p = \hbar k$ . Equating the classical and quantum expressions for angular momentum and

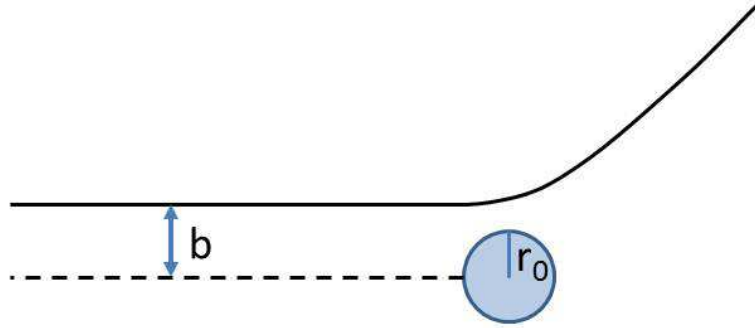


Figure 2.2: An incident particle with impact parameter  $b$  comes towards a potential region of size  $r_0$  and scatters. Classically if  $b > r_0$  then the particle will not scatter.

momentum gives  $\hbar l \approx pb \approx \hbar kb$ . Let  $r_0$  be the radius, centered at the scattering potential, beyond which the potential is negligible. A classical picture is that the impact parameter,  $b \approx \frac{\hbar l}{p}$  needs to be smaller than  $r_0$  for scattering to occur. For low energy,  $b$  is large except for  $l = 0$ , so there is only s-wave ( $l = 0$ ) scattering and only  $l = 0$  has a non-zero phase shift. For high energy, the maximum  $l$  needed in Eq. 2.31 to satisfy  $b > r_0$  is larger. In other words, more  $l$  values contribute to the scattering and have non-zero phase shifts. An impact parameter,  $b > r_0$ , corresponds to  $l > kr_0$ . This condition can be used to determine the maximum quantum number  $l$  needed for convergence in the summation of Eq. 2.31. Here  $\hbar k = \mu v_r$ , where  $v_r$  is the relative speed (taken to be the incoming background gas speed). This gives  $l > \frac{\mu v_r r_0}{\hbar}$ . The criterion  $l > [0.5 \text{ s} \cdot \text{m}^{-1}] v_r$  was used, meaning that  $\frac{\mu r_0}{\hbar} = 0.5 \text{ s/m}$  which corresponds roughly to  $r_0$  of 25 bohr radii, or 1 nm, using a reduced mass between  $^{87}\text{Rb}$  and  $^{40}\text{Ar}$ . A criteria of  $l > 2v_r$  was also tried but the velocity averaged collisional loss cross section given differed by less than 0.1%, calculated for a 2.2 K trap depth and also for the total cross section. A typical maximum velocity for these calculations is 900 m/s and the maximum  $l$  needed to satisfy Eq. 2.45 for that velocity is around 700.

### 2.2.3 Interaction potential

The form of the potential used in the calculation of  $\langle \sigma_{\text{loss}} v_i \rangle_{X,i}$  with both collisional partners in their ground state is  $V(r) = \epsilon \left( \frac{(r_m)^{12}}{r^{12}} - 2 \frac{(r_m)^6}{r^6} \right) =$

$\frac{C_{12}}{r^{12}} - \frac{C_6}{r^6}$ . Here  $r$  is the internuclear separation,  $\epsilon$  is the depth of the potential well, and  $r_m$  is the internuclear separation at which the minimum of the potential occurs [40]. The  $C_6$  and  $C_{12}$  coefficients are more commonly referred to. This form is called a Lennard-Jones potential. The  $r^6$  term describes an attractive force and arises due to long range interaction between the atoms. The  $r^{12}$  term describes a short range repulsive term and is chosen to have a  $r^{12}$  dependence for computational ease since it is the square of  $r^6$  [41].

The following is a simple argument from [42] for why the attractive part of the interaction potential energy term,  $V(r)$ , has a  $\frac{1}{r^6}$  dependence for two atoms in their ground state. Fig. 2.3 shows two hydrogen atoms where the protons are situated at A and B and their respective electrons are at  $\vec{r}_A$  and  $\vec{r}_B$ . The distance between the protons is given by  $\vec{R}$ . The potential energy

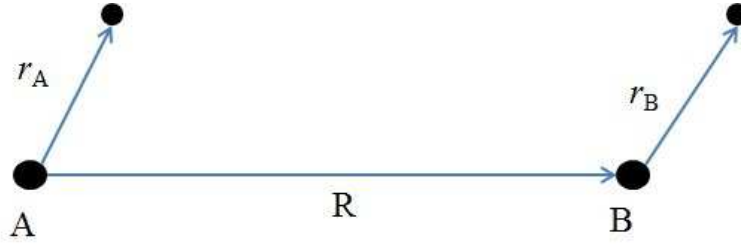


Figure 2.3: A cartoon drawing of protons and electrons for two hydrogen atoms. This figure was patterned after that found in [42]. The protons, A and B, are separated by a distance,  $|\vec{R}|$ . The electrons associated with proton A or B are a distance  $|\vec{r}_A|$ , or  $|\vec{r}_B|$  away, respectively.

arising from interaction between the hydrogen atoms is given as

$$V = \frac{e^2}{|\vec{R}|} + \frac{e^2}{|\vec{R} + \vec{r}_B - \vec{r}_A|} - \frac{e^2}{|\vec{R} + \vec{r}_B|} - \frac{e^2}{|\vec{R} - \vec{r}_A|}. \quad (2.46)$$

Taking  $|\vec{R}|$  to be much larger than  $|\vec{r}_A|$  and  $|\vec{r}_B|$  allows Eq. 2.46 to be expanded using  $\frac{|\vec{r}_A|}{|\vec{R}|}$  and  $\frac{|\vec{r}_B|}{|\vec{R}|}$  being small. This expansion gives [42]

$$V = e^2 \left( \frac{\vec{r}_A \cdot \vec{r}_B}{R^3} - \frac{3(\vec{r}_A \cdot \vec{R})(\vec{r}_B \cdot \vec{R})}{R^5} \right). \quad (2.47)$$

The interaction potential  $V$  when  $\vec{R}$  is taken to be along the  $z$ -axis is

$$V = \frac{e^2}{R^3} (x_A x_B + y_A y_B - 2z_A z_B). \quad (2.48)$$

For simplicity we will denote the ground  $S$  state of atom A and atom B to be  $|S_A\rangle$  and  $|S_B\rangle$ , respectively. The next excited  $P$  state we will label similarly  $|P_A\rangle$  and  $|P_B\rangle$ . The first order correction to the energy with both atoms being in the  $S$  (ground) state is  $\langle S_A | \langle S_B | V | S_B \rangle | S_A \rangle$ . For the sake of argument we will just take the  $x_A x_B$  term of  $V$  giving  $\langle S_A | x_A | S_A \rangle \langle S_B | x_B | S_B \rangle$ . This means the first order energy correction is zero since the  $S$  state is symmetric. To get a non zero correction to the energy second order perturbation theory is needed which will involve, for example, a term like  $|\frac{e^2}{R^3} \langle P_A | x_A | S_A \rangle \langle P_B | x_B | S_B \rangle|^2$ . This term is non zero and gives a  $\frac{1}{R^6}$  dependence for the energy correction due to interaction between two atoms in their ground states. A physical interpretation of the  $1/r^6$  dependence of the potential between ground state atoms is that it is the interaction energy between two induced dipoles.

The  $C_6$  constant can be found from the dynamic electric polarizabilities,  $\alpha^A(i\omega)$  and  $\alpha^B(i\omega)$  of atom A and B, respectively, as

$$C_6 = \frac{3}{\pi} \int_0^\infty \alpha^A(i\omega) \alpha^B(i\omega) d\omega. \quad (2.49)$$

The atomic polarizabilities can in turn be found from semi-empirical oscillator strength distributions [43, 44].

#### 2.2.4 The dependence of $\langle \sigma_{\text{loss}} v_i \rangle_{X,i}$ on trap depth, $U$

It is important to note that  $\langle \sigma_{\text{loss}} v_i \rangle_{X,i}$  is a function of trap depth through the limits of integration in Eq. 2.18. Intuitively one would predict that  $\langle \sigma_{\text{loss}} v_i \rangle_{X,i}$  will decrease as trap depth increases. This is because the larger the kinetic energy needed for a trapped atom to escape the trap the less probable it is that a collision with a background gas particle will cause loss. In the limit of zero trap depth the loss cross section becomes the total cross section. Figure 2.4 shows the variation of  $\langle \sigma_{\text{loss}} v_{\text{Ar}} \rangle_{87\text{Rb}, 40\text{Ar}}$  with trap depth. For this calculation both species are taken to be in the ground state and the potential used is  $V(r) = \frac{C_{12}}{r^{12}} - \frac{C_6}{r^6}$ . The coefficients were taken to be  $C_6 = 280 E_{\text{H}} a_{\text{B}}^6$  and  $C_{12} = 8.6 \times 10^7 E_{\text{H}} a_{\text{B}}^{12}$ , where  $E_{\text{H}} = 4.35974 \times 10^{-18}$  J and  $a_{\text{B}}$  is the Bohr radius [14, 45]. The  $C_6$  value given here is calculated in Ref. [45] from optical data. The  $C_{12}$  coefficient is chosen to correspond to a  $50 \text{ cm}^{-1}$  well depth as per rough estimate from Dr. Roman Krems

in the UBC chemistry department. As shown in Refs. [14, 15], the value of  $\langle\sigma_{\text{loss}}v_{\text{Ar}}\rangle_{87\text{Rb},40\text{Ar}}$  is fairly insensitive to large variations in the  $C_{12}$  value chosen. The points superimposed on the curve are experimental data which will be discussed in the next chapter.

The following few paragraphs discuss the need for a quantum mechanical scattering theory calculation at low trap depths. For large trap depths classical calculation predicts a  $U^{-1/6}$  dependence of the loss cross section on trap depth for a long range potential interaction of  $V(r) = -\frac{C_6}{r^6}$  [32, 46, 47]. For small trap depths, where small angle scattering can induce loss, a quantum calculation is needed for the loss cross section. This is due to the fundamental uncertainty in the scattering angle so that scattering at angles close to this uncertainty needs to be treated quantum mechanically [48]. The kinetic energy,  $\epsilon_d$ , imparted to a trapped atom for angles within the quantum regime is approximated in [49] as

$$\epsilon_d = \frac{4\pi\hbar^2}{m_t\sigma} \quad (2.50)$$

where  $m_t$  is the mass of the trapped atom species and  $\sigma$  is the total cross section. For collisions between  $^{87}\text{Rb}$  and  $^{40}\text{Ar}$ , both in their ground state,  $\epsilon_d$  is estimated to be 8.9 mK.

For hard sphere scattering the scattering potential is infinite inside some radius,  $d$ , and zero outside this radius. The classical total collision cross section is  $\sigma = \pi d^2$  [48]. The quantum mechanical total cross section is two or four times the classical value, depending on the collisional energy [48]. The fact that the quantum collisional cross section is larger than the classical cross section is in analogy to light scattering off of a ball bearing. Classically a shadow the size of the ball would be observed, but quantum mechanically fringes are observed past the size of the ball bearing. Our case is not that of hard sphere scattering but this idea is useful to understand why below  $\epsilon_d$  the slope of the  $\langle\sigma_{\text{loss}}v_{\text{Ar}}\rangle_{87\text{Rb},40\text{Ar}}$  versus trap depth curve is greater than for the classical regime of the curve. The loss cross section is limited to the total cross section so the slope must then decrease as trap depth tends to zero.

An interesting consideration for the shape of the  $\langle\sigma_{\text{loss}}v_{\text{Ar}}\rangle_{87\text{Rb},40\text{Ar}}$  versus trap depth curve is to consider the trap loss process as a chemical reaction. The reaction could be expressed as  $A + B \rightarrow C + B$  where  $A$  is a trapped atom,  $B$  is a background gas particle, and  $C$  is the trapped atom being lost from the trap. The rate constant,  $k$ , for a chemical reaction depends on the activation energy,  $E_a$ , according to  $k \propto e^{-E_a/RT}$  where  $T$  is the temperature of the reactants and  $R$  is the gas constant. If  $\langle\sigma_{\text{loss}}v_{\text{Ar}}\rangle_{87\text{Rb},40\text{Ar}}$

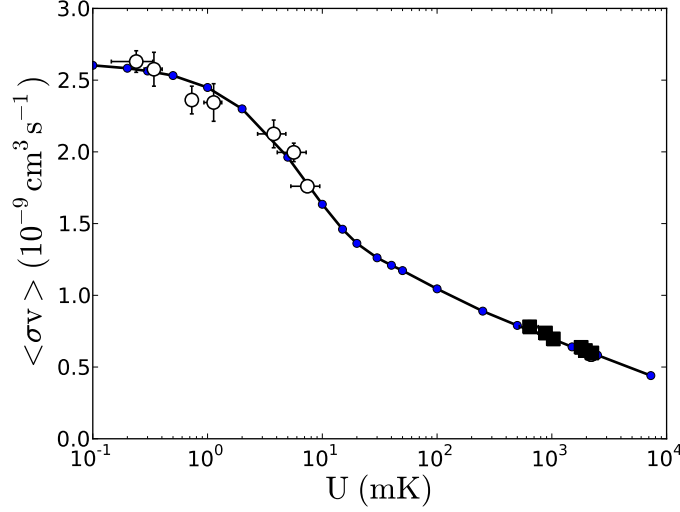


Figure 2.4: The velocity averaged collisional loss cross section plotted versus trap depth showing a decrease in the loss cross section with increasing trap depth. As trap depth increases the kinetic energy required to leave the trap grows and the probability of a collision with a background gas particle imparting sufficient energy to leave the trap decreases. The curve is generated by numerically calculating  $\langle \sigma_{\text{loss}} v_{\text{Ar}} \rangle_{^{87}\text{Rb}, ^{40}\text{Ar}}$  at discrete trap depths for  $^{87}\text{Rb}$  as the trapped species and  $^{40}\text{Ar}$  as the background species both in their ground state. The potential used in the calculation is  $V(r) = \frac{C_{12}}{r^{12}} - \frac{C_6}{r^6}$ . The coefficients were taken to be  $C_6 = 280 E_{\text{H}} a_{\text{B}}^6$  and  $C_{12} = 8.6 \times 10^7 E_{\text{H}} a_{\text{B}}^{12}$  where  $E_{\text{H}} = 4.35974 \times 10^{-18}$  J and  $a_{\text{B}}$  is the Bohr radius [14, 45]. The points superimposed on the curve are experimental data.

is likened to the rate constant and the trap depth to the activation energy then the expected dependence of  $\langle \sigma_{\text{loss}} v_{\text{Ar}} \rangle_{^{87}\text{Rb}, ^{40}\text{Ar}}$  on trap depth would be  $\langle \sigma_{\text{loss}} v_{\text{Ar}} \rangle_{^{87}\text{Rb}, ^{40}\text{Ar}} \propto e^{-U}$ . In the case of collisions of background gas particles with trapped atoms the temperature of the background gas ( $\approx 294$  K) is very different from the trapped atom temperature ( $150 \mu$  K). This means that the reactants in our proposed chemical reaction are not in thermal equilibrium with each other and we do not see an exponential dependence of  $\langle \sigma_{\text{loss}} v_{\text{Ar}} \rangle_{^{87}\text{Rb}, ^{40}\text{Ar}}$  on trap depth.

The calculation of  $\langle \sigma_{\text{loss}} v_{\text{Ar}} \rangle_{^{87}\text{Rb}, ^{40}\text{Ar}}$  depends on what state the background atoms and trapped atoms are in. The long-range form of the potential when  $^{87}\text{Rb}$  is excited and  $^{40}\text{Ar}$  is in its ground state is the same form as when both atoms are in their ground state,  $V(r) = \frac{C_{12}}{r^{12}} - \frac{C_6}{r^6}$ , however the  $C_{12}$  and  $C_6$  values are different. If  $a$  is the fraction of trapped atoms in the excited state, in for example a MOT, then the expected collision cross section is

$$\langle \sigma_{\text{loss}} v_{\text{Ar}} \rangle_{^{87}\text{Rb}, ^{40}\text{Ar}} = (1 - a) \langle \sigma_{\text{loss},g} v_{\text{Ar}} \rangle_{^{87}\text{Rb}, ^{40}\text{Ar}} + a \langle \sigma_{\text{loss},e} v_{\text{Ar}} \rangle_{^{87}\text{Rb}, ^{40}\text{Ar}}. \quad (2.51)$$

The subscript  $e$  and  $g$  refer to when  $^{87}\text{Rb}$  is in the excited state or the ground state, respectively.

The next chapter describes the experimental verification of the dependence of the velocity averaged collisional loss cross section on trap depth.  $^{87}\text{Rb}$  was the trapped atom species and  $^{40}\text{Ar}$  was the background species. Further reference to  $\sigma$  implicitly means the loss cross section  $\sigma_{\text{loss}}$  unless otherwise noted.

## Chapter 3

# Experimental verification of the dependence of the loss cross section on trap depth

The first section of this chapter describes how the velocity averaged collisional loss cross section,  $\langle\sigma v_i\rangle_{X,i}$ , due to collisions between trapped atoms of type  $X$  and background gas of species  $i$  is measured. In our experiments we used  $^{87}\text{Rb}$  as the trapped species,  $X$ , and  $^{40}\text{Ar}$  as the background species  $i$ . The velocity averaged collisional loss cross section  $\langle\sigma v_{\text{Ar}}\rangle_{^{87}\text{Rb},^{40}\text{Ar}}$  was calculated for a range of trap depths and measured previously by members of our lab using a magnetic trap [14, 15]. The magnetic trap used could obtain trap depths up to 10 mK. The work performed for this thesis was the measurement of  $\langle\sigma v_{\text{Ar}}\rangle_{^{87}\text{Rb},^{40}\text{Ar}}$  at larger trap depths using a MOT. A technique adapted from Hoffmann et al. [16] to measure the trap depth of a MOT is described. It is also proposed that the dependence of  $\langle\sigma v_i\rangle_{X,i}$  on trap depth can be used as a measurement technique for trap depth. The work described in this chapter is also reported in [17].

### 3.1 Experimental apparatus

Our apparatus consisted of optics and a vacuum apparatus to produce a 3D MOT as well as to introduce a background gas to the 3D MOT. The  $5^2S_{1/2}$  to  $5^2P_{3/2}$  transition was used for trapping of either  $^{85}\text{Rb}$  or  $^{87}\text{Rb}$ . The pump was chosen to be resonant with the  $F = 2$  to  $F' = 3$  transition for  $^{87}\text{Rb}$  or the  $F = 3$  to  $F' = 4$  transition for  $^{85}\text{Rb}$ . The repump was chosen to be resonant with the  $F = 1$  to  $F' = 2$  transition for  $^{87}\text{Rb}$  or the  $F = 2$  to  $F' = 3$  transition for  $^{85}\text{Rb}$ . A schematic of the optical setup is shown in Fig. 3.1. On a separate table, shared among several experiments, external cavity diode lasers generate laser light locked 180 MHz below the pump and repump transitions using saturated absorption signals [50, 51]. The pump light was fibered over to the experimental table where it injected a diode

laser amplifier (fiber FC1) to provide more power for the experiment than was sent in the fiber. The repump light in fiber FC2 was not amplified. Double pass acousto-optical modulator (AOM) setups were used to bring the pump and repump frequencies from the fibers to the values used in the experiment [52]. The frequency shifted pump and repump light were combined together and sent to the MOT optics.

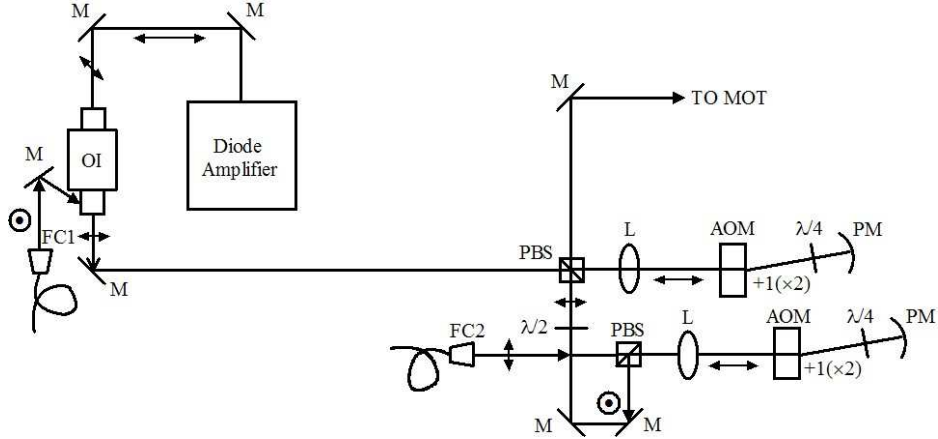


Figure 3.1: A schematic of the optical setup used to produce the pump and repump light for the MOT used in the loss cross section measurement experiment. Light from the master table was used to inject a diode amplifier via fiber FC1. An acousto-optical modulator (AOM) in double pass configuration was used to bring the output of the amplifier from 180 MHz to 12 MHz below the pump resonance. Repump light from fiber FC2 from the master table was also brought up to resonance using an AOM in double pass configuration. The pump and repump beams were combined and sent towards the MOT optics. M: mirror, L: lens (PCX 300 mm), OI: optical isolator, PM: parabolic mirror 300mm focal length, Q: quarter wave plate, H: half wave plate, PBS: polarizing beam splitter.

A retroreflected 3D MOT configuration was used with a maximum six beam total power of 18.3 mW for the pump and 0.3 mW for the repump. The  $1/e^2$  horizontal (vertical) diameter of the MOT beams was 7.0 (9.5) mm and was measured with a Coherent LaserCam-HR beam diagnostic camera. This corresponds to a maximum available pump intensity of  $34.5 \text{ mW/cm}^2$ . Further increases in pump and repump intensity would increase the MOT atom number. As saturation occurs and light assisted collisional losses grow

the atom number would eventually decrease with increasing intensity.

The axial magnetic field gradient used for the MOT was 27.9(0.3)G/cm ( $2.79(0.03) \times 10^{-3}$  T/cm). To achieve different MOT trap depths different pump intensities and detunings were selected with the AOM used for the pump light. A rectangular glass cell of dimensions 1 cm by 1cm by 3.5 cm under vacuum was used. Rb vapour was introduced into the system by running current through a Rb dispenser (Alvatec Rb-20). The system also contains an ion pump (PS-100 Thermionics) and a non-evaporable getter pump (SAES getters).

To introduce Ar into the system, a portable station was attached to a valve on the MOT vacuum chamber by a flexible bellows. This station (called the ‘bakeout station’) has a turbo pump (TV-70 Varian), a scroll pump (SH 100, Varian), a residual gas analyzer (RGA) (RGA200, Standford Research Systems), an ion gauge (843 Varian), and a leak valve (951-5106 Varian). Ar could be introduced in the MOT region through the leak valve while the pressure of Ar was measured with the RGA. The residual gas analyzer was about 1 m away from the trapped atoms. This could result in the pressure of Ar at the trapped atoms not being the same as read by the RGA. This effect, however, is expected to be minimal since both the RGA and the trapped atoms were located at the same distance, of approximately 1 m, from the leak valve where argon was introduced. Also, the RGA and the trapped atoms were roughly the same distance from the turbo and scroll pumps. The ion pump on the apparatus close to the trapped atoms was turned off while argon was being added to minimize pressure differentials between the trapped atoms and the RGA.

### 3.2 Measurement of $\langle \sigma v_{\text{Ar}} \rangle_{^{87}\text{Rb}, ^{40}\text{Ar}}$

The velocity averaged collisional loss cross section  $\langle \sigma v_{\text{Ar}} \rangle_{^{87}\text{Rb}, ^{40}\text{Ar}}$  can be measured for a trap of a certain trap depth by measuring the background collision loss rate constant,  $\Gamma$ , at various measured densities,  $n_{\text{Ar}}$ , of  $^{40}\text{Ar}$ . Eq. 2.1 predicts that plotting  $\Gamma$  vs  $n_{\text{Ar}}$  will give a linear relationship with a slope of  $\langle \sigma v_{\text{Ar}} \rangle_{^{87}\text{Rb}, ^{40}\text{Ar}}$ . The velocity averaged collisional loss cross section,  $\langle \sigma v_{\text{Ar}} \rangle_{^{87}\text{Rb}, ^{40}\text{Ar}}$ , was measured in this manner for different trap depths of the MOT. As already mentioned, the different trap depths were attained by changing the intensity and detuning of the pump light. The dependence of trap depth on detuning and intensity is discussed further in section 3.5. The technique for measuring the loss rate constant,  $\Gamma$ , in our magnetic and magneto-optical trap will be discussed next.

### 3.2.1 Measurement of $\Gamma$ for a MOT

In a MOT when the magnetic field is first turned on, atoms will start to accumulate in the intersection of the six laser beams comprising the MOT. The fluorescence from the trapped atoms can partially be captured by a lens and focused onto a photodiode. The photodiode voltage,  $V(t)$ , is proportional to the number of the atoms in the MOT,  $N(t)$ , where we assume

$$V(t) = \alpha\gamma_{\text{sc}}N(t). \quad (3.1)$$

Here  $\alpha$  is a proportionality constant relating the efficiency of collecting the photons being fluoresced by the atoms onto the photodetector and the conversion efficiency of photons to voltage by the photodetector. The scattering rate,  $\gamma_{\text{sc}}$ , is the rate at which an atom in the MOT scatters photons and is dependent on the frequency and intensity of the light.

For the purposes of obtaining the loss rate constant,  $\Gamma$ , we recorded the fluorescence voltage on the photodetector as a function of time as the atoms accumulate in a MOT until a steady state voltage (atom number) is reached. Time  $t = 0$  was set to be when the magnetic field was turned on with the repump and pump light already on. Fig. 3.2 shows an example of a MOT loading curve from which  $\Gamma$  can be determined [17]. This loading curve can be fit to an equation proportional to Eq. 1.6 and  $\Gamma$  can be determined. For determination of  $\Gamma$  we do not need to know  $\alpha$  and  $\gamma_{\text{sc}}$ .

### 3.2.2 Measurement of $\Gamma$ for a magnetic trap

A magnetic trap is initially loaded by turning off the MOT light and turning up the current to the magnetic coils to increase the magnetic field gradient. A magnetic trap starts off with its maximal atom number which then decays over time. Eq. 1.15 models this decay with

$$\frac{N(t)}{N(0)} = e^{-\Gamma t} \quad (3.2)$$

where  $N(t)$  is the number of atoms in the magnetic trap after a hold time,  $t$ , from initial loading of  $N(0)$  atoms. Consider instead the ratio  $\frac{N(t)}{N_{\text{MOT}}}$  where  $N_{\text{MOT}}$  is the steady state number of atoms in the MOT before loading into the magnetic trap. The initial number in the magnetic trap is proportional to the steady state value in the MOT,  $N(0) \propto N_{\text{MOT}}$ , so that

$$\frac{N(t)}{N_{\text{MOT}}} \propto \frac{N(t)}{N(0)} = e^{-\Gamma t}. \quad (3.3)$$

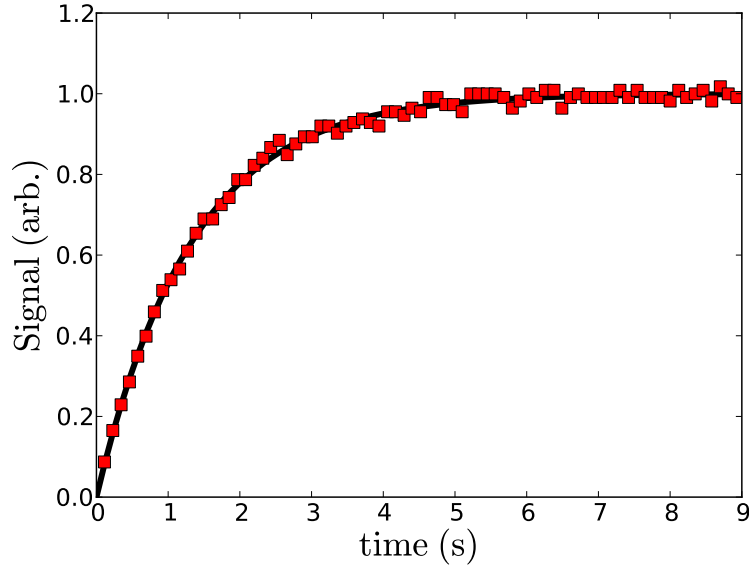


Figure 3.2: The fluorescence signal of the atoms accumulating in a MOT as a function of time from the turn on of the magnetic field.

Fig. 3.3 shows an example set of data taken to determine  $\frac{N(t)}{N_{\text{MOT}}}$  for a particular hold time,  $t$ . The experimental sequence is as follows:

- (a) First the fluorescence voltage due to the steady state atom number in our MOT was recorded.
- (b) The light was turned off and the magnetic field was increased to load atoms into a magnetic trap. The atoms were held in the magnetic trap for some hold time,  $t$ .
- (c) The MOT light was turned back on and the magnetic field was put back to the settings used for the MOT. The MOT was then allowed to load for a short time.
- (d) The magnetic field was turned off to let the trapped atoms escape. The MOT light was left on to record a background level.
- (e) The magnetic field was turned back on allowing the MOT to reload

completely before starting at step (a) again. Each cycle a different hold time was used.

Step c is needed because a magnetic trap has no light and the atoms do not fluoresce so that only background light is detected on the photodetector. In order to see how many atoms are left in the magnetic trap we turned the MOT conditions back on to detect the fluorescence. Because there are some atoms there to start with from the magnetic trap the fluorescence voltage will be higher than when loading the MOT initially.

We are interested in the ratio of the voltage corresponding to the number of atoms in the magnetic trap,  $V_{\text{MT}}(t)$ , to the voltage in the steady state MOT,  $V_{\text{MOT}}$ . Both of these observables are labelled in Fig. 3.3. From Eq. 3.1 and Eq. 3.3 we have

$$\frac{V_{\text{MT}}(t)}{V_{\text{MOT}}} = \frac{N(t)}{N_{\text{MOT}}} \propto \frac{N(t)}{N(0)} = e^{-\Gamma t}. \quad (3.4)$$

By measuring  $\frac{V_{\text{MT}}(t)}{V_{\text{MOT}}}$  for different hold times and then fitting to an equation proportional to  $e^{-\Gamma t}$  we could determine  $\Gamma$ . An example result is shown in Fig. 3.4. Each data point in Fig. 3.4 came from a sequence as described above, and as shown in Fig. 3.3. This sequence requires loading of the MOT, transfer to the magnetic trap, waiting a certain hold time, and then measuring the fraction  $\frac{V_{\text{MT}}(t)}{V_{\text{MOT}}}$ . The process is then repeated for the next hold time. The data shown in Fig. 3.4 was not averaged. This method of determining the trapped atom number decay rate in a magnetic trap assumes that the same fraction of atoms from the MOT are loaded into the magnetic trap for each hold time sequence. Typically approximately 50% of the atoms can be transferred from the MOT to the magnetic trap. The fraction loaded into the magnetic trap depends on various experimental factors such as trap depth, the overlap of the MOT trapped atom cloud with the exact location of the magnetic field zero, experimental timing, and the energy states of the atoms. These factors should be consistent through out the experiment. Averaging could, however, reduce the error in the loss rate constant,  $\Gamma$ , due to this assumption, as well as any random noise.

### 3.2.3 Results of $\Gamma$ vs $n_{\text{Ar}}$ measurement

Fig. 3.5 shows the loss rate constant versus argon density,  $\Gamma$  vs  $n_{\text{Ar}}$ , for two different trap depths obtained using a magnetic trap and a MOT. The relationship is linear and the slope,  $\langle \sigma v_{\text{Ar}} \rangle_{87\text{Rb}, 40\text{Ar}}$ , is larger for the smaller trap depth of the magnetic trap as predicted. Each loss rate constant,  $\Gamma$ ,

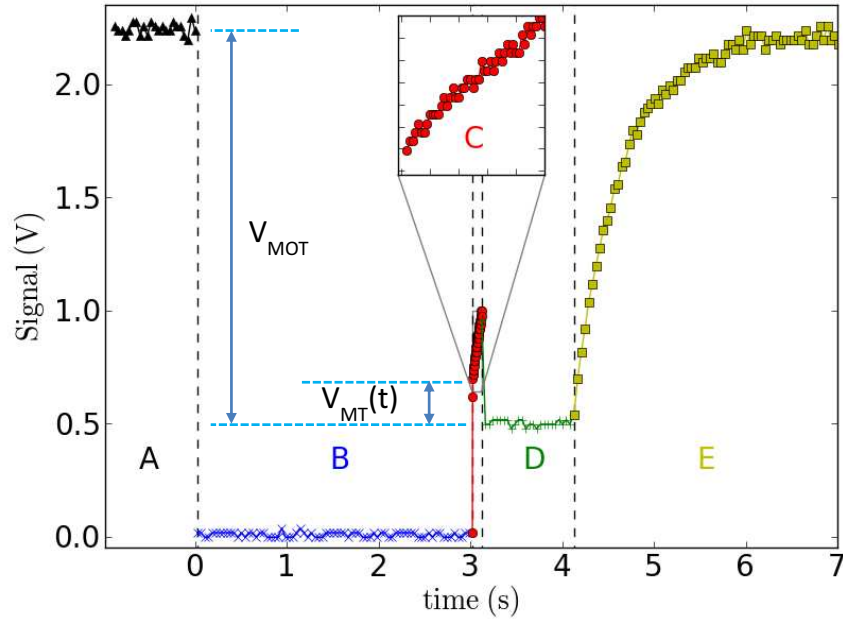


Figure 3.3: An example of data taken to determine  $\frac{N(t)}{N_{\text{MOT}}}$  for a certain hold time,  $t$ , in the magnetic trap. A) First the fluorescence voltage is recorded for a MOT in steady state. B) Atoms are loaded into the magnetic trap by turning off the MOT light and ramping up the magnetic field. The atoms are held in the magnetic trap for a hold time,  $t$ . C) The MOT light is turned back on and the magnetic field set to the MOT setting. The MOT is allowed to load for a short amount of time in order to get a line that one can use to extrapolate the fluorescence voltage when the MOT light was first turned back on. D) The magnetic field is turned off while the light is left on which dumps the atoms from the trap. E) The magnetic field is turned back on to its MOT setting and the MOT is reloaded back to its steady state atom number. The difference between voltage levels D and the start of C, labelled  $V_{\text{MT}}(t)$ , is proportional to the number of atoms in the magnetic trap,  $N(t)$ , after hold time,  $t$ . The difference between voltage levels A and D, labelled  $V_{\text{MOT}}$ , is proportional to the number of atoms in the MOT,  $N_{\text{MOT}}$ . As shown here the hold time was long and not many atoms remained in the magnetic trap.

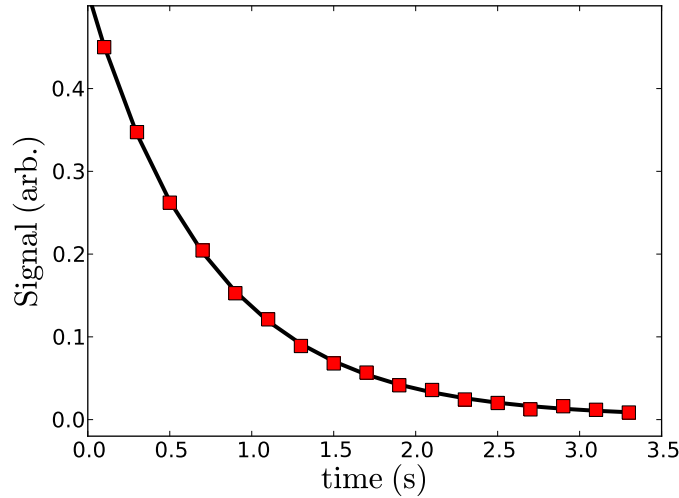


Figure 3.4: The number of atoms in the magnetic trap divided by the original steady state number in the MOT,  $\frac{N(t)}{N_{\text{MOT}}}$ , measured as a function of hold time,  $t$ . Each point is generated as described in Fig. 3.3. The data is fit to an equation proportional to  $e^{-\Gamma t}$  to determine the background loss rate constant,  $\Gamma$ .

measurement shown for a magnetic trap is determined from a fit of the atom number to a single decay curve as described in subsection 3.2.2. The error bars for  $\Gamma$  are based on the fit results for  $\Gamma$ . The error bars increase with increasing argon density because the atom number in the MOT decreases as the density of argon increases. This means that fewer atoms are loaded into the magnetic trap as argon density increases and the signal to noise ratio decreases. No averaging was performed in the data shown in Fig. 3.5. Improvements in the error of  $\Gamma$  for the magnetic trap could be made by averaging many decay curves.

The loss rate constant for the MOT data shown in Fig. 3.5 is determined by fitting a single loading curve, as described in subsection 3.2.1, to a form proportional to  $(1 - e^{-\Gamma t})$ , following Eq. 1.6. Though not visible on the graph, the error bars for  $\Gamma$  for the MOT data shown increase with increasing argon density. Again this is because the MOT atom number decreases and the signal to noise ratio of the loading curve decreases. No error bars were

assigned to the density of argon because the calibration error of the residual gas analyzer is not known and drifts with time. The error in argon density measurement causes error in the absolute measurement of  $\langle\sigma v_{\text{Ar}}\rangle_{^{87}\text{Rb},^{40}\text{Ar}}$ . Measuring  $\Gamma$  vs  $n_{\text{Ar}}$  provides a method of measuring  $\langle\sigma v_{\text{Ar}}\rangle_{^{87}\text{Rb},^{40}\text{Ar}}$  for a

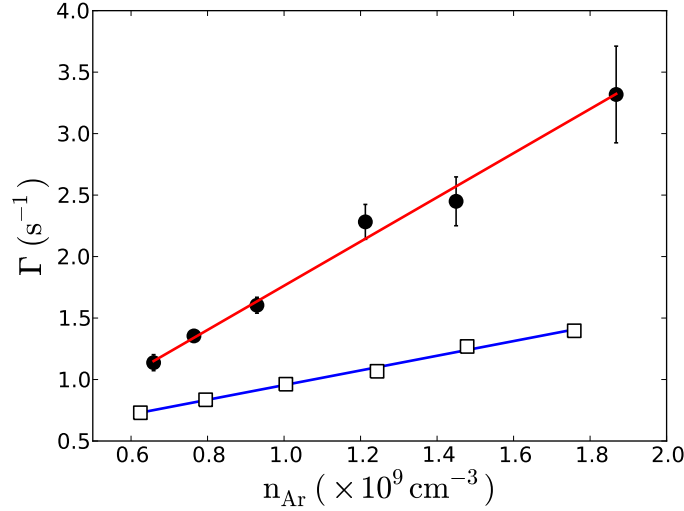


Figure 3.5: The background loss rate constant,  $\Gamma$ , is measured for a MOT (squares) and a magnetic trap (circles) as a function of the density of argon  $n_{\text{Ar}}$ . The density of argon was measured using a residual gas analyzer as described in section 3.1. The slope of  $\Gamma$  vs  $n_{\text{Ar}}$  is equal to the velocity averaged cross section for loss between trapped  $^{87}\text{Rb}$  atoms and  $^{40}\text{Ar}$  background atoms  $\langle\sigma v_{\text{Ar}}\rangle_{^{87}\text{Rb},^{40}\text{Ar}}$ . The slope for the magnetic trap is greater than for a MOT because the magnetic trap has a smaller trap depth and the probability of background collisions causing loss is greater.

given trap depth.  $\langle\sigma v_{\text{Ar}}\rangle_{^{87}\text{Rb},^{40}\text{Ar}}$  was measured for a range of trap depths accessible by our magnetic trap (0 - 10 mK) and our MOT (500 mK to 2 K). The trap depth of a magnetic trap can be calculated as described in section 1.2.2. By varying the magnetic trap gradient different trap depths could be chosen. The trap depths for various MOT settings was determined using the ‘catalysis method’ described in the next section.

### 3.3 MOT trap depth determination by the ‘catalysis method’

Fig. 3.6 shows a mechanism for imparting kinetic energy to trapped atoms [16]. Two cold ground state atoms in the trap separated by a certain inter-nuclear separation are photo-associated by a ‘catalysis’ laser to a repulsive molecular potential. The atoms quickly move apart picking up kinetic energy and then spontaneously emit back to the ground state. The kinetic energy picked up by each atom in the case of homonuclear collisions is  $h\Delta/2$ .  $\Delta$  is the detuning of the catalysis laser above the atomic resonance between the ground and the excited state of an isolated atom (in our case  $5^2S_{1/2}$  to  $5^2P_{3/2}$  for  $^{87}\text{Rb}$ ). If  $h\Delta/2 > U$ , where  $U$  is the trap depth, then the catalysis laser will cause loss of the atoms from the trap.

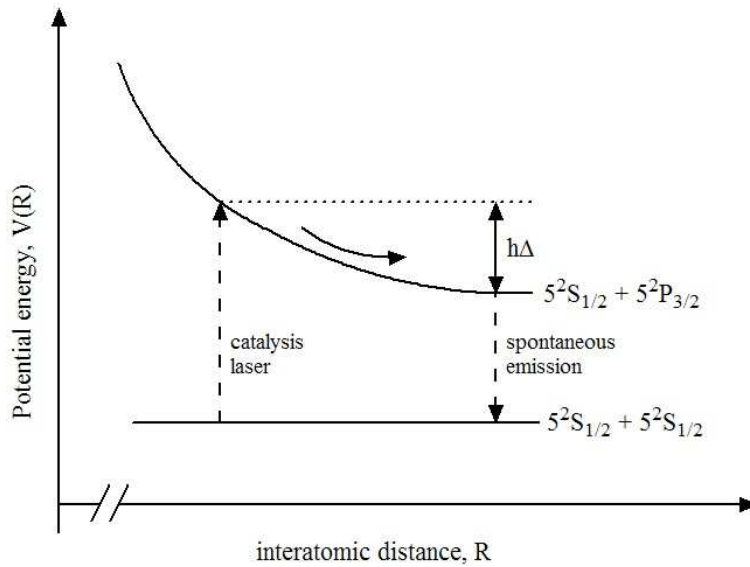


Figure 3.6: A ‘catalysis laser’ excites the ground state atoms to a repulsive excited molecular potential. The atoms quickly repel each picking up  $h\Delta/2$  in kinetic energy for the homonuclear case.  $\Delta$  is the detuning of the catalysis laser above the  $5^2S_{1/2}$  to  $5^2P_{3/2}$  atomic resonance for  $^{87}\text{Rb}$ . If the kinetic energy imparted to the atoms is greater than the trap depth loss will result. This figure is patterned after that found in [16].

Fig. 3.7 shows the experimental setup used to measure the trap depth

of a MOT. The MOT setup is described earlier in section 3.1. A Coherent Titanium:Sapphire Ring laser (899-01) pumped by a Verdi V10 Coherent laser was used as the catalysis laser. The linewidth and frequency jitter of the catalysis laser was approximately 1 MHz. The frequency of the catalysis laser was set by a dc input voltage, from a frequency generator, fed to the control box. This voltage was stepped through discretely to increment the catalysis laser frequency. A small portion of the catalysis laser light was sent to a wavemeter (Bristol 621). The rest of the light was sent through an AOM (IntraAction Corp. ADM-602AF3) and the first order used. The AOM was used to turn the catalysis laser on and off at a duty cycle given by a frequency generator (Standford Research Systems DS345) sent to the AOM driver (IntraAction Corp. DE-603H6). The first order of the AOM was coupled into a single mode polarization preserving fiber and transferred to the MOT setup. The catalysis light was focused to  $\approx 1$  mm, with an intensity of  $\approx 2$  W/cm<sup>2</sup>, and overlapped with the trapped atoms in the MOT. A photodiode was used to monitor the fluorescence of the MOT in steady state without the catalysis light and also in the presence of the catalysis light with a certain duty cycle. A LabVIEW program was used to control the frequency generators responsible for stepping through different catalysis laser frequencies and for turning on and off the catalysis light being sent to the MOT. The LabVIEW program was used to capture fluorescence data from an oscilloscope (Tektronix TDS3014) as described later in this section, as well as to record the catalysis light frequency from the wavemeter.

Part of the catalysis light (not shown in Fig. 3.7) was sent to a Rb cell (Triad Technology Inc. TT-Rb-75-V-P). This was so that the catalysis laser could be scanned over the Rb absorption lines to see how the laser was behaving and to position the frequency at an appropriate starting place for the catalysis laser experiments. As mentioned, the catalysis laser light was focused onto the trapped atoms to be roughly the same size as the cloud of atoms. For initial alignment of the catalysis laser onto the trapped atoms in the MOT the catalysis laser was tuned to the MOT pump atomic resonance. During this alignment process the intensity was attenuated by neutral density filters so that the atoms could still be trapped with the catalysis laser on. In the presence of resonant catalysis light the fluorescence was lowered. The mirrors sending the catalysis laser light to the MOT were adjusted to minimize the fluorescence of the MOT so that the catalysis beam had maximal overlap with the trapped atoms.

The presence of the catalysis laser affects the loading dynamics in a MOT

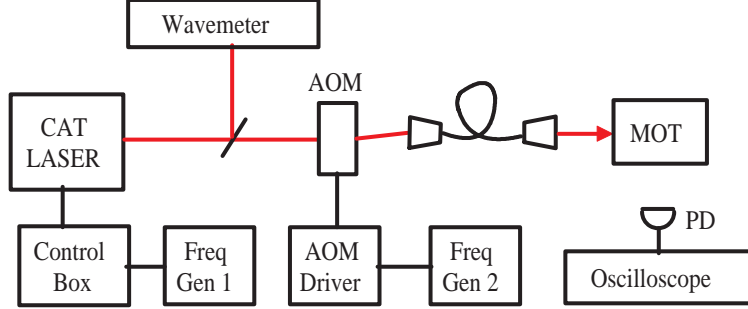


Figure 3.7: The experimental setup used to measure the trap depth of a MOT using a catalysis laser (CAT laser). The catalysis laser frequency is measured with a wavemeter. The frequency of the CAT laser is controlled by external control of the laser control box with a frequency generator. The catalysis light was sent through an acousto-optical modulator (AOM) and the first order used for the experiment. The AOM driver had a TTL input so that a function generator could be used to turn the catalysis light on and off at a given duty cycle. The catalysis light was fibered over to the MOT and aligned onto the MOT atom cloud. The fluorescence of the MOT in steady state with no catalysis light and with catalysis light on at a certain duty cycle was recorded with a photodiode and an oscilloscope. A Labview code was used to control the function generator and read from the wavemeter and oscilloscope by GPIB.

so that Eq. 1.5 becomes [16]

$$\frac{dN}{dt} = R - \Gamma N - (\beta + d \cdot \beta_{cl}) \int n^2(\vec{r}, t) d^3\vec{r} \quad (3.5)$$

where  $\beta_{cl}$  is the contribution to the two body intra-trap loss constant due to the presence of the catalysis laser and  $\beta$  is the contribution from all other two body intra-trap losses not mediated by the catalysis laser. We consider the case where the catalysis laser is modulated on and off with duty factor,  $d$ , where duty factor is the percentage of on time.

A measure of  $\beta_{cl}$  was determined, which involved the steady-state number of the trapped atoms with and without the catalysis laser present. The steady state number for the trap when the catalysis light is present with duty factor,  $d$ , using Eq. 1.9 is

$$N_{ss} = \frac{R}{\Gamma + (\beta + d\beta_{cl})n_{ss}} \quad (3.6)$$

where  $n_{\text{ss}}$  is the average steady state density of trapped atoms. Taking the ratio of  $N_{\text{ss}}$  with the steady state number,  $N_{\text{ss}}^0$ , when the catalysis laser is not present (i.e.  $d = 0$ ) gives

$$\frac{N_{\text{ss}}^0}{N_{\text{ss}}} = 1 + \frac{\beta_{\text{cl}} n_{\text{ss}} d}{\Gamma + \beta n_{\text{ss}}}. \quad (3.7)$$

Experimentally the ratio of  $\frac{N_{\text{ss}}^0}{N_{\text{ss}}}$  was determined from  $\frac{V_{\text{ss}}^0}{V_{\text{ss}}}$  as per Eq. 3.1. Here  $V_{\text{ss}}^0$  is the steady state fluorescence voltage from the trapped atoms when the catalysis laser is off.  $V_{\text{ss}}$  is the steady state voltage when the catalysis laser is on with duty factor,  $d$ . Rearranging Eq. 3.7 we define the parameter  $J$  as

$$J = \frac{N_{\text{ss}}^0}{N_{\text{ss}}} - 1 = \left( \frac{\beta_{\text{cl}} n_{\text{ss}}}{\Gamma + \beta n_{\text{ss}}} \right) d. \quad (3.8)$$

As long as  $d$  is not too large so as to change the steady state density  $n_{\text{ss}}$ , the relationship between  $J$  and  $d$  will be linear. Fig. 3.8 shows  $J$  as a function of  $d$  for different catalysis laser detunings. Fig. 3.9 shows the portion over

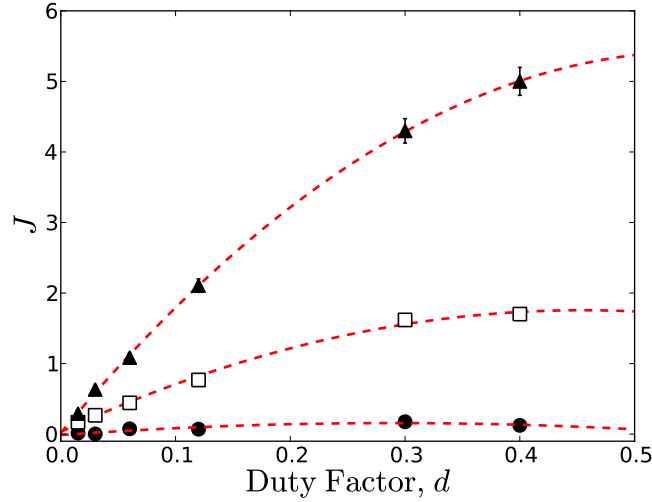


Figure 3.8:  $J = \frac{N_{\text{ss}}^0}{N_{\text{ss}}} - 1$  vs the catalysis laser duty factor  $d$ . For small duty factors the steady state density of the MOT,  $n_{\text{ss}}$  is unaffected and  $J$  vs  $d$  is linear. As  $d$  increases,  $n_{\text{ss}}$  becomes dependent on  $d$  and the curve becomes non linear. Each of the curves is for a different catalysis laser detuning.

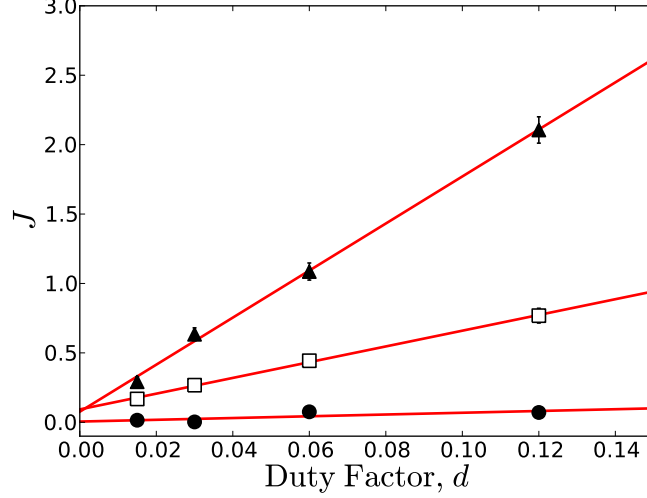


Figure 3.9:  $J$  vs  $d$  taken from Fig. 3.8 in the linear region. The slope as given by Eq. 3.8 is proportional to the loss rate constant  $\beta_{\text{cl}}$  for the repulsive loss mechanism induced by the catalysis laser. Each of the curves is for a different catalysis laser detuning.

which  $J$  versus  $d$  is linear. The slope of the linear portion of  $J$  vs  $d$  for a given catalysis laser detuning is proportional to the  $\beta_{\text{cl}}$  value for that detuning. Plotting this slope as a function of catalysis laser detuning provides a measure of  $\beta_{\text{cl}}$  as a function of detuning.

Fig. 3.10 shows a plot of our measure of  $\beta_{\text{cl}}$  versus detuning,  $\Delta$  for a MOT whose average trap depth was determined to be  $U = 0.64(0.12)K$ . To understand the qualitative behaviour of  $\beta_{\text{cl}}$  with changing  $\Delta$ , we follow the argument made in Ref. [16]. It is argued in that work that  $\beta_{\text{cl}} \propto \sigma P(h\Delta/2)$ , where  $\sigma$  is the photoassociative cross section and  $P(h\Delta/2)$  is the probability of escape of a trapped atom with kinetic energy  $h\Delta/2$ . The cross section can be written as  $\sigma = \pi r^2 f$  where  $r$  corresponds to the internuclear separation at which the catalysis laser transition occurs for a given detuning  $\Delta$ . The excitation probability,  $f$ , is inversely proportional to  $\frac{dV}{dr}$ . This is because the interaction time of the atom pair with resonant light at a given internuclear separation decreases as  $\frac{dV}{dr}$  increases. For a potential of  $V(r) = -\frac{C_3}{r^3}$  and for  $V(r) = h\Delta$  this gives  $\sigma \propto \Delta^{-2}$  and  $\beta_{\text{cl}} \propto \Delta^{-2}P(h\Delta/2)$ . The MOT

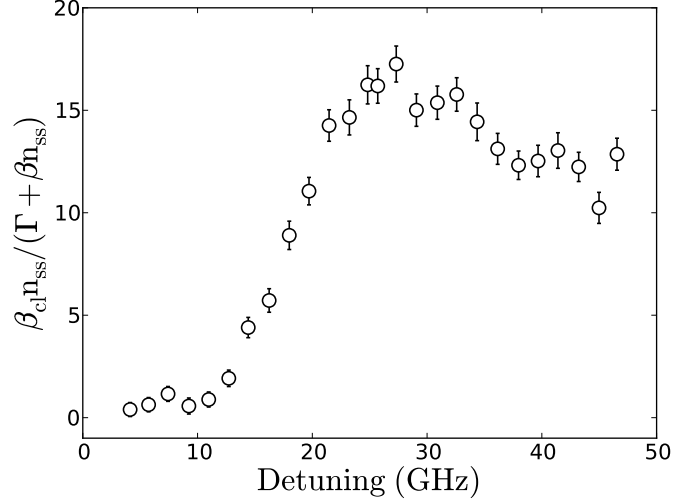


Figure 3.10: The slope of the  $J$  vs  $d$  curve (as shown in Fig. 3.9) is plotted as a function of catalysis laser detuning. The  $J$  vs  $d$  curve is proportional to the loss rate constant  $\beta_{cl}$  associated with the repulsive loss mechanism induced by the catalysis laser. The detuning,  $\Delta$ , at which  $\beta_{cl}$  is maximal corresponds to  $h\Delta/2 = U$  where  $U$  is the depth of the trap. In this manner the trap depth can be measured for a MOT. The data shown is for a  $^{87}\text{Rb}$  MOT with a pump detuning of -5 MHz and a pump intensity of  $2.7 \text{ mW cm}^{-2}$ .

trap depth is anisotropic and was found to be approximately double along the axial direction [53]. This means that  $P(h\Delta/2)$  will not be a sharp step function but will gradually increase as  $h\Delta/2$  increases from the minimum trap depth to the maximum trap depth. A gradual increase in  $P(h\Delta/2)$  predicts a gradual increase in  $\beta_{cl}$ . Because of the additional  $1/\Delta^2$  dependence of  $\beta_{cl}$ , a peak in  $\beta_{cl}$  occurs around  $h\Delta/2 = U_{\text{avg}}$ . A decrease in  $\beta_{cl}$  is seen for further increases in detunings. The decrease of  $\beta_{cl}$  with detuning,  $\Delta$ , shown in Fig. 3.10, seems to be slower than a  $1/\Delta^2$  dependence. A possible reason is because past the peak in  $\beta_{cl}$ ,  $P(h\Delta/2)$  continues to increase until  $h\Delta/2$  is the maximal trap depth. In summary, the peak of our measure of  $\beta_{cl}$  versus detuning is used to determine the average MOT trap depth. The uncertainty in the detuning at which  $\beta_{cl}$  is maximized was used to assign an uncertainty for the trap depth measurement. We note that that Hoffmann

et al. [16] plot the probability of a trapped atom escaping as a function of  $\Delta$  to determine trap depth. They interpret the detuning,  $\Delta$ , at which this probability starts to increase past approximately 30 % to correspond to the trap depth. For the trap depth measurement example given in [16], our interpretation of choosing the detuning at which  $\beta_{\text{cl}}$  is maximized predicts a trap depth about 35 % higher than their prediction for their data. Our measurement technique of MOT trap depth seems to be more correct based on the data taken in the next chapter (shown in table 3.2).

Fig. 3.11 shows the measure of  $\beta_{\text{cl}}$  plotted versus detuning,  $\Delta$ , for three different MOT trap depth conditions. As trap depth increases, the width of the curve increases, although the width relative to the trap depth stays approximately the same. This is due to the trap depth anisotropy discussed in the above paragraph. This increase in width causes the absolute error in the trap depth measurement using the catalysis method to increase with increasing trap depth. The measure of  $\beta_{\text{cl}}$  also decreases with increasing trap depth because of the decreasing probability of excitation for increasing catalysis detunings,  $\Delta$ .

### 3.4 Comparison of measurement with theory

Measuring  $\Gamma$  versus  $n_{\text{Ar}}$  provides a method of determining  $\langle\sigma v_{\text{Ar}}\rangle_{^{87}\text{Rb},^{40}\text{Ar}}$ . The theoretical predictions of  $\langle\sigma v_{\text{Ar}}\rangle_{^{87}\text{Rb},^{40}\text{Ar}}$  versus trap depth  $U$  can now be compared with experimentally measured values. Fig. 3.12 shows that the experimental results follow the predicted dependence (this is the same figure shown in Fig. 2.4). The error bars for the velocity averaged collisional loss cross section,  $\langle\sigma v_{\text{Ar}}\rangle_{^{87}\text{Rb},^{40}\text{Ar}}$ , come from linear fits of the loss rate constant,  $\Gamma$ , versus the density of argon. The error bars on a  $\Gamma$  measurement for a magnetic trap or a magneto-optical trap come from fitting a decay or loading curve, respectively, as described in section 3.2.3.

#### 3.4.1 Magnetic trap data

The data in Fig. 3.12 below 10 mK was taken previously by members of our lab with a magnetic trap and is reported in [14]. For these data, either the  $|F = 1, m_F = -1\rangle$  or the  $|F = 2, m_F = 2\rangle$  states of the  $5^2S_{1/2}$  ground state for  $^{87}\text{Rb}$  was used for magnetic trapping. Only the second lowest trap depth recorded used the  $|F = 2, m_F = 2\rangle$  state. The  $|F = 1, m_F = -1\rangle$  was used preferentially because it is easier to isolate experimentally.  $^{40}\text{Ar}$  has a nuclear spin  $I = 0$  so hyperfine changing collisions will not occur. The only

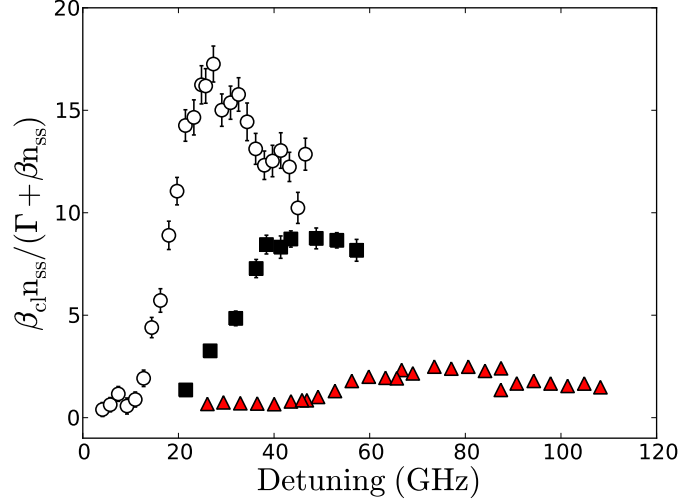


Figure 3.11: A plot of our measure of  $\beta_{cl}$  versus detuning,  $\Delta$ , for three different MOT trap depth conditions. The relative height of the curves decreases as trap depth increases because the probability of excitation by the catalysis laser decreases as detuning increases. The curves widen with increasing trap depth due to the trap depth anisotropy being approximately double along the axial direction compared to the radial direction. The width of each curve relative to the detuning at which the peak occurs is approximately the same.

expected difference between the two states is that for a given magnetic field gradient the trap depth will be double for the  $|F = 2, m_F = 2\rangle$  state.

As explained in section 1.2.2, the trap depth assigned for the magnetic trap data was an average of the trap depth along the axial and radial directions. The error bars assigned to the magnetic trap depth span the two values used in the average. The magnetic trap depth along a given direction was calculated, as discussed in section 1.2.2, by diagonalizing the hyperfine and magnetic field contribution for the intermediate B-field case. The magnetic field used was from Eq. 1.3 and Eq. 1.4, which assumes the field magnitude increases linearly with distance away from the center of the trap. A more precise expression for the B-field for a circular coil can be found in Ref. [24]. Using the linear approximation predicts a magnetic field magnitude that is 4% higher than the more accurate expression, at the edge of the

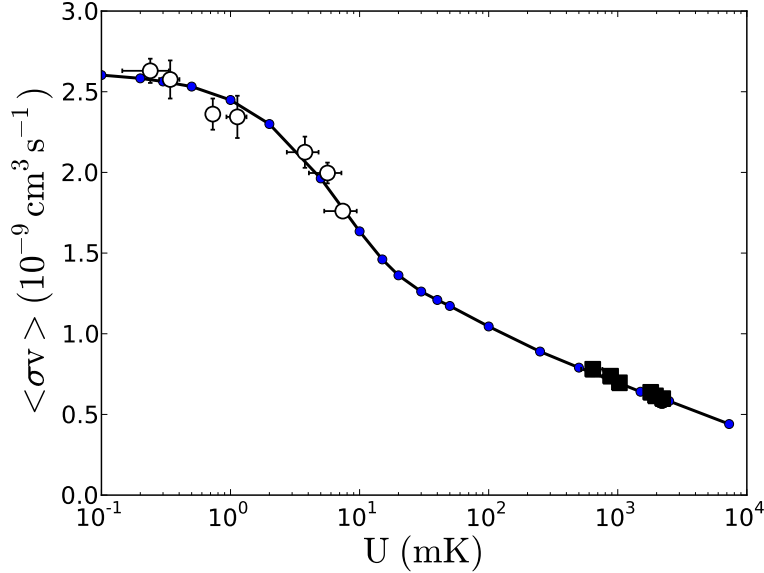


Figure 3.12: The velocity averaged collisional loss cross section for  $^{87}\text{Rb}$  as the trapped species and  $^{40}\text{Ar}$  as the background species plotted versus trap depth. The plot shows a decrease in the loss cross section with increasing trap depth. As trap depth increases, the kinetic energy required to leave the trap grows and the probability of a collision with a background gas particle imparting sufficient energy to leave the trap decreases. The curve is generated by numerically calculating  $\langle \sigma v_{\text{Ar}} \rangle_{^{87}\text{Rb}, ^{40}\text{Ar}}$  at discrete trap depths. The points superimposed on the curve are experimental data.

cell at 0.5 cm from the B-field zero. This was not accounted for in the trap depth error bars.

### 3.4.2 Magneto-optical trap data

The catalysis laser provides a means of determining the trap depth of a MOT. A zoomed in portion of the curve for the data taken with a magneto-optical trap is given in Fig. 3.13. The error bars on the trap depth are determined according to the width of the curve, as discussed in section 3.3. The error bars for the measurements of  $\langle \sigma v_{\text{Ar}} \rangle_{^{87}\text{Rb}, ^{40}\text{Ar}}$  are larger for smaller trap depths. This is because for a lower trap depth MOT there are less atoms

trapped and the signal to noise ratio for the fluorescence voltage decreases, which increases the error when determining  $\Gamma$  from loading curves. The data

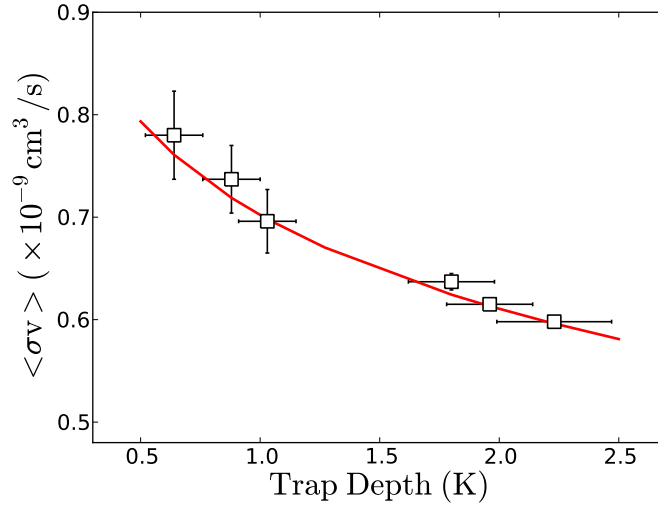


Figure 3.13: The velocity averaged collisional loss cross section plotted versus trap depth for the data taken with a magneto-optical trap. The trap depth of the trap was changed by varying the pump detuning and intensity. The data presented here is similarly presented in tables 3.1 and 3.2.

in Figs. 3.12 and 3.13 are also presented in tables 3.1 and 3.2.

### 3.4.3 Discussion

It should be noted that measurements of  $\langle \sigma v_{\text{Ar}} \rangle_{87\text{Rb}, 40\text{Ar}}$  and  $U$  did not necessarily fall on the predicted curve before a corrective factor was applied to the  $\langle \sigma v_{\text{Ar}} \rangle_{87\text{Rb}, 40\text{Ar}}$  measurements. This corrective factor corrects inaccuracy in determining  $n_{\text{Ar}}$ . This inaccuracy is due to calibration uncertainty and drift of the residual gas analyzer. In addition, as discussed in section 3.1, there are possible differences in argon density at the RGA compared to the location of the trapped atoms. To account for  $n_{\text{Ar}}$  measurement inaccuracy,  $\langle \sigma v_{\text{Ar}} \rangle_{87\text{Rb}, 40\text{Ar}}$  for a magnetic trap was measured along with the MOT measurements. The loss rate constant,  $\Gamma_{\text{MT}}$ , for a magnetic trap, with trap depth 3.14(0.84) mK, was measured at each  $n_{\text{Ar}}$  where  $\Gamma_{\text{MOT}}$  for a particular MOT setting was also measured. The trap depth of the magnetic

trap was calculated and the theoretical value of  $\langle\sigma v_{\text{Ar}}\rangle_{^{87}\text{Rb},^{40}\text{Ar}}$  for that trap depth was calculated. The ratio of the measured and calculated value of  $\langle\sigma v_{\text{Ar}}\rangle_{^{87}\text{Rb},^{40}\text{Ar}}$  for the magnetic trap provided a correction factor for all the  $\langle\sigma v_{\text{Ar}}\rangle_{^{87}\text{Rb},^{40}\text{Ar}}$  values taken for the MOT settings. This correction factor was less than 10 %, which is within the expected inaccuracy of the RGA. For the magnetic trap data taken by previous members of the labs, shown in Fig. 3.12, the trap depths were calculated and the data was scaled down to the theoretically predicted curve. In summary, the experimental data shown in Fig. 3.12 taken with both the magnetic trap and MOT were both scaled to lie on the theoretical curve. The magnetic trap data and the MOT data shown in that figure were taken at different times. For the MOT data, data was also taken for one trap depth with a magnetic trap to provide the scaling factor to apply to the MOT data.

### 3.5 Proposal for a trap depth measurement technique

This chapter has focused on confirming that the shape of the calculated  $\langle\sigma v_{\text{Ar}}\rangle_{^{87}\text{Rb},^{40}\text{Ar}}$  vs  $U$  curve agrees with measurement. It is proposed that this dependence can be used to determine the depth of a trap by measuring the velocity averaged collisional loss cross section and determining based on calculation what trap depth this corresponds to. The loss rate constant,  $\Gamma$ , can be measured for a trap as a function of  $n_i$  where  $n_i$  is the density of background species of choice  $i$ . The slope of  $\Gamma$  versus  $n_i$  gives  $\langle\sigma v_i\rangle_{X,i}$ . The value of  $\langle\sigma v_i\rangle_{X,i}$  can be calculated for a sufficient number of trap depths in the region where the depth of the trap is estimated to be and can be numerically fit to give a dependence of  $\langle\sigma v_i\rangle_{X,i}$  on  $U$ . This dependence of  $\langle\sigma v_i\rangle_{X,i}$  on  $U$  can then be inverted to give  $U$  as a function of  $\langle\sigma v_i\rangle_{X,i}$ . The measured  $\langle\sigma v_i\rangle_{X,i}$  from the slope of  $\Gamma$  versus  $n_i$  can be used to determine trap depth. The accuracy of this trap depth determination would be limited by the accuracy to which  $n_i$  is known. As described above, inaccuracies in density measurement can be corrected for when measuring  $\langle\sigma v_i\rangle_{X,i}$  for a trap whose depth is unknown if  $\langle\sigma v_i\rangle_{X,i}$  is also measured simultaneously for a known trap depth.

Table 3.2 shows trap depths measured using the catalysis technique for various pump detunings and intensities. The trap depths determined from the numerically calculated  $\langle\sigma v_{\text{Ar}}\rangle_{^{87}\text{Rb},^{40}\text{Ar}}$  vs  $U$  curve are also included. Table 3.1 and table 3.2 together contain the same information presented in Fig. 3.13. The trap depth measurement data in table 3.2 confirms that the

peak of  $\beta_{cl}$  as a function of catalysis laser detuning corresponds to the average trap depth, as discussed in section 3.3. One may wonder how the MOT trap depth depends on intensity and detuning. The values of trap depth for various detunings and intensities, given in Table 3.2, follow the qualitative behaviour that was numerically simulated in [47]. In those simulations trap depth increases approximately linearly with detuning until trap depth starts to decrease. The trap depth initially grows rapidly with intensity, but as intensity increases, the increase in trap depth slows down as saturation occurs.

A complication of the trap depth measurement technique using background collisions is that the  $\langle\sigma v_i\rangle_{X,i}$  value changes depending on the state of the trapped atom  $X$ . For both Rb and Ar in their ground state, Mitroy and Zhang [44] give  $C_6 = 336.4$  in a.u. For Rb in its  $np$  excited state and Ar in its ground state the long range potential is given as  $V(r) = -\frac{C_6}{r^6}$ . In this case  $C_6 = 924.1$  for the  $\Sigma$  molecular state, and for the  $\Pi$  molecular state it is  $C_6 = 545.1$ , both in atomic units. This gives a total velocity averaged collision cross section,  $\langle\sigma v_{Ar}\rangle_{s7Rb,40Ar}$ , in the three cases of  $2.8 \times 10^{-9}$ ,  $4.2 \times 10^{-9}$ ,  $3.4 \times 10^{-9} \text{ cm}^3 \text{ s}^{-1}$ , respectively. For  $^{40}\text{Ar}$  as the background choice an estimate of excited state fraction in our MOT at a maximum of 15% did not cause significant error in the agreement of the measured  $\langle\sigma v_i\rangle_{X,i}$  with the  $\langle\sigma v_i\rangle_{X,i}$  calculated for rubidium in its ground state. For example, for a MOT setting with  $-12$  MHz pump detuning and  $34.5 \text{ mW cm}^{-2}$  pump intensity, the measured value of  $\langle\sigma v_{Ar}\rangle_{s7Rb,40Ar}$  given in table 3.1 is  $0.598 \times 10^{-9} \text{ cm}^3 \text{ s}^{-1}$  and the calculated value shown in Fig. 3.13 is  $0.594 \times 10^{-9} \text{ cm}^3 \text{ s}^{-1}$ .

As mentioned in section 3.4.3, it was necessary to correct the measurements of  $\langle\sigma v_{Ar}\rangle_{s7Rb,40Ar}$  to account for pressure measurement inaccuracies in the density of  $^{40}\text{Ar}$ . Present pressure gauges which can measure in the  $\approx 10^{-6} \text{ Pa}$  ( $10^{-8} \text{ Torr}$ ) range, as will be discussed in the next chapter, are subject to calibration drift. Calibration is difficult and expensive and depends on gas type. It is proposed by our lab (Dr. James Booth and Dr. Kirk Madison), that the atoms themselves could serve to provide accurate and stable measurements of the density of argon,  $n_{Ar}$ , as well as possibly of other desired background gases. The idea is based on the relationship between the loss rate constant,  $\Gamma$ , due to background collisions, the density of background gas, and knowledge of the velocity averaged collisional loss cross section. The remaining chapters of this thesis focus on the proposal of using trapped atoms as a pressure sensor. The next chapter introduces existing gauges and standards, and explains more fully the concept of the ‘trapped atom pressure sensor’. The chapters afterwards describe the experimental

Table 3.1: Measurements of the velocity averaged collisional loss cross section,  $\langle\sigma v_{\text{Ar}}\rangle_{87\text{Rb},40\text{Ar}}$ , for various MOT pump intensities and detunings. The velocity averaged collisional loss cross section is the slope of the linear fit to measurements of the loss rate constant  $\Gamma$  of a  $^{87}\text{Rb}$  MOT versus the density of  $^{40}\text{Ar}$  in the background gas. The values of the velocity averaged cross section and errors quoted are from the linear fit results.

MOT detuning (MHz)	Intensity ( $\text{mW cm}^{-2}$ )	$\langle\sigma v_{\text{Ar}}\rangle_{87\text{Rb},40\text{Ar}} (\times 10^{-9} \text{cm}^3 \text{s}^{-1})$
-5	2.7	0.780 (0.043)
-8	2.7	0.737 (0.033)
-10	2.7	0.696 (0.031)
-12	6.9	0.637 (0.008)
-12	9.6	0.615 (0.006)
-12	34.5	0.598 (0.003)

Table 3.2: 3D MOT trap depths for various pump detunings and intensities. The trap depths,  $U_{\text{cat}}$ , were determined using the catalysis method described in section 3.3. As a comparison the trap depths were also obtained by fitting the numerically calculated  $\langle\sigma v_{\text{Ar}}\rangle_{87\text{Rb},40\text{Ar}}$  vs  $U$  and then determining trap depth from measured values of  $\langle\sigma v_{\text{Ar}}\rangle_{87\text{Rb},40\text{Ar}}$ . Trap depths determined numerically are denoted  $U_{\langle\sigma v\rangle}$ .

Detuning (MHz)	Intensity ( $\text{mW cm}^{-2}$ )	$U_{\langle\sigma v\rangle}$ (K)	$U_{\text{cat}}$ (K)
-5	2.7	0.55 (0.15)	0.64 (0.12)
-8	2.7	0.77 (0.17)	0.88 (0.12)
-10	2.7	1.05 (0.22)	1.03 (0.12)
-12	6.9	1.64 (0.10)	1.80 (0.18)
-12	9.6	1.93 (0.07)	1.99 (0.18)
-12	34.5	2.20 (0.05)	2.23 (0.24)

*Chapter 3. Experimental verification of the dependence of the loss cross section on trap depth*

---

progress made to date on the trapped atom pressure sensor.

## Chapter 4

# Proposal for a cold atom based pressure sensor

The cold atom based sensor that is proposed here would measure the local density of a background gas where the trapped atoms are situated. For sufficiently low pressures and high temperatures, the pressure,  $P$ , of a gas relates to its density by the ideal gas law. The ideal gas law is  $PV = Nk_B T = nRT$ , where  $N$  is the total number of atoms in volume  $V$ ,  $k_B$  is Boltzmann's constant,  $T$  is the temperature,  $n$  is the number of moles, and  $R$  is the Rydberg constant. The official SI unit of pressure is the Pascal (Pa). In North America (particularly in the US) a commonly used unit is Torr where  $1 \text{ Torr} = 133.3 \text{ Pa}$ . Ranges of vacuum are defined as low/rough vacuum ( $10^5$  to  $10^2$  Pa), medium/fine vacuum ( $10^2$  Pa to  $10^{-1}$  Pa), high vacuum (HV)( $10^{-1}$  to  $10^{-6}$  Pa), ultra-high vacuum (UHV)( $10^{-6}$  to  $10^{-10}$  Pa) and extremely high vacuum (XHV)(  $10^{-10}$  Pa and below) [54].

There are a variety of pressure measurement devices (pressure gauges) on the market, most of which have to be calibrated by a primary or a transfer standard. A primary standard is a 'measurement standard established using a primary reference measurement procedure, or created as an artifact, chosen by convention'. A primary reference measurement procedure gives '...a measurement result without relation to a measurement standard for a quantity of the same kind'. Quantities of the same 'kind' require the same units (for example diameter and circumference are of the kind length) [55].

An example of a primary pressure standard is a mercury manometer (Fig. 4.1). The pressure difference,  $P_1 - P_2$ , between two connected columns, partially filled with mercury, is determined by the height difference  $h$  of the mercury in each column. The relation is  $P_1 - P_2 = \rho gh$  where  $\rho$  is the density of mercury. By pumping down on one side so that  $P_2 \ll P_1$  we have  $P_1 \approx \rho gh$ .

Primary standards are normally quite involved both in apparatus and technique so that they are not employed as gauges in a commercial way. Instead they are maintained by national laboratories who use their primary standards to calibrate commercial gauges that can then be used as transfer

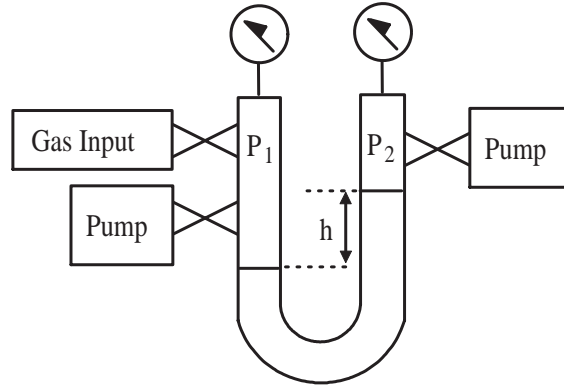


Figure 4.1: A mercury manometer is used as a primary pressure standard relating the height difference,  $h$ , of mercury in a connected tube to the pressure difference by  $P_1 - P_2 = \rho gh$ . Both the density of mercury  $\rho$  and the height difference  $h$  are traceable to primary standards in length and mass.

standards. This chapter begins with a discussion of some existing pressure gauges for the HV and UHV range and some existing primary pressure standards for the UHV vacuum range. At the end of the chapter a proposed pressure standard based on cold trapped atoms is discussed.

## 4.1 Pressure gauges

In this section we describe several pressure gauges used in the HV and UHV range. The focus is on pressure gauges that are used in our experimental apparatus for our proposed pressure standard.

### 4.1.1 Capacitance diaphragm gauge

Fig. 4.2 shows a schematic representation of a capacitance diaphragm gauge.

The capacitance diaphragm gauge consists of a sealed chamber divided into two sections by a thin inconel tensioned sheet of metal (the diaphragm). For absolute pressure measurement one side is evacuated to low pressure  $\approx P_{\text{ref}} = 0$  and sealed. A chemical getter is included to absorb any particles that outgas from the gauge material in order to maintain low pressure after this section is sealed. On the other side of the diaphragm there is an inlet to accept the gas whose pressure  $P_x$  is to be measured. The diaphragm

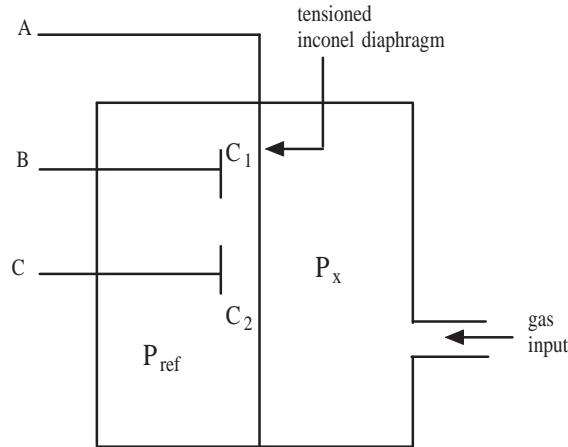


Figure 4.2: A capacitance diaphragm gauge (CDG) consists of an enclosure divided into two sections by a thin metal sheet called the diaphragm. The diaphragm is typically inonel, an alloy of predominantly nickel and chromium. For absolute pressure measurement one side of the enclosure is evacuated to a very small pressure so that  $P_{ref} \approx 0$ . The other side of the diaphragm will be deflected according to the pressure  $P_x$  to be measured. At different positions of the diaphragm the capacitance  $C_1$  and  $C_2$  formed between the diaphragm and electrodes will change. These capacitances ( $C_1$  and  $C_2$ ) are fed into an AC bridge (see Fig. 4.3) and the voltage  $V$  across the bridge related to the pressure  $P_x$ .

will deflect by an amount related to the pressure of the gas introduced. On the evacuated side several electrodes are placed so that the diaphragm forms a capacitor with each electrode. These two capacitance signals,  $C_1$  and  $C_2$  in Fig. 4.2, are fed into an AC bridge via connections A, B, and C. Fig. 4.3 shows an AC bridge where the voltage  $V$  across the bridge is zero if the impedance  $Z_1, Z_2, Z_3$  and  $Z_4$  satisfies  $\frac{Z_1}{Z_3} = \frac{Z_2}{Z_4}$ . For capacitors  $Z = \frac{1}{i\omega C}$  where  $\omega$  is the frequency of the AC source. As the diaphragm deflects with pressure the capacitances  $C_1$  and  $C_2$  change which changes the voltage across the bridge. The voltage across the bridge versus pressure can be characterized and the device made to output a voltage that varies linearly with pressure. The 615A from MKS instruments for the 1 Torr (133 Pa) range has a claimed accuracy of  $\pm 0.25\%$  [56]. The pressure range for the gauge is  $1 \times 10^{-5}$  to 1 Torr ( $1.33 \times 10^{-3}$  to 133 Pa). The lowest pressure

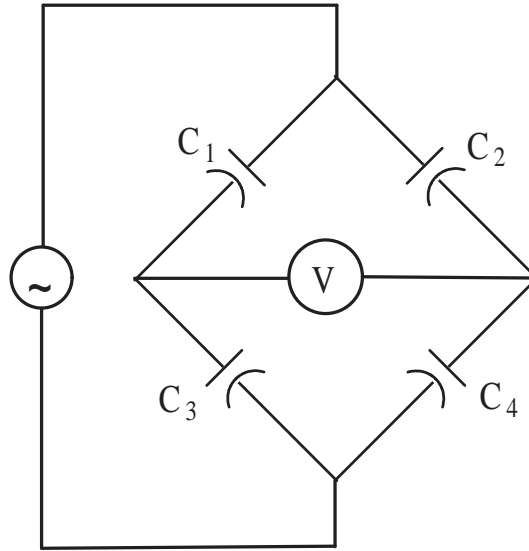


Figure 4.3: An AC bridge. The voltage,  $V$ , across the bridge is zero if the impedances satisfy  $Z_1/Z_3 = Z_2/Z_4$ .

reading of the gauge is derived from the second last digit in the pressure display on the controller front panel. The pressure reading of a capacitance diaphragm gauge can change with temperature changes so that often they are temperature controlled [57].

#### 4.1.2 Spinning rotor gauge

The spinning rotor gauge consists of a set of magnets and magnetic coils in the midst of which a magnetized steel ball is levitated (shown in Fig. 4.4). The ball (R) is levitated by two permanent magnets (M). Using drive coils (D) the ball is set to spin at a certain number of revolutions per second as detected by two pick-up coils (P). Two stabilization coils in the vertical direction (S) and four in the horizontal direction (L) are used to minimize deviations in the position of the rotor. The drive coils are then turned off and the rate of angular deceleration is measured. The relative rate of angular deceleration ( $\frac{1}{\omega} \frac{d\omega}{dt}$ ) is proportional to the pressure of the environment surrounding the ball. The ball is within the vacuum surrounded by a steel tube. The magnets and sense coils slip over the tube and are external to the vacuum environment. When the ball is spinning eddy currents induced

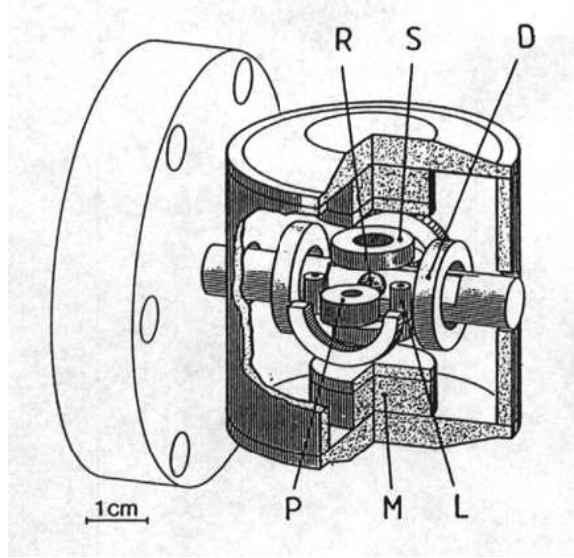


Figure 4.4: A schematic of a spinning rotary gauge. Two permanent magnets (M) are used to levitate a stainless steel ball (R). Four drive coils (D) are used to spin the ball (R) at a certain angular frequency. Vertical deviations of the ball are suppressed by two stabilization coils (S) and horizontal deviations are suppressed by four coils (L). Pickup coils (P) are used to sense the angular frequency of the ball and the rate of angular deceleration when the ball is allowed to spin without being driven in the presence of gas. From the relative rate of angular deceleration the pressure of the gas can be determined. The ball resides in a steel tube connected to the vacuum apparatus while the magnets and coil assembly slide over the tube external to the vacuum. This figure is attributed to MKS Instruments and is used with permission. This figure source is Ref. [58] .

in the ball and surrounding structures will cause a ‘residual drag’ which results in a pressure reading even for zero pressure of gas and needs to be corrected for. Fluctuations of this residual drag limit the lowest pressure that can be detected by the SRG. The SRG3 from MKS instruments which is currently in our setup can read a pressure range of  $5 \times 10^{-5}$  Pa to 100 Pa. The quoted stability is  $\leq 1\%$  per year [58]. To read accurately, the device must be calibrated since exposure to air, travel, baking and remounting of the magnetic sensing head all effect the original calibration [59, 60].

### 4.1.3 Bayard-Alpert ionization gauge

There are two main categories of ionization gauges, hot cathode and cold cathode. These categories come from whether the source of electrons to ionize gas whose pressure is to be measured comes from heating a filament (hot cathode) or from a high (kilovolt range) voltage cathode (cold cathode) [61–63]. Examples of hot cathode gauges are the Bayard-Alpert ionization gauge and an extractor gauge. Examples of cold cathode gauges are the Penning gauge, inverted magnetron gauge (Redhead) or the magnetron gauge. In our system a Bayard-Alpert ionization gauge is used which is part of the hot cathode category. In a Bayard-Alpert ionization gauge (see Fig. 4.5) current is sent through a thin tungsten filament heating the filament. The filament emits electrons which are accelerated towards an anode grid at +180V and follow trajectories around and through the grid until they hit the grid. As the electrons travel they can ionize gas they collide with forming positive ions. The grid surrounds a thin wire at 0V towards which any ions formed inside the grid will go to. This wire is called the ion collector. Ions formed outside the grid are accelerated towards the walls of the gauge (also held at 0V) and do not contribute to the ion collector current. The ratio of ion collector current to electron emission current is proportional to the pressure of the gas in which the gauge is situated and the gauge can be calibrated to give pressure readings. The calibration constant will change for different gas types because the ionization probability is different.

This gauge though popular has several unwanted features [61, 65]:

1. The calibration of the ion gauge can drift with time due to the sagging of elements in the ion gauge [66]. Any relative movement of the filament to the grid affects the electron trajectories either by changing the electron path length or by changing the amount of time the electron spends within the grid where detectable ions can be formed. Changes in electron trajectories will therefore change the ion collector current

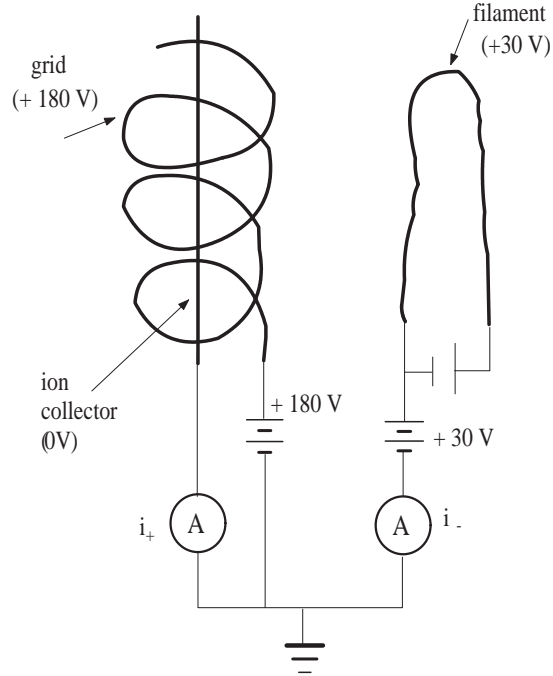


Figure 4.5: A schematic of an ion gauge. A filament (typically tungsten or yttria-coated iridium) is heated and electrons released. The electrons travel trajectories towards the positively charged grid. Ions that are formed from collisions of the electrons with the gas present will travel towards the ion collector and a current will be detected on the ion collector ( $i_+$ ). The pressure,  $P$  of the gas being measured is proportional to the ratio of the ion collector current and the electron emission current ( $i_-$ ) so that  $P \propto \frac{i_+}{i_-}$ . Figure patterned after that found in [64].

for a given pressure. The calibration can also change as the filament wears with time. ‘Poisoning’ of the filament surface by chemical reactions and by adsorption of gases can change the work function of the filament and can change the emission current [67]. The National Institute of Science and Technology (NIST) estimates the calibration factor over the period of several years to be stable within a standard uncertainty of 1.9 percent ( $k=1$ ) [68]. This result came from calibration analysis of 9 gauges, though an individual gauge calibration may vary more than this (on the order of 5 or more percent).

2. X-rays are produced when the electrons hit the grid. These x-rays can strike the ion collector and cause electrons to be liberated from the collector. This is indistinguishable from an ion current and is not related to the presence of gas being measured. This places a limit (called the ‘X-ray limit’) on the lowest pressure that can be read reliably. The ion collector is made to be a very thin wire so as to minimize this effect by intercepting as little x-rays as possible.
3. The gauge changes the local pressure in which it is in by ionizing the gas being measured and by heat-induced outgassing of the gauge components, especially the filament and the surrounding structures. Chemical reaction of the gauge components with the gas being measured can occur [67]. The electron emission current is kept low in an effort to minimize these effects.

The ion gauge installed on our system is the Granville-Phillips Series 370 Stabil-Ion Gauge with Yttria-coated Iridium filaments. The measurement range is  $2 \times 10^{-11}$  to  $5 \times 10^{-4}$  Torr ( $2.7 \times 10^{-9}$  to  $6.7 \times 10^{-2}$  Pa). The x-ray limit is  $2 \times 10^{-11}$  Torr so measurements near this limit will not be repeatable [69]. The quoted accuracy for  $N_2$  is  $\pm 4\%$  of the reading from  $1 \times 10^{-8}$  to  $1 \times 10^{-4}$  Torr ( $1.3 \times 10^{-6}$  to  $1.3 \times 10^{-2}$  Pa). The quoted repeatability is  $\pm 3\%$  of the reading from  $1 \times 10^{-8}$  to  $1 \times 10^{-4}$  Torr ( $1.3 \times 10^{-6}$  to  $1.3 \times 10^{-2}$  Pa)[64].

#### 4.1.4 Residual gas analyzer

Similar to an ion gauge, a residual gas analyzer (RGA) uses an electron beam to ionize gases present. A quadrupole RGA in addition uses an arrangement of electric fields to select which charge to mass ratio of ions will be detected. In this way by sweeping over different charge to mass ratios to be detected the RGA provides information on the composition of the gas being measured

and the relative amount of different gas species. Residual gas analyzers are most easily used for qualitative detection of the presence of various species in the vacuum system. For quantitative work they must be calibrated for the species that is to be measured. The RGA on our system is the QMG220 M2 PrismaPlus from Pfeiffer Vacuum (part number PTM06241213) which has a minimum detection limit less than  $2 \times 10^{-12}$  mbar and a mass range of 1-200 amu [70].

#### 4.1.5 Pirani gauge

In a Pirani gauge, changes in resistance of a heated wire with pressure are detected. One of these gauges ( a ‘convectron’ gauge accompanying the 370 Stabil-Ion gauge, part number 275256) is installed on our system to detect failures in the turbo and scroll pumps. The pressure range they read is in the  $1 \times 10^{-4}$  to 1000 Torr range ( $10^{-2}$  to  $10^5$  Pa range).

## 4.2 Existing pressure standards

This section outlines some of the existing pressure standards that are used to calibrate gauges in the high and ultra-high vacuum pressure range.

### 4.2.1 Static expansion method

In the static expansion method [71] the pressure in a chamber of known volume,  $V_1$ , is measured at a pressure  $P_1$ . The pressure  $P_1$  is high enough that it can be accurately measured with a gauge calibrated on a high pressure standard (such as a mercury manometer). The gas is then expanded into volume  $V_1$  and  $V_2$  so that  $P_1 V_1 = P_2 (V_1 + V_2)$  where  $P_2$  is the pressure after expansion. Provided that the volumes  $V_1$  and  $V_2$  are accurately known and  $P_1$  is accurately measured then  $P_2$  can be determined. A gauge connected to the volume  $V_1$  or  $V_2$  can be calibrated at lower pressures than the gauge that was used to measure  $P_1$ . This could also be used to extend the calibration range of the gauge that measured  $P_1$ . The static expansion method typically is used as a standard down to  $10^{-5}$  Pa, though it can be extended for inert gases down to  $10^{-7}$  Pa [72]. The lower pressure limit is mainly determined by the outgassing from the vacuum chamber.

### 4.2.2 Orifice flow method

For calibration of gauges at a pressure range of ( $10^{-1}$  to  $10^{-10}$  Pa), orifice-flow standards (also known as dynamic expansion methods) are used [54, 71, 73–75]. Ion gauges are typically calibrated by this method. The typical setup of the orifice flow method is shown in Fig. 4.6. Two chambers are separated by an orifice with gas being fed into chamber 1 and pumped out at chamber 2. The flow of gas through the orifice can be characterized by the ‘throughput’. Throughput,  $Q$ , also sometimes called flow or flow rate, of gas into/out of a volume  $V$  with pressure  $P$  is defined as  $Q = \frac{d(PV)}{dt}$ . For the ideal gas law  $PV = nRT$  and

$$Q = \frac{d(PV)}{dt} = RT \frac{dn}{dt} \quad (4.1)$$

so that throughput is proportional to the rate of molar increase/decrease in the volume  $V$ . Throughput has units of  $\frac{\text{Pa}\cdot\text{m}^3}{\text{s}}$ . The molar rate of change  $\frac{dn}{dt}$  is also commonly called flow or flow rate and has units of mol/s. Through the orifice there will be a throughput of

$$Q = C(P_1 - P_2) \quad (4.2)$$

where  $P_1$  and  $P_2$  are the pressures in chamber 1 and 2 respectively. The conductance  $C$  depends on the dimensions of the orifice, and the gas type and temperature [61, 65]. The conductance is independent of pressure for sufficiently low pressures (i.e  $< 100$  Pa) [76]. Chamber 1 in Fig. 4.6 has a net throughput of zero and its pressure,  $P_1$ , is in steady state.

In the schematic of an orifice flow standard shown in Fig. 4.6 two gauges are installed at the upper chamber. One of the gauges ( $G_a$ ) is calibrated on another standard in a higher pressure range, and another gauge ( $G_b$ ) is to be calibrated at a lower pressure range than  $G_a$ . Dividing Eq. 4.2 above by  $P_1$  we have

$$\frac{Q}{P_1} = C(1 - r) \quad (4.3)$$

where  $r = P_2/P_1$ . In the molecular flow regime (where the gas atoms or molecules hit the walls before hitting each other) the ratio  $r$  is a constant at different flow rates,  $Q$ . The ratio  $r$  can be determined by generating a large flow so that the pressure,  $P_1$ , in chamber 1 is high enough that it can be measured with gauge  $G_a$ . Gauge  $G_a$  is typically a spinning rotary gauge. In addition, throughput  $Q$  is measured with a flowmeter so that the ratio  $r$  can be solved from Eq. 4.3 with a known conductance.

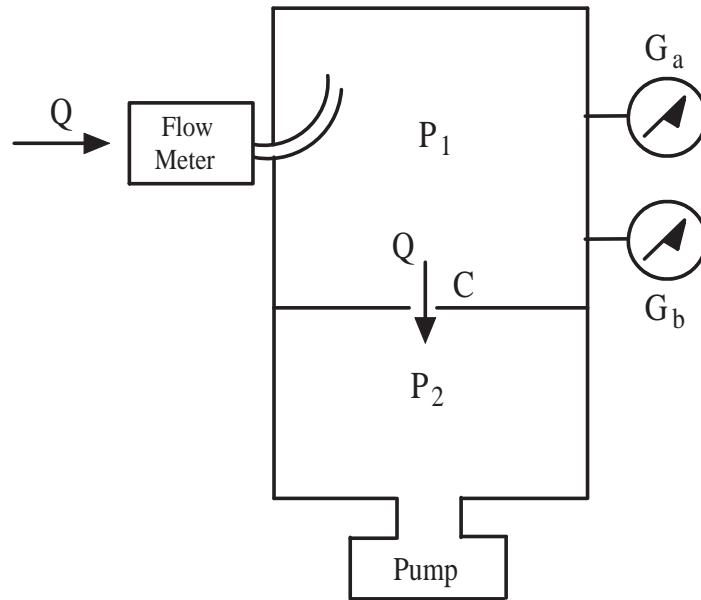


Figure 4.6: Two chambers are separated by an orifice of known conductance  $C$ . The throughput through the orifice is  $Q = C(P_1 - P_2)$ . This throughput will be the same as the throughput input to chamber 1 providing the pressure  $P_1$  in the upper chamber is in steady state and outgassing is negligible. Two gauges are connected to the upper chamber. Gauge A ( $G_A$ ) is calibrated on another higher pressure range standard and is typically a spinning rotary gauge. Gauge B ( $G_B$ ) is the gauge that is to be calibrated by the orifice flow standard.  $Q$  is measured with a flowmeter and  $C$  is either independently measured or calculated. The ratio  $r = P_1/P_2$  is determined by sending a large enough throughput through the system so that gauge A can measure  $P_1$ . The flow is then cut back so that the pressure  $P_1$  in the upper chamber is lower than the calibration range of gauge A. The ratio  $r$  is constant within the molecular flow regime so that the pressure  $P_1$  in the upper chamber can be determined from  $Q$ ,  $C$  and  $r$  and can be used to calibrate gauge B.

To calibrate the gauge  $G_b$  in Fig. 4.6, the flow can then be cut back so that the pressure  $P_1$  is below the measuring range of the calibrated gauge  $G_a$ . With measured  $Q$ ,  $r$ , and known  $C$ , the pressure  $P_1$  can be determined from Eq. 4.3.

For a constant pressure flowmeter, as shown in Fig. 4.7, the volume of a gas-filled region is changed at a constant rate,  $\frac{dV}{dt}$ , driving gas out of the volume through a leak valve [77, 78]. The pressure,  $P$ , is kept constant in the volume and is measured by a calibrated pressure gauge. With the pressure, the rate of volume change, and the temperature  $T$ , the molar flow rate  $\frac{dn}{dt}$  is given as

$$Q = P \frac{dV}{dt} = \frac{dn}{dt} RT. \quad (4.4)$$

The conductance of an orifice can be measured using a constant pressure flow meter. The orifice is used as the outlet for the flowmeter instead of a leak valve [78]. The basic idea is that for a known flow  $Q$  produced by the flowmeter, a known pressure  $P$  inside the flowmeter, and a small pressure on the output side of the orifice, the conductance  $C$  of the orifice is given as  $C = Q/P$ . The conductance can also be calculated using Monte-Carlo simulations [78].

A separated flow method can also be used to extend the range of a flowmeter [73, 76]. A known throughput  $Q$  from a flowmeter is put into a volume with two orifices with conductances  $C_1$  and  $C_2$ . The flow through the orifice of conductance  $C_1$  will be  $Q_1 = Q \frac{C_1}{C_1+C_2}$ . The flow through the orifice of conductance  $C_2$  will similarly be  $Q_2 = Q \frac{C_2}{C_1+C_2}$ . Smaller known flows enables calibration of smaller pressures  $P_1$  using Eq. 4.3.

Ar and N<sub>2</sub> gas are typically used in orifice flow standards. When asked why, NIST [79] responded that reactive gases are not favourable, nor are ‘sticky’ gases that are hard to pump, such as H<sub>2</sub>O. Also, if the gas molecule is too complex (for example a polyatomic molecule) then calculations of the conductance of the orifice become difficult.

### 4.3 A proposed density/pressure standard using trapped atoms

It is proposed that measurement of background gas collisional loss rate can be used to measure the density of a given background gas surrounding a cloud of trapped atoms. Assume for the moment that there is only one background species, for example <sup>40</sup>Ar, and that the trapped species is <sup>87</sup>Rb.

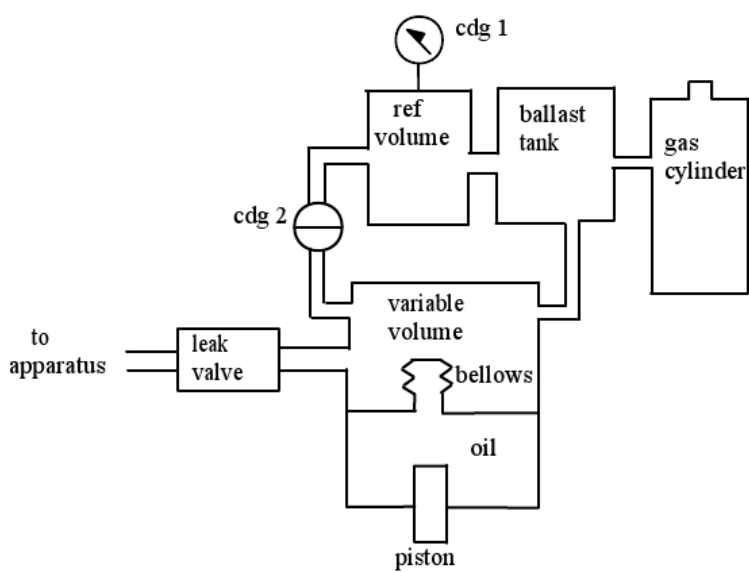


Figure 4.7: A constant pressure flowmeter used to generate a known flowrate. The volume of a chamber is changed steadily while the pressure is kept constant with respect to a reference chamber allowing a precise determination of flowrate out of the variable volume chamber.

From Eq. 2.1 the loss rate constant can be expressed as

$$\Gamma = n_{\text{Ar}} \langle \sigma v_{\text{Ar}} \rangle_{^{87}\text{Rb}, ^{40}\text{Ar}}. \quad (4.5)$$

The velocity averaged collisional loss cross section,  $\langle \sigma v_{\text{Ar}} \rangle_{^{87}\text{Rb}, ^{40}\text{Ar}}$ , was described in Chapter 2. The proposed density measurement involves measuring  $\Gamma$  for trapped  $^{87}\text{Rb}$  atoms. With known  $\Gamma$  and  $\langle \sigma v_{\text{Ar}} \rangle_{^{87}\text{Rb}, ^{40}\text{Ar}}$  for a known trap depth of the trap,  $n_{\text{Ar}}$  can be determined. This proposal is not restricted to our particular choice of trapped atom or background gas. A discussion of the advantages of using a MOT or a magnetic trap is discussed in section 4.3.2.

Trap loss due to background gas collisions and its dependence on background gas pressure is well established [27, 80–82]. The novelty of the study of trap loss due to background collisions expressed here is the proposed application of the loss rate constant due to background collisions,  $\Gamma$ , to precision measurements of background gas density. Also, as mentioned in chapter 3, the loss rate constant,  $\Gamma$ , and the velocity averaged collisional loss cross section can be applied to the measurement of trap depth of a trap.

A decay time constant of 0.01 to 100 s, corresponds to a loss rate constant,  $\Gamma$ , of 100 to  $0.01 \text{ s}^{-1}$ , which corresponds to a pressure measurement range of  $10^{-4}$  to  $10^{-8} \text{ Pa}$  ( $10^{-6}$  to  $10^{-10} \text{ Torr}$ ). It is within vacuum technology to achieve ultimate background pressures orders of magnitudes lower than this pressure range so that the assumption that  $^{40}\text{Ar}$ , for example, could be taken as the dominant species is reasonable. The expected pressure range of the atom gauge on the lower pressure side depends on the residual background pressure in our system. Our apparatus is described in the next chapter, and the background pressure is on the order of the low  $10^{-8} \text{ Pa}$  ( $10^{-10} \text{ Torr}$ ) to  $10^{-7} \text{ Pa}$  ( $10^{-9} \text{ Torr}$ ) depending on the pumps that are used. In section 1.3.1 it is estimated that the intra-trap loss rate for a MOT becomes comparable to the background collisional induced loss rate below  $10^{-6} \text{ Pa}$  ( $10^{-8} \text{ Torr}$ ). As also mentioned in section 1.3.2, the intra-trap loss rate for a magnetic trap should be negligible compared to the background loss rate even below  $10^{-6} \text{ Pa}$  ( $10^{-8} \text{ Torr}$ ). The higher pressure range measurable is around the low ( $< 2 \times 10^{-4} \text{ Pa}$  ( $2 \times 10^{-6} \text{ Torr}$ )) range because our magneto-optical trap does not form above that.

The proposed density measurement method potentially also allows density measurement of multiple species in the background (i.e. differential pressure measurement), provided that what those species are is known. Suppose the background composition is known to contain N different background

species. The loss rate  $\Gamma$  will have a contribution from each of these species

$$\Gamma = \sum_{i=1}^N n_i \langle \sigma v_i \rangle_{X,i}. \quad (4.6)$$

As discussed in previous chapters, the loss cross section depends on trap depth. Measurements of  $\Gamma$  could be taken at  $N$  different trap depths and the values of  $\langle \sigma v_i \rangle_{X,i}$  at each trap depth determined. Eq. 4.6 then would give  $N$  equations and  $N$  unknowns and the densities  $n_1 \dots n_N$  could be solved for.

It is hoped that the method of density measurement using trapped atoms could serve as a pressure standard. Currently the pressure standards for the UHV pressure range rely on measurements using gauges calibrated at higher pressures. The proposed method has the possibility of not having to use calibrated gauges. For example, for Ar or noble gases the dispersion coefficients for the interaction potential between trappable alkali metal atoms have been calculated [43–45] which allows the velocity averaged collisional loss cross section to be calculated for a known trap depth. With a known velocity averaged collisional loss cross section, an externally calibrated gauge should not be necessary. There is also the possible advantage of improved inter-laboratory agreement for pressure calibration because atomic interactions are fundamentally the same in any lab. The velocity averaged collisional loss cross section should be the same in all laboratories using the same trap depth and room temperature.

There are efforts to make trapped atom technology more portable, which would help with providing on-site calibration. Semi-conductor manufacturing processes involving thin film deposition [83], ion implantation [84] and atomic layer deposition [85, 86] use residual gas analyzers and benefit from accurate calibration of these devices. In-situ calibration techniques have been developed which rely on externally calibrated ion gauges and flow rates [87]. Having an on-site calibration of RGAs or ion gauges using trapped atoms may be a possibility. The technique proposed of using trapped atoms to perform differential pressure measurement would help with RGA calibration where more than one species is desired to be calibrated simultaneously. Trapped atoms could also potentially be applied to measurement of pressure for gases that are currently not used in existing standards.

There is still merit to the proposed method even if it is not desired or it is difficult to calculate the velocity averaged collisional loss cross section between the trapped atom species and the background gas species chosen. A gauge that is calibrated on another standard could be used to measure

the density of the desired background gas. The loss rate constant,  $\Gamma$ , for the trapped atoms could be measured for various background gas densities. As seen in subsection 3.2.3, the slope of the plot of  $\Gamma$  versus background gas density yields the velocity averaged collisional loss cross section. Once the velocity averaged collisional loss cross section is known for a given trap depth it does not change as long as the trap conditions stay the same. The trapped atoms once calibrated could serve as a transfer standard which if put in a miniaturized and commercially viable package could enable customers to calibrate their gauges on site. The trapped atoms could also be used to extend gauge calibration to lower pressures and serve as a standard at lower pressures, much in the same way that orifice flow standards rely on a gauge that is calibrated on a higher pressure standard.

#### 4.3.1 Existing proposals for total vacuum pressure measurement using trapped atoms

If the gas species whose pressure is to be measured is unknown, unfortunately the technique of using trapped atoms cannot give high accuracy pressure measurements. However, Arpornthip et al. [46] proposed that a MOT could provide rough measurements of background pressure (within a factor of two). As seen in Eq. 2.1 the loss rate due to background collisions,  $\Gamma$ , can be expressed as

$$\Gamma = \sum_i n_i \langle \sigma v_i \rangle_{X,i} \quad (4.7)$$

where  $n_i$  is the background density of species,  $i$ , and  $\langle \sigma v_i \rangle_{X,i}$  is the velocity averaged collisional loss cross section for collisions between the background species  $i$  and trapped atoms (labelled type  $X$ ). Writing Eq. 4.7 in terms of partial pressure  $P_i = n_i k_B T$  gives

$$\Gamma = \sum_i \frac{P_i}{k_B T} \langle \sigma v_i \rangle_{X,i}. \quad (4.8)$$

Arpornthip et al. calculated that  $\langle \sigma v_i \rangle_{X,i}$  varies roughly within a factor of two independent of background species choice  $i$  and can be pulled out of the summation. For Rb as the trapped species, they estimate for background gases such as  $\text{H}_2$ , He,  $\text{H}_2\text{O}$ ,  $\text{N}_2$ , Ar, and  $\text{CO}_2$ , that the quantity  $a = \frac{\langle \sigma v_i \rangle_{X,i}}{k_B T}$  has an approximate value of  $a = 1.7 \times 10^5$  to  $3.7 \times 10^5 \text{ Pa}^{-1} \text{ s}^{-1}$  ( $a = 2.3 \times 10^7$  to  $4.9 \times 10^7 \text{ Torr}^{-1} \text{ s}^{-1}$ ). This is for Rb as the trapped atom species. Assuming  $a$  is roughly the same for the different background species then

$a$  can come out of the summation. This gives a sum over partial pressures which adds to the total pressure,  $P$ , giving

$$\Gamma = aP. \quad (4.9)$$

By taking measurements of  $\Gamma$  and using the rough values given for  $a$  one can determine the background pressure in their system using a MOT. This idea is very similar to our proposed pressure measurement using trapped atoms. Their technique is different in that it is applied to lower precision pressure measurements of the total background pressure, whereas we are proposing using trapped atoms as a pressure standard for a certain known species. Similar ideas to that of Arpornthip et al. of using a MOT to measure the surrounding total vacuum pressure is also shown by Refs. [88, 89]. These ideas are motivated by being able to have a more compact and portable MOT setup without the need for an ion gauge to measure the background pressure.

### 4.3.2 Magneto-optical trap versus magnetic-trap for a pressure sensor

Each of the two atomic traps have advantages and disadvantages for use as a high accuracy ( $< 5\%$  uncertainty) sensor. The magnetic trap has the advantages of being able to trap atoms all in one state, being able to set the trap depth with an RF knife, and not having light mediated losses. The magneto-optical trap has some fraction of the atoms in the excited state, and it has light mediated losses. The magneto-optical trap has the advantage of cooling down trapped atoms that were collided with but were not lost from the trap, whereas for a magnetic trap collisions that did not lead to loss lead to heating. A magneto-optical trap also has a simpler and faster experimental sequence to determine the loss rate constant,  $\Gamma$ . The signal to noise for a single  $\Gamma$  measurement is also better for a MOT. Our aim is to explore both options for pressure measurement, possibly using a combination of magnetic trap at low pressures where light mediated losses become comparable to  $\Gamma$  for a MOT. A MOT could be used at high pressures where the signal would be small because the steady state atom number decreases as pressure goes up. For differential pressure measurements, as described above, a magnetic trap may be better because the velocity averaged cross section changes more with the trap depths accessible with a magnetic trap. However, it could also be useful for differential measurement to have access to a wide range of trap depths provided by both a magnetic trap and a MOT. In summary, both the magnetic trap and MOT have advantages for

use with pressure measurement, with the MOT being perhaps more suited for high pressure measurement and the magnetic trap for low pressure measurement. In the range of pressure overlap between the two types of traps, the pressure measurements should be shown to agree.

### 4.3.3 Estimated uncertainty

The uncertainty in the proposed pressure measurement using trapped atoms depends on the uncertainty in the measurement of the loss rate constant,  $\Gamma$ , and the calculation of the velocity averaged collisional loss cross section  $\langle\sigma v\rangle$ .  $\Gamma$  has an uncertainty of roughly 3% on a single loss rate measurement which can be reduced by multiple measurements, hopefully to below 1%.

As discussed in chapter 2, the physical parameters to input into the calculation for  $\langle\sigma v\rangle$  are the masses of the background gas species and the trapped atom species, the interaction potential  $V(r)$ , the temperature of the background gas, and the trap depth. For  $^{87}\text{Rb}$  as the trapped species, and  $^{40}\text{Ar}$  as the background gas species, the percentage change of the value of  $\langle\sigma_{\text{loss}}v_{\text{Ar}}\rangle_{^{87}\text{Rb},^{40}\text{Ar}}$  was calculated for a 10 percent, 50 percent and 100 percent increase in the  $C_6$  coefficient, well depth, background temperature, and trap depth. The original input parameter values used were a background gas temperature of 294 K, a potential with  $V(r) = \frac{C_{12}}{r^{12}} - \frac{C_6}{r^6}$  with  $C_6 = 336.4$  a.u., a  $50\text{ cm}^{-1}$  well depth used for  $C_{12}$ , and a 5 mK trap depth. The results of the calculation are shown in Table 4.1, where the values in the tables are expressed in percentages and under each parameter is the percentage change of  $\langle\sigma_{\text{loss}}v_{\text{Ar}}\rangle_{^{87}\text{Rb},^{40}\text{Ar}}$  due to 10, 50 and 100 percent increases in the parameters while the other parameters were held at the original values. Given that

Table 4.1: Percentage changes for the value of  $\langle\sigma_{\text{loss}}v_{\text{Ar}}\rangle_{^{87}\text{Rb},^{40}\text{Ar}}$  due to 10, 50 and 100% increases in the values of  $C_6$ , well depth  $\epsilon$ , temperature ( $T$ ), and trap depth ( $U$ ). While one parameter changed the other parameters were held fixed at  $T = 294\text{ K}$ ,  $C_6 = 336.4\text{ a.u.}$ ,  $\epsilon = 50\text{cm}^{-1}$ , and  $U = 5\text{ mK}$

Percentage change	$C_6$	$\epsilon$	$T$	$U$
10	3	-0.02	4	-2.3
50	13	-0.06	15	-10
100	23	0.03	26	-17

the temperature variations expected in the room should generally exceed no more than 2 K the room temperature variation should contribute negligibly to the uncertainty in  $\langle\sigma_{\text{loss}}v_{\text{Ar}}\rangle_{^{87}\text{Rb},^{40}\text{Ar}}$ , i.e  $< 0.1\%$ . Another source of error

is temperature variations at different locations in the vacuum apparatus. The temperature variation, except right near an ion gauge, is less than 5K. At an ion gauge flange the exterior of the gauge is  $\approx 50$  to  $60$  °C . The rest of the apparatus is at room temperature. As described in section 4.2.2, the ion gauges are typically calibrated by a gauge such as a spinning rotary gauge that is nearby but not at the same local temperature as the ion gauge. This means although locally at the ion gauge the temperature is higher than room temperature the gauge is calibration is performed within an environment that is at room temperature.

Changes in the well depth,  $\epsilon$  contribute negligibly. The most significant contribution to uncertainty in  $\langle\sigma_{\text{loss}}v_{\text{Ar}}\rangle_{87\text{Rb},40\text{Ar}}$  are errors in the  $C_6$  coefficient and trap depth. The  $C_6$  given is accurate to within 1% [43, 44], which contributes an error to  $\langle\sigma_{\text{loss}}v_{\text{Ar}}\rangle_{87\text{Rb},40\text{Ar}}$  of roughly 0.3%. It should be noted that there are dipole-quadrupole ( $C_8/r^8$ ) and quadrupole-quadrupole ( $C_{10}/r^{10}$ ) contributions to the interaction potential that should also be included to attain the best accuracy possible. If the trap depth can be set to within approximately 5%, then the resulting uncertainty contribution of trap depth to  $\langle\sigma_{\text{loss}}v_{\text{Ar}}\rangle_{87\text{Rb},40\text{Ar}}$  is approximately 1.5%. To get a sense of realistic trap depth errors, we refer to the measurements described in chapter 3 in Fig. 3.12 and Fig. 3.13. There the estimated trap depth error for the magnetic trap data was around 30% and the MOT trap depth error was around 15%. For the magnetic trap the trap depth error may be reduced by using an RF-knife (see section 1.2.2). An RF-knife was not used for the measurements in chapter 3. Note also that the trap depth of 5 mK chosen for these uncertainty estimates is approximately at the steepest point on the  $\langle\sigma_{\text{loss}}v_{\text{Ar}}\rangle_{87\text{Rb},40\text{Ar}}$  versus trap depth curve in Fig. 3.12. This means the contribution of trap depth uncertainty to the uncertainty of  $\langle\sigma_{\text{loss}}v_{\text{Ar}}\rangle_{87\text{Rb},40\text{Ar}}$  should be an upper bound. In summary, an estimate of  $< 5\%$  is hoped for for the uncertainty in  $n_{\text{Ar}}$  based on uncertainty in  $\langle\sigma_{\text{loss}}v_{\text{Ar}}\rangle_{87\text{Rb},40\text{Ar}}$  and  $\Gamma$ . Another possible source of error is pressure differences at the trapped atoms versus the gauge locations. This is further discussed in section 8.1.

The National Institute of Standards and Technology (NIST) performs calibration of ionization gauges at pressures of  $10^{-3}$  to  $10^{-5}$  Pa ( $10^{-5}$  to  $10^{-7}$  Torr) with an uncertainty of 0.7% or less with the uncertainty rising to 2% at  $10^{-7}$  Pa ( $10^{-9}$  Torr) [90].

## Chapter 5

# Experimental apparatus for the pressure sensor experiment

This chapter provides details on the design and construction of the experimental apparatus for taking pressure measurements using trapped atoms. A solidworks drawing of the vacuum apparatus is given in Fig. 5.1. Fig. 5.2 shows the same apparatus from a different point of view. Vacuum created in the system starts with the high-vacuum (HV) pump region of the apparatus consisting of scroll and turbo pumps. The 2D MOT section consists of a chamber with viewports for the 2D MOT light to enter. A Rb source is also attached to the 2D MOT chamber to load the 2D MOT from Rb vapour. The 2D MOT section is connected to the 3D MOT section through a series of tubes used for differential pumping. The 2D MOT provides an atomic beam of  $^{85}\text{Rb}$  or  $^{87}\text{Rb}$  atoms to the 3D MOT section. The 3D MOT section consists of a glass cell for input of laser beams and surrounding magnetic coils to create a 3D MOT and a magnetic trap. The 3D MOT cell has ultra-high vacuum (UHV) pumps attached to it to maintain low pressures (i.e. in the  $10^{-9}$  Pa ( $10^{-11}$  Torr) range). Diagnostics (pressure gauges) are also attached to the 3D MOT cell to compare pressure measurements of commercial gauges with measurements taken using trapped atoms. Below the 2D MOT section is a leak valve to input gases whose pressures are to be measured. This chapter will provide more detail on all of these different sections of the experimental apparatus. Not shown in Fig. 5.1 and Fig. 5.2 are the optics used to generate the 2D and 3D MOT light. These optics will also be discussed in this chapter. Throughout this chapter any abbreviated labelling refers to Fig. 5.1 unless otherwise noted.

Several features of our apparatus that are not common in experiments involving ultra-cold atoms are the presence of a leak valve to introduce background gas, the design of our differential pumping system, and the numerous pressure gauges installed on our apparatus. A new apparatus

was built, different from the one used for chapter 3, to implement these features. A motivation for a brand new apparatus is that the 3D MOT used in chapter 3 is vapour loaded and the implementation of a 2D MOT allows the pressure in the 3D MOT region of Rb to be low. Also, in a 2D MOT setup, the Rb source is protected from reactive gases that may be studied later. The optical setup used in chapter 3 does not generate enough power for a 2D MOT and a 3D MOT, and a new optical setup with a tapered amplifier was needed. Another reason for a new setup is physically the new apparatus takes more room than is available on the optical table occupied by the setup used in chapter 3.

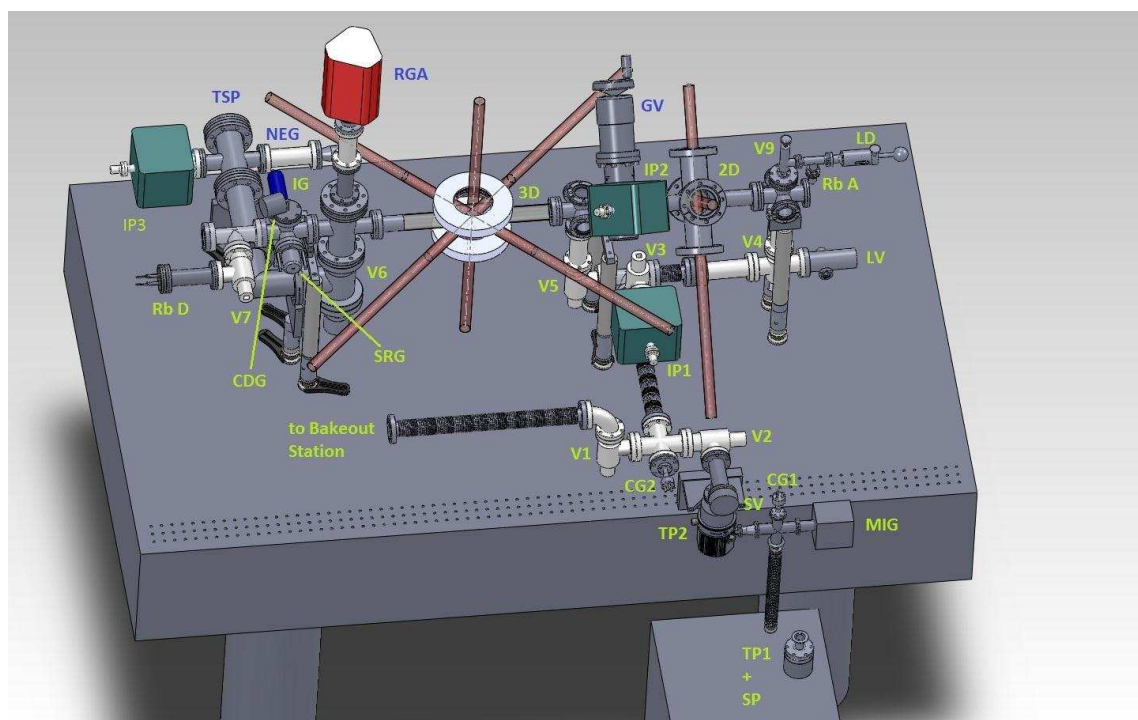


Figure 5.1: The vacuum apparatus for the pressure sensor experiment. SP: scroll pump, TP1, TP2: turbo pumps, MIG: mini ion gauge, CG1 and CG2: convection gauges, SV: solenoid valve, V1-V9 (V8 not shown): all metal valves, IP1-IP3: ion pumps, LV: leak valve, LD: linear drive mechanism, RbA: rubidium ampoule, 2D: 2D MOT chamber, GV: gate valve, 3D: 3D cell, RGA: residual gas analyzer, CDG: capacitance diaphragm gauge, SRG: spinning rotary gauge, IG: ion gauge, RbD: rubidium dispensers, TSP: titanium-sublimation pump, NEG, non-evaporable getter.

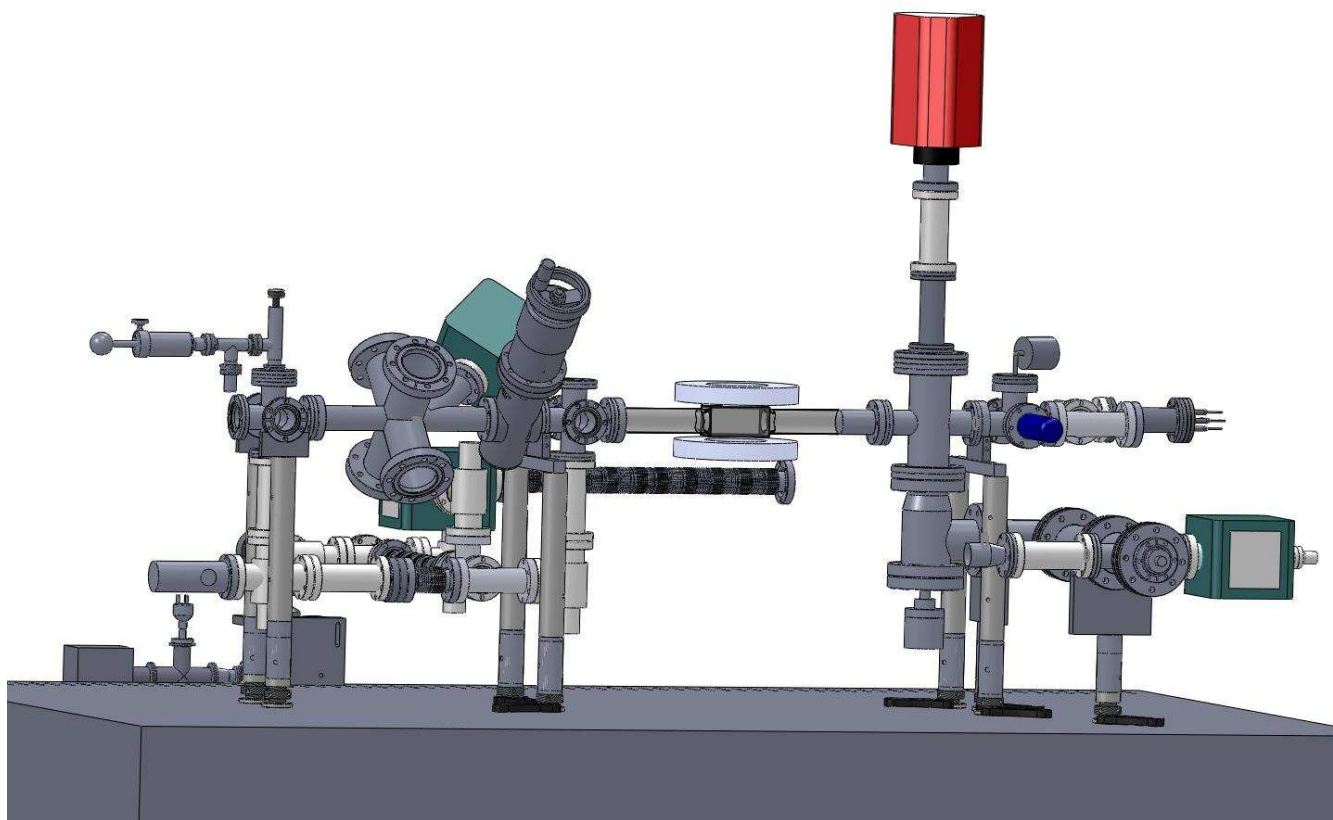


Figure 5.2: Another perspective of the vacuum apparatus for the pressure sensor experiment. The apparatus consists of different main sections. At the 2D MOT section a 2D MOT is created to form an atomic beam to load a 3D MOT. A Rb source is connected to the 2D MOT region to load the 2D MOT from Rb vapour. The 3D MOT section consists of a glass cell. UHV pumps are used to maintain ultra-high vacuum pressure in the 3D MOT cell. Pressure gauges are attached to the 3D MOT cell to provide measurements of pressure to compare to the pressure measurements taken with trapped atoms.

## 5.1 High vacuum pumps

Our experiment uses a variety of vacuum pumps to establish ultra-high vacuum (UHV) in our apparatus (pressures  $< 10^{-6}$  Pa or  $< 10^{-8}$  Torr). Starting from atmospheric pressure we pump with a scroll pump (SH-110, Agilent) labelled SP. The scroll pump has two circular mechanisms that move with respect to each other and compress gas that enters the mechanisms towards an exhaust output. The scroll pump has a specified base pressure of 7 Pa ( $5 \times 10^{-2}$  Torr) [91]. The measured base pressure with an eyesys mini-BA ion gauge from Varian connected directly to the scroll pump was 4.8 Pa ( $3.6 \times 10^{-2}$  Torr). To get lower in pressure, turbomolecular pumps (TV 70, Agilent) labelled TP1 and TP2 were attached in series and backed by the scroll pump. Turbomolecular pumps have a series of blades which are angled. When spinning, the blades impart momentum to the gas that hit the blades towards another set of blades etc. The gas makes its way to the exhaust which is pumped away by the scroll pump. The specified base pressure of the turbo pump is  $5.1 \times 10^{-7}$  Pa ( $3.8 \times 10^{-9}$  Torr).

During initial evacuation and while baking we attached to the vacuum system the ‘bakeout station’ described in sec. 3.1. This station has another scroll pump (SH-100, Agilent) and a turbo pump (TV 70, Agilent). During initial pump down and baking, the turbo and scroll pumps were the only pumps operating since the other pumps in the apparatus operate in the UHV regime and need ‘cleaning’ by baking.

An electromagnetic solenoid valve labelled SV (SA0150EVCF, Kurt Lesker) was placed after the turbo pump in the high-vacuum pump region in case of a power failure to prevent air leaking into the vacuum chamber through the scroll and turbo pumps. The bakeout station also has a pneumatic valve for this purpose. Two manual all metal valves, V1 and V2 (9515027, Agilent) can be used to valve off the HV pumps for further protection and for removal or repair of the pumps.

The high vacuum pumps are connected to the main apparatus by a bellows. This bellows connects to ion pump IP1 (9191145, Agilent) through all-metal valve V3 (9515027, Agilent). This bellows is also attached by a tee to all-metal valve V4 and V5. Valve V4 (9515017, Agilent) connects the high vacuum pumps to the 2D MOT chamber portion up above. Valve V5 (9515027, Agilent) connects the 3D MOT and UHV pump region of the apparatus to the high vacuum pumps. Valve V5 also separates the 3D MOT region from the leak valve LV (9515106, Agilent). A convectron gauge (labelled CG2) is present after valves V1 and V2 but can only read down to  $10^{-2}$  Pa ( $10^{-4}$  Torr).

## 5.2 2D MOT section

A 2D MOT is formed from two orthogonal pairs of counterpropagating laser beams travelling along, for example, the  $\pm y$  and  $\pm z$  directions. In addition, magnetic field gradients along those directions are needed, and also appropriate right or left circular polarization choices for the light. There are no trapping laser beams along the  $x$  direction and the field gradient along the  $x$  direction is small compared with the  $y$  and  $z$  direction. This means Rb atoms entering the intersection of the trapping laser beams from a background vapour of Rb will have their  $y$  and  $z$  velocity components decreased in magnitude but not their  $x$  velocity component. As a result an atomic beam will form exiting the trapping region (the intersection of the laser beams) along the  $\pm x$  axis. This atomic beam travels through small tubes connected to the section of the vacuum apparatus where the coils and optics for the 3D MOT reside. A ‘push’ laser beam is sent through the 2D MOT to push atoms in the positive  $x$  direction towards the tubes. The push beam is a collimated laser beam that is approximately the diameter of the tubes, points along the atomic beam axis, and is blue detuned to accelerate the atoms towards the 3D MOT region. The small tubes separating the 2D and 3D MOT regions provide differential pumping where the pressure on the 2D MOT side of the tubes can be high (e.g.  $10^{-6}$  Pa or  $10^{-8}$  Torr) and on the 3D MOT side it can be low (e.g.  $10^{-8}$  Pa or  $10^{-10}$  Torr). The tubes also act as a speed filter so that the speed distribution of the atomic beam travelling to the 3D MOT is significantly below the speed distribution expected from a thermal gas. The 2D MOT is loaded from Rb vapour. An advantage of loading a 3D MOT from a 2D MOT is that the 3D MOT vacuum region can be orders of magnitude lower in pressure. For our case this is important since we want the residual background pressure that the pressure measurements with trapped atoms are performed in to be as low as possible, while still maintaining a sizeable 3D MOT. Another advantage of separating the Rb source from the 3D MOT region is to protect the source while adding in background gas that is reactive with Rb.

### 5.2.1 2D MOT chamber region

The 2D MOT chamber (labelled 2D in Fig. 5.1 and also shown in Fig. 5.3) was custom built (Johnsen Ultravac) with seven ports. Four of these ports form a four-way cross with 4.5 inch CF viewports for light to enter for the 2D MOT. One port along the atomic beam axis is connected to a six way cross (shown in Fig. 5.2). This six way cross connects to the Rb source through

valve V9 (9515014, Agilent). The Rb source consists of a glass ampoule with 1g of Rb (K4584x from ESPI metals). This ampoule has a custom made holder (Johnsen Ultravac). A linear drive mechanism LD (KLPDAA, Kurt Lesker) was installed for the purpose of breaking open the ampoule after baking. The six way cross also connects to the HV pumps when valve V4 is open. Three viewports are installed on the six way cross for looking for Rb fluorescence when filling the 2D MOT chamber with Rb. The viewports in line with the atomic beams axis is also used for viewing the 2D MOT down the atomic beam axis, and for sending in the push beam mentioned above.

The port of the 2D MOT chamber in line with the beam axis, and closest to the 3D MOT section, contains a differential pumping section vacuum-welded into the port. Fig. 5.4 shows a cut away of the differential pumping section of the chamber. The first tube in the differential pumping design separates the 2D MOT chamber, where the Rb vapour resides, from an ion pump (IP2 9191145, Agilent). A second tube then connects the region with the ion pump to the 3D MOT side of the apparatus. The second tube has a graduated opening to allow for divergence in the atomic beam as it propagates towards the 3D MOT. Having the ion pump separated from the Rb vapour helps to preserve the lifetime of the ion pump. The two tubes are lined up along the  $x$  direction (the atomic beam axis). Atoms from the 2D MOT propagate with high directionality along the  $x$  direction and will make it through both tubes. Atoms that randomly make their way into the tubes from the Rb background vapour within the 2D MOT chamber will tend not to be travelling with such high  $x$  directionality and will bounce around in the region between the two tubes until they are removed by the ion pump. The distance from the entrance of the differential pumping tube in the 2D MOT chamber to the center of the cell at the 3D MOT region is approximately 55 cm.

The design of the 2D MOT chamber as well as preliminary design, and ordering, of the vacuum apparatus is credited to Ian Moulton, Weiqi Wang, and Haotian Pang. The mechanical drawings for the 2D MOT chamber and the Rb ampoule holder, as well as differential pumping analysis are found in their report [92]. The Rb ampoule holder design is credited to Dr. Bruce Klappauf.

### 5.2.2 2D MOT coils

Figure 5.5 shows a picture of the 2D MOT coils installed on the 2D MOT chamber. Four rectangular coils are used to produce a magnetic field gradient along the two perpendicular arms of the large four-way cross of the

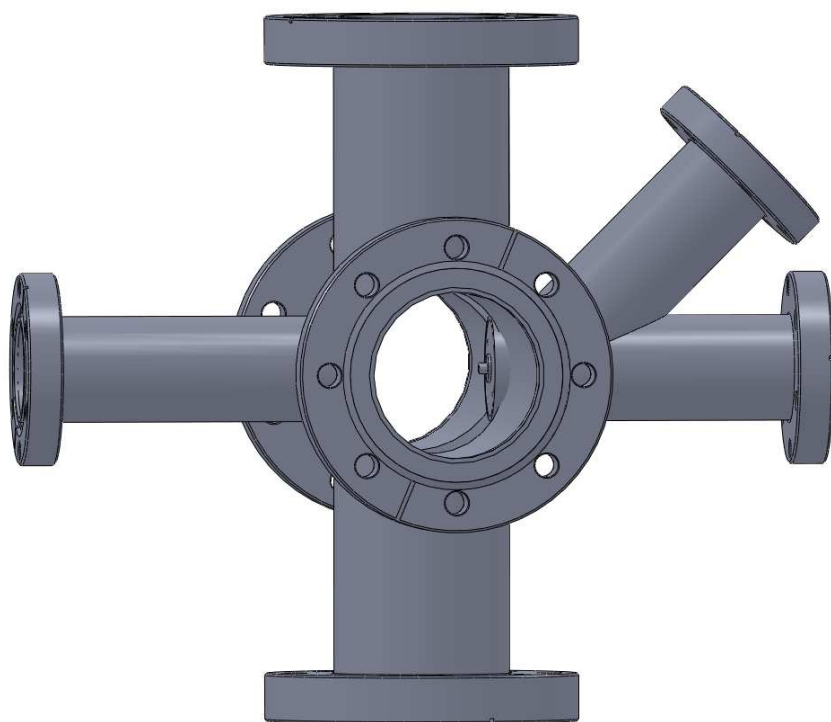


Figure 5.3: The custom made 2D MOT chamber. The differential pumping tube (see Fig. 5.4) can be seen to protrude slightly into the chamber. This tube then leads to an opening where an ion pump is attached on the port that is coming out at a 45 degree angle. A second series of tubes connects this opening to the 3D MOT chamber. The four large ports are for the viewports through which the 2D MOT laser beams are sent. The port on the left in the figure is attached via a six way cross (not shown) to the Rb source and to viewports. A viewport in line with the atomic beam axis is used both to view the 2D MOT and to send a push beam that sends the atoms towards the 3D MOT region.

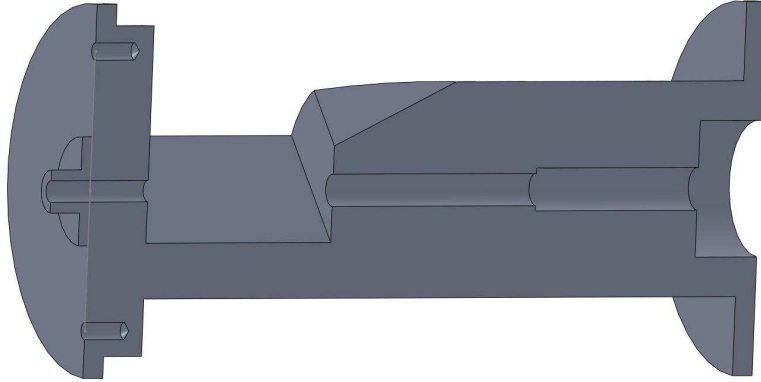


Figure 5.4: A cut away of the differential pumping section. Atoms travel from left to right through one tube and then through another series of tubes before exiting and going to the 3D MOT cell. Atoms in the atomic beam have a high directionality and will make their way through the tubes. Atoms that randomly enter the tubes from the vapour on either side of the 2D or 3D MOT regions will tend to bounce around in the section between the two different tube sections and be pumped away by an ion pump.

2D MOT chamber. Each coil is parallel to the viewport it fits around. The position of the 2D MOT beam axis with respect to the differential pumping tube is optimized by controlling the current to each of the four coils. The inside dimensions of each coil is 8 by 26 cm. The coil pair surrounding the viewports in the  $y$  direction has an inside separation of approximately 8.5 cm and the pair surrounding the viewports in the  $z$  direction is separated by approximately 12.5 cm. There are approximately 10 layers with 12 turns per layer totalling 120 turns. The wire used was 16 AWG magnet wire from Superior Essex (H GP/MR-200). The gradient with 5A going through all the coils was measured using a gaussmeter (model Bell 620) to be 16.6 G/cm ( $1.66 \times 10^{-3}$  T/cm) along the transverse direction and 0.29 G/cm ( $2.9 \times 10^{-5}$  T/cm) along the axial direction.

The inner width of the coils was less than the width of the viewports they slip over. For this reason the 2D MOT rectangular coils were wound on a separable frame (Fig. 5.6) that could be used to wind the coils and then could come away from the coils leaving just the coil. The coil shape once separated from the frame was maintained by wrapping around the coil cross section in a few positions either with high temperature kapton tape or with

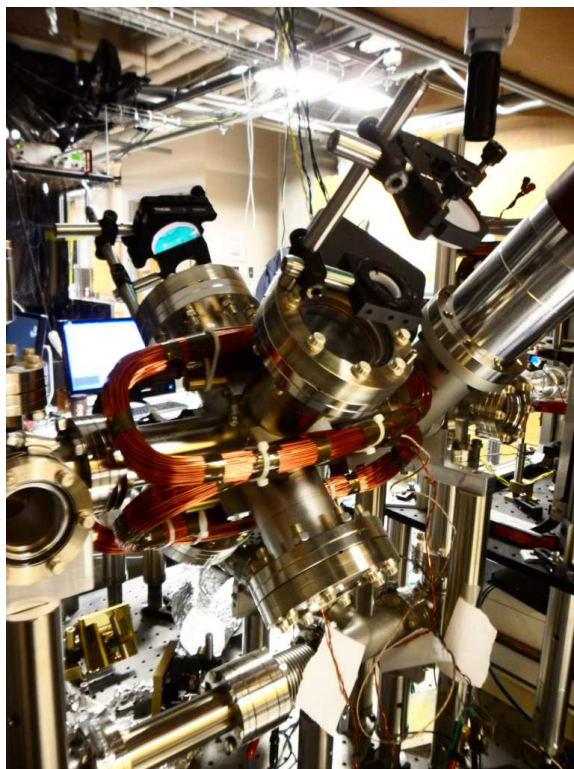


Figure 5.5: Four rectangular coils are slipped around each of the four viewports of the 2D MOT chamber and provide the magnetic field gradient for the 2D MOT.

wire. This allowed the coils to be wound separately first and then installed later which is more convenient than winding the coils in place. This was possible because the inner coil width was large enough, and the coils flexible enough, that the coils, with slight deformation, could be slipped over the viewports of the four-way cross of the 2D MOT chamber. The design and manufacture of this frame as well as initial simulations of the 2D MOT coils is credited to Kousha Talebian. Electrical tape was placed on the frame surface to prevent the wire from scratching on the frame when winding. Scratches could lead to the removal of the insulating layer on the wires and shorting. The coils were wound by hand with feet placed on a rod going through the wire spool providing tension. The start of the first winding was secured so that the wire did not move around when the coil winding was

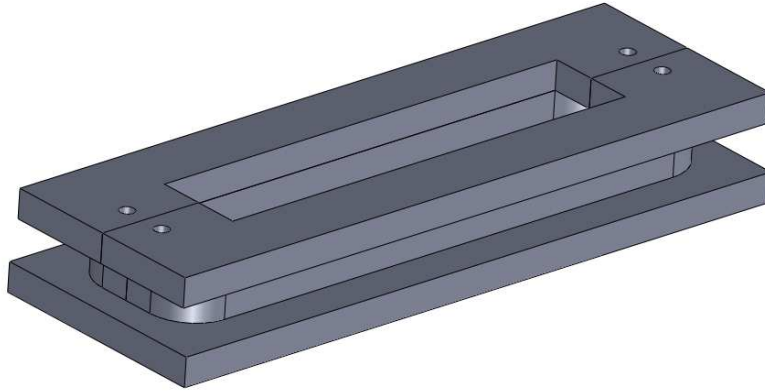


Figure 5.6: A drawing of the frame used to wind the 2D MOT coils. The frame is made to separate away from the coils once the coils are wound. The coils are held together by wrapping high temperature kapton tape around the coils in a few places. The coils could then be slipped over the viewports of the 2D MOT chamber.

getting started. Plastic wrap was placed over the viewports and over the bolts securing the viewports to the 2D MOT chamber when putting on the coils to prevent either the coils or the viewports from being scratched.

One of the coils needed to be mounted before the ion pump used for the differential pumping in the 2D MOT chamber could be installed. This coil can not be removed and was present during baking. The three others coils were not present during baking and are removable. The magnet wire used for the coils has an insulating layer of polyester/polyamideimide (which is not kapton). This coating has a limited lifetime above  $215^{\circ}\text{C}$  and Kapton coated wire should be used if a higher temperature limit is needed. After baking for a long period of time (a month) near the upper temperature limit and then cooling down to room temperature, small cracks formed at stress points so that extreme care should be taken in handling these coils so that the coating is not rubbed off causing shorts.

Credit goes to Vandna Gokhroo and Wolfgang Müssel for helpful advice concerning the alignment and detection of the 2D and 3D MOT. Also Refs. [93–95] the following papers were useful in the design of the 2D MOT magnetic coils and the optics planning.

### 5.3 3D MOT section

The 2D MOT chamber is separated from the 3D MOT section by an all-metal gate valve (48132-CE01-0002, VAT valve). After the gate valve is a six-way cross with viewports for diagnosing the 2D MOT beam characteristics exiting the differential pumping tubes. The six way cross connects to an ion pump, leak valve and turbo and scroll pumps through valve V5 in Fig. 5.1. This six way cross is also attached to a glass cell into which laser beams for the 3D MOT are sent. This glass cell is rectangular in shape where the laser beams enter. The cross section of the cell is square with inner dimensions of 40 mm by 40 mm and the cell is 90 mm long. Magnetic coils are also needed for the 3D MOT and are representatively shown in Fig. 5.1 and Fig. 5.2.

### 5.4 UHV pumps and diagnostics

Several gauges are attached to the UHV region (the part numbers and specifications are given in chapter 4). A capacitance diaphragm gauge (labelled CDG in Fig. 5.1) was installed to calibrate a spinning rotary gauge, which in turn was installed to calibrate an ion gauge. Pressure measurements with the ion gauge (IG) will be compared with the measurements provided by trapped atoms. A residual gas analyzer (RGA) is also installed for analysis of the different species present in the background, for background gas detection, and for comparative differential pressure measurements.

The UHV section has a titanium sublimation pump attached to it (labelled TSP, 916-0050, Agilent). A non-evaporable getter pump (NEG, C 400-2-DSK ,SAES getters) and an ion pump (IP3, VacIon Plus 20, 9191145, Agilent) are also attached to achieve a low background pressure. These pumps are behind a valve (V6, VZCR60R, Kurt Lesker) so that they can be isolated from the 3D MOT region during any pressure measurements to reduce pressure gradients and to protect the pumps. An elbow is installed between the valve V6 and the TSP, NEG, and IP3, to prevent Titanium from the Ti-sub pump coating the valve which is exposed to the 3D MOT cell when the valve is closed.

The titanium sublimation pump and the non-evaporable getter in our system work by chemisorption [61]. Chemisorption is when a material (titanium or Zr V Fe in the case of our NEG) has a high binding energy for active gases such as O<sub>2</sub>, N<sub>2</sub>, CO<sub>2</sub> and H<sub>2</sub> so that these gases adhere to the material. The titanium sublimation pump shown in Fig. 5.7 consists of titanium filaments that are heated. At a sufficiently high temperature the

titanium evaporates forming a film on the surrounding walls of the chamber which can then pump gases from the system. The titanium is evaporated at intervals forming a fresh layer over trapped material adsorbed onto previous layers.

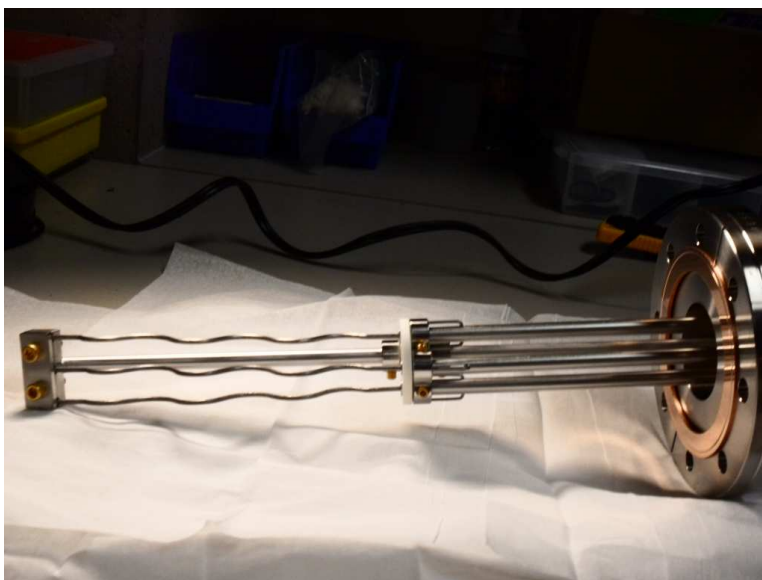


Figure 5.7: A picture of the titanium sublimation pump. The wavy metal is three titanium filaments. They are mounted such that high currents can be put through them sublimating the titanium and coating surrounding structures in the vacuum apparatus. This thin titanium layer coating acts like a pump because gases bind to it.

Our non-evaporable getter is ZrVFe arranged in disks to have a large surface area. The getter is activated occasionally by heating causing the external monolayer of gases adhering to the surface to move within the getter material allowing a fresh surface for continued pumping. The getter is then cooled because the lower the temperature of the getter, the lower the base pressure of  $H_2$  realized in the system. About 90-100 activations can be performed, with the time between activations depending on the gas input to the system, how often the system is baked, and how often it is vented to atmosphere. The getter is reaching its end of use when the hydrogen pressure slowly rises and re-activation leads to a baseline hydrogen pressure that is higher than for previous re-activations. The getter pumps hydrogen

and active gases well: however, the getter pumps do not pump inert gases. These pumps are typically used to achieve and maintain UHV but can only be activated once a sufficiently low pressure has already been achieved by other pumps such as the scroll, ion, and turbo pumps.

Ion pumps (VacIon Plus 20, 9191145, Agilent) are placed in several locations of our apparatus. Ion pumps have an ultimate pressure of less than  $10^{-9}$  Pa ( $10^{-11}$  Torr) and should not be turned on above  $10^{-1}$  Pa ( $10^{-3}$  Torr). In ion pumps electrons are discharged from cathodes towards an anode. Magnetic fields are used to maximize the electron trajectory length by producing spiral trajectories. During its trajectory an electron can ionize gases found in the system creating positive ions which are then accelerated towards a negatively charged cathode. This cathode is typically made of titanium so that the ions react with the titanium and are removed from the system. Also neutral gases can react with the titanium as in a titanium sublimation pump. When the ions hit the cathode they have sufficient energy to knock out or ‘sputter’ titanium from the cathode which coats surfaces with fresh titanium [61, 65]. Ionized noble gases can be pumped by being accelerated towards the cathode and being buried within the cathode material. They are further buried by incoming sputtered cathode material.

Part of the 3D MOT section is also a connection to Rb dispensers (Rb D, AS-3-Rb-50-V, Alvatec) which can be valved off with valve V7 (9515027, Agilent) if not needed. These were installed for trouble shooting purposes in case a 3D MOT could not be achieved easily at first using the 2D MOT.

## 5.5 Vacuum apparatus assembly

This section describes the assembly steps of the vacuum apparatus. The vacuum apparatus was assembled from the 2D MOT side towards the 3D MOT side. All the standard stainless steel vacuum components were assembled first, except for the gauges, pumps, and Rb sources. Mounts for 2.5 inch ConFlat (CF) flanges and 4.5 inch CF flanges were machined and mounted on to 1.5 inch diameter posts to hold up the vacuum apparatus. The CF flanges are secured to the mounts using hose clamps that are cut and screwed to the mounts. The height from the optical table top to the center of the cell where the atoms are trapped in the 3D MOT is 17.5 inches. The reason the trapped atom location quite high relative to the table top is that the apparatus was designed to be as narrow as possible, leaving room for surrounding optics. This pushed part of the apparatus upwards.

Each piece used for ultra-high vacuum has one or multiple CF flanges

to connect to other pieces. A CF flange consists of a sharp knife edge. A copper gasket is placed between two CF flanges and a seal is formed when the flanges are bolted and tightened together. If the connection is ever taken apart (vacuum is broken) then a new gasket must be used. Scratches in the gaskets can prevent proper sealing. It is sometimes hard to hold the gasket in place while holding pieces together and putting in screws and bolts. A helpful suggestion from a labmate was to put kapton tape on the edges of the copper gasket to secure it to the conflat flange while connecting flanges. This prevents the gasket from falling out while tightening the bolts. The tape is removed after the flanges and bolts have been finger-tightened together. The flange bolts are tightened in opposing pairs to maintain uniform cutting of the flanges into the gasket. The bolts are tightened until a sliver of copper gasket can still be seen so that, in the case of a leak, the bolts can be further tightened and to allow for expansion when baking. Wherever possible silver bolts ( eg. TBS25028125P from Kurt Lesker) are used to prevent seizing after baking. Otherwise an anti-seize compound (VZTL from Kurt Lesker) can be used but care should be taken not to introduce the compound to the vacuum side of the flanges.

All CF connections on the tee and valve V9 that are attached to the Rb ampoule RbA have Ni annealed gaskets (GA-0275NIA and GA-0133NIA, Kurt Lesker) since this region comes in the highest contact with Rb. The viewports on the apparatus have annealed copper gaskets (VZCUA38 and VZCUA64, Kurt Lesker) rather than regular copper gaskets to put less stress on the viewport which reduces the chance of the viewports developing a leak.

No precleaning of vacuum parts was used (they are precleaned from the factory). Gloves were used at all times and changed frequently. Care was taken not to talk or breathe into the vacuum apparatus. The bellows on the Rb cell was scrubbed with a bottle washer withalconox, sonicated inalconox for 1 hr, then in distilled water, then in acetone and then in methanol. The bellows side of the cell was attached to the 2D MOT side of the apparatus to strain relieve the connection of the cell to the 2D MOT region while all the components on the other side of the cell were being added. The compensation coil pair, shown in Fig. 5.12, that encircle the cell were put in at this stage. There are three pairs of compensation coils in total to allow a magnetic field to be added to the magnetic field from the 3D MOT magnetic coils. These coils were installed for planned optical-dipole trapping in the far future.

Another part that had to be cleaned was the electrical feedthrough which was machined (cut down and holes inserted) so that the Rb dispenser tabs could be put through. The feedthrough was cleaned with methanol sonica-

tion after machining. The NEG holder was also sonicated in methanol. Both the NEG holder and the feedthrough have ceramic parts deeper inside the pieces and it is recommended not to get these wet with methanol or other solvents since the ceramic will absorb it and outgas later under vacuum.

The apparatus was leak-tested periodically as it was being built by blanking off all openings, pumping down using our bakeout station, and then spraying He around the CF flange joints. The residual gas analyzer on the bakeout station described in section 3.1 was used to detect any He entering the system. Once the main vacuum apparatus frame was in place, the Ti-sub pump was installed.

The ion pumps were installed next with the magnets left on. As mentioned, the 2D MOT coil which wraps around the ion pump port on the 2D MOT chamber was installed prior to connecting the ion pump. The ion pumps are shipped under vacuum, sealed off with a CF flange. This flange has a bolt hole in it into which one can insert a bolt and use the bolt to remove the flange, which is held tightly onto the pump due to the low pressure inside and the high pressure outside. The bakeable cables were attached to the ion pumps since the ion pumps needed to be turned on towards the end of the baking phase (described in the next section). The optical table surface is grounded using a metal braid attached to grounded electrical piping in the lab. This provides grounding to the vacuum apparatus through the mounts holding the vacuum apparatus up.

Pressure gauges were installed as per their manuals consisting mostly of routine connections of CF flanges. The spinning rotary gauge was installed using a level since the axis of the measurement head needs to be vertical within  $\pm 1^\circ$ . After the gauges were installed two Rb dispensers were installed. Finally the NEG was installed. It was clear that the standard 2.75 inch CF nipple was too small in diameter as the NEG scrapes the walls. If vacuum is ever broken, it is recommended to buy and install the manufacturer designed pump body for the NEG or to install the NEG in a larger diameter flange so that the pumping capacity is not limited as it is now. Also the capacitance diaphragm gauge should be oriented so that the housing can come off and the cables removed. Consideration of putting on a valve on any of the gauges should be made in case one wants to disconnect them and send them away for calibration or repair. Additional recommended changes include the installation of a cooling sleeve on the Ti-Sub (9190180, Agilent). Credit is given to Ian Moulton, Weiqi Wang, and Haotian Pang, Dr. James Booth, Dr. Kirk Madison, and Kousha Talebian for work on planning of the apparatus, purchasing, assembly and baking out of the apparatus.

## 5.6 Bakeout Procedure

Baking out a vacuum apparatus involves heating the apparatus to high temperatures (above  $100^{\circ}\text{C}$ ) to drive the water and other gases like  $\text{H}_2$ ,  $\text{CO}_2$ , and  $\text{O}_2$  off of the vacuum apparatus walls and to pump them away.

### 5.6.1 Oven

To bakeout the chamber, an oven was formed around the vacuum apparatus on the optical table (see Fig. 5.8). Firebricks (K23 Firebrick and 3 feet by 1

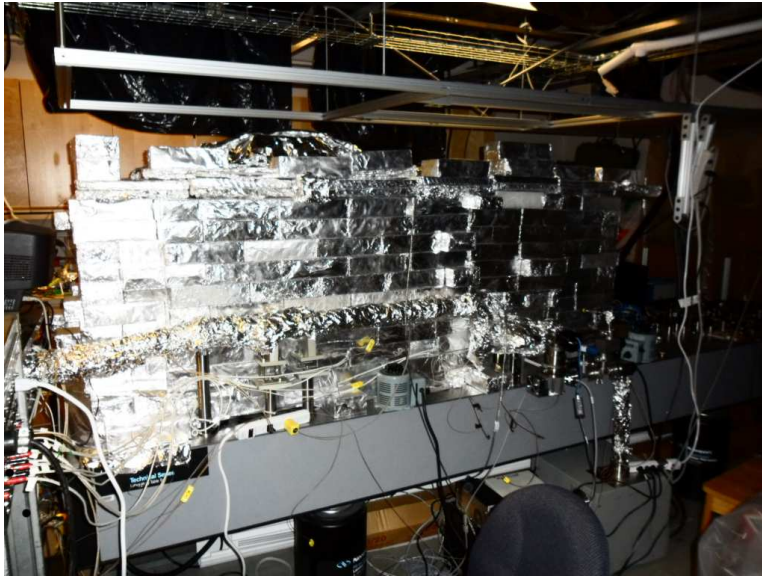


Figure 5.8: A picture of the oven built around the setup to bakeout the vacuum apparatus.

feet by 1 inch Fibre Block Insulation from Greenbarn Potters Supply) were used to form the oven. They were wrapped in aluminum foil to prevent the dust from the porous firebrick material from getting everywhere. Two layers of firebricks were put down on a layer of aluminum foil on the optical table around the base of the vacuum setup. A few bricks were cut to try to fill in gaps in this bottom layer and aluminum foil was scrunched up and put in to fill remaining gaps. Five infrared heaters (900 W Infrared Salamander heaters from Mor Electric Heating Assoc., Inc) powered individually by a variac were placed on this base layer of bricks at roughly equally spaced

locations. Thermocouple gauges were also placed at various positions of the chamber to monitor the temperature while baking out. The thermocouple gauges were assembled from Newark part numbers (93F9305, 93F9313, 50B5932, 93B0462). The firebricks have dimensions of roughly 9" by 4.5" by 2" and the overall dimensions of the oven was approximately 7 feet by 3 feet by 3 feet and required around 420 firebricks. The lid of the oven was made from 3 feet by 1 feet by 1 inch Fibre block insulation with double layers put on top.

### 5.6.2 Pre-bake preparation

Before any of the oven was formed we removed the wooden platform above the optical table and the HEPA filter to reduce the amount of heat trapped, to protect the filter and to allow the oven to be built tall enough to surround the vacuum apparatus. In preparation for the bakeout aluminum foil was placed in thick layers around the viewports and cell to protect against temperature gradients and anything melting onto them. The plastic handles for the gate valve (labelled GV in Fig. 5.1), 4.5" CF valve (labelled V6) and the linear drive mechanism (labelled LD) were removed. The linear drive mechanism was locked so as not to break the Rb ampoule. Any electrical connections to the ion gauge, residual gas analyzer, capacitance diaphragm gauge as well as the spinning rotary gauge measurement head were not installed prior to baking and must be removed for any future baking. Any stickers or plastic were also removed. The all-metal valves as well as the gate valve were open fully. The leak valve (labelled LV) was kept closed.

Heater tapes powered by variacs were also used for heating the parts of the vacuum apparatus not contained in the oven such as the bellows connecting the apparatus to the bakeout station. The lab's 'bakeout station' consists of a scroll and turbo pump for pumping, an ion gauge to indicate the pressure, a residual gas analyzer, and a bank of inputs for thermocouple gauges. A labview program collected the temperature readings of the thermocouple gauges and the pressure from the bakeout station ion gauge.

Before starting to bake the system we pumped on the vacuum apparatus using the bakeout station to a pressure of  $9.3 \times 10^{-6}$  Pa ( $7 \times 10^{-8}$  Torr) as read by the ion gauge on the bake-out station. Initially we ran 30 A through each Ti-Sub filament just to test the Ti-Sub filament controller; the pressure rose to the high  $10^{-2}$  Pa ( $10^{-4}$  Torr) range and then decreased. The Ti-Sub filaments were then turned off. After pumping down to the  $10^{-6}$  Pa ( $10^{-8}$  Torr) range again, the NEG was activated. To activate the NEG, DC voltage was applied in steps of 1V/min up to 16V which is then

left for 60 min. The heating curves provided by SAES Getters give a getter temperature of 475°C at 16V. Again pressure in the range of  $10^{-2}$  Pa ( $10^{-4}$  Torr) is reached when the NEG is being heated due to outgassing. It was noted that when first applying voltage, the current predicted through the NEG by SAES Getters was about a factor of two off of their provided curves. This is because the resistance of the NEG increases as it is being heated so that the current will match the measurements provided by SAES Getters after some wait time. While the NEG was at 16 V the TSP filaments were outgassed by running each in turn at 37 A for 1.5 min. Once the NEG was activated the voltage was brought down to 7V which corresponds to a getter temperature of 250°C and was left at that voltage for the duration of the bakeout so that the NEG would be hotter than the rest of vacuum apparatus. The coldest spot in the apparatus is where outgassed material preferentially sticks. The TSP controller can only send current through one of the three filaments at a time, so for the remainder of the bake-out we cycled from filament to filament running 30A continuously through them. When changing from one filament to another the pressure increased by about 10 times and then decreased.

### **5.6.3 Baking**

The actual baking started by increasing the voltage to the infrared heaters in 5V intervals waiting for the temperature inside given by the thermocouples to stabilize in between. The time to reach a steady temperature after each increase of variac voltage to the heaters was around 12 hours. A temperature goal of 180°C in the oven was set since the RGA, linear drive mechanism, and the capacitance diaphragm gauge cables all have a maximum temperature of 200°C. At the bottom of the oven the temperature attained to was 157°C with temperature rising up to 185°C at the top of the 3D MOT cell and then decreasing to 179°C at the top of the RGA since this is close to the top cover of the oven where heat escapes. The hottest place in the oven was on top of the 4 way cross containing the NEG and Ti-Sub filaments at 200°C. This is because the NEG and Ti-Sub filaments were additionally being heated by running current through them.

The oven was brought up first in temperature with the outside bellows lagging behind in temperature so as not to outgas material from the hot bellows into a colder main apparatus. Since the bakeout was low temperature compared to typical bakeout temperatures, we baked out for a longer time period of about 1 month. During bakeout the maximum pressure attained at maximum temperature was  $2.9 \times 10^{-4}$  Pa ( $2.2 \times 10^{-6}$  Torr). While pump-

ing, it decreased to  $3.3 \times 10^{-5}$  Pa ( $2.5 \times 10^{-7}$  Torr) with both the bakeout station (one turbo, one scroll pump) and the main apparatus pumps (two turbo's and one scroll pump). The Ti-sub filaments were run at 40 A for 1.5 min. After that 30A was used continuously, cycling through the filaments occasionally.

At this stage the ion pumps were turned on and baked for another week. Though others [96] valve off their turbo pumps at this point we found that valving them off caused the pressure to rise 2 to 5 times and so we kept the turbo pumps and scroll pumps pumping on the system while the ion pumps were pumping.

#### 5.6.4 Cooling

Cool down occurred slowly over the course of two days where the bellows were kept colder than the main chamber. When the experimental chamber was below 100°C, the NEG was reactivated at 16V for 60 min and then turned to zero. The current to the Ti-sub was also shut off. The system then was allowed to completely cool down. When cooled the ion gauge on the bake-out station 'flat lined' at the lowest reading of  $1.35 \times 10^{-6}$  Pa ( $1.01 \times 10^{-8}$  Torr). The ion current readout from the ion pumps, which is proportional to the pressure in the system, went down when the turbos were valved off. This means that at that stage the ion pumps were doing a more effective job of pumping than the turbos and the scroll pumps. At this stage we closed valve V1 to the bakeout system and the solenoid valve SV to the high vacuum experimental pumps. 48 A was put through one of the Ti-sub filaments several times with a maximum duration of two minutes and a minimum of 30 seconds to sublimate the titanium and coat the surrounding chamber walls. The ion gauge pressure reading on our experimental apparatus dropped to  $2.3 \times 10^{-8}$  Pa ( $1.7 \times 10^{-10}$  Torr), over the course of a day. The next step was to break the Rb ampoule and see if the system needed more baking due to the gases released in the ampoule.

### 5.7 Rb release from the ampoule

While baking, the Rb for the 2D MOT was inside of a sealed glass ampoule. The UHV section was valved off from the pumps before the ampoule was broken. The gate valve GV was closed connecting the 2D and 3D MOT sections and the valve V3 to the ion pump IP3 closest to the high vacuum pumps was also closed. The reason for this was to protect the 3D MOT region and UHV pumps from contamination while breaking the ampoule.

Valves V1, V4, and V9 were left open so that the 2D MOT section could be pumped on while the Rb ampoule was being broken and heated. Breaking the ampoule involved pushing the linear drive mechanism over the top of the Rb ampoule to break the glass which was prescored so that the top snapped off easily. When the ampoule broke the Ar in the ampoule was released and the pressure went above  $10^{-2}$  Pa ( $10^{-4}$  Torr) dropping rapidly as the Ar was pumped away.

Once the ampoule was broken, the custom holder and the tee holding the Rb ampoule was wrapped in heater tape and heated up over several hours to 75 °C. This was to release Rb vapour into the 2D MOT chamber so that there is Rb to trap in the 2D MOT. The 2D MOT chamber was pumped on using the bakeout station and several (5-10) Ar bursts from Ar trapped inside the Rb were seen on a RGA. A laser beam was shone through a viewport close to the ampoule region to detect Rb release from the ampoule. The laser frequency was scanned over the  $5^2S_{1/2}$  to  $5^2P_{3/2}$  transition of  $^{85}\text{Rb}$ . A photodetector was also placed close to the beam to detect fluorescence and the photodetector readout on an oscilloscope was averaged to reduce noise. Once the ampoule region was at 75 °C, it took several hours to see fluorescence close to the ampoule region. Upon cooling of the ampoule, the valve connecting the 2D MOT chamber to the turbo and scroll pump (V4), and the valve for the Rb ampoule (V9), were closed by hand.

A few days later the ampoule was heated again up to 86 °C while pumping on the 2D MOT chamber using the turbo and scroll pump on the bakeout station. Again valve V4 and V9 were open for heating and closed while cooling.

Several weeks later we opened up the Rb ampoule valve V9 (no heating). The gate valve (GV) was open also and the pressure in the UHV region shot up to  $10^{-3}$  Pa ( $10^{-5}$  Torr). The UHV section was then opened to the bakeout station pumps and the UHV region recovered to the  $10^{-7}$  Pa ( $10^{-9}$  Torr) range from the  $10^{-8}$  ( $10^{-10}$  Torr) range previous to the leak. The leak was traced to a seal at the top of the Rb ampoule valve V9. Tightening this seal stopped the leak as determined by a He test detected with the RGA on the bakeout station. The ampoule valve V9 had its top uncovered to air to allow access to tighten it while the bottom portion was heated so it seems that the temperature differential on the valve caused the leak. The heater tape was moved away from the valve and the ampoule was heated to 95 °C for about an hour. After this, valve V4 connecting the 2D MOT chamber was closed and the rubidium ampoule valve V9 was left open.

After the leak was fixed, running the Ti-Sub pump several times for 1-

2 min at 48 A allowed the pressure to decrease to around  $2.7 \times 10^{-8}$  Pa ( $2 \times 10^{-10}$  Torr). The NEG was also reactivated but it is not clear that helped as the baseline pressure was initially higher than before with very slow decrease. Again the Ti-Sub was run around 1.5 min several times and then the UHV section pressure slowly made its way to  $1.25 \times 10^{-8}$  Pa ( $9.4 \times 10^{-11}$  Torr) over the course of several months with valve V5 closed. This is from an original low of  $1.2 \times 10^{-8}$  Pa ( $8.9 \times 10^{-11}$  Torr) prior to the leak. Currently the base pressure with only the UHV pumps is  $8.9 \times 10^{-9}$  Pa ( $6.7 \times 10^{-11}$  Torr).

After breaking and heating the ampoule, the next step was to try to produce a 2D MOT. The next section explains the optical setup used for creating a 2D MOT and for the first version of the 3D MOT.

## 5.8 Optics

The  $5^2S_{1/2}$  to  $5^2P_{3/2}$  D<sub>2</sub> transition is used for trapping of either  $^{85}\text{Rb}$  or  $^{87}\text{Rb}$ . The laser pump is chosen to be the  $F = 2$  to  $F' = 3$  transition for  $^{87}\text{Rb}$  or  $F = 3$  to  $F' = 4$  transition for  $^{85}\text{Rb}$ . The repump is chosen to be the  $F = 1$  to  $F' = 2$  transition for  $^{87}\text{Rb}$  or  $F = 2$  to  $F' = 3$  transition for  $^{85}\text{Rb}$ . Light that is 180 MHz below the repump and pump transitions, for either  $^{87}\text{Rb}$  or  $^{85}\text{Rb}$ , is brought over by optical fibers to the experimental table from a central optical table. This central table provides the initial frequency stabilized light for all of our experimental tables [50, 51]. The fibers used between the central and experimental tables are from OZ optics.

The main optical setup to provide light for the 2D and 3D MOT is shown in Fig. 5.9. A list of optical components used in the setup with part numbers is given in Table. 5.1

For the repump, light arriving by fiber from the central table (1.5 mW) injects a slave laser diode (MeshTel MLD780-100S5P at 18 °C). The slave laser diode output is 44 mW. This laser-diode light is shifted up to an experimental frequency of 4.5 MHz below resonance using an acousto-optical modulator (AOM) in a double pass configuration. Part of the repump light is used for the 2D MOT (5.7 mW in each arm to total 11.4 mW). The remainder of the repump is coupled into a fiber that leads to a 2 by 6 fiber splitter (Evanescent Optics Inc) used for the 3D MOT. There is 0.25 mW repump light in each of the six fiber outputs of the splitter.

The pump light, arriving by fiber from the central table (1.1 mW), injects a slave (again MeshTel MLD780-100S5P at 18 °C). This slave light is coupled into a fiber and about 10.3 mW is sent into a tapered amplifier (TA).

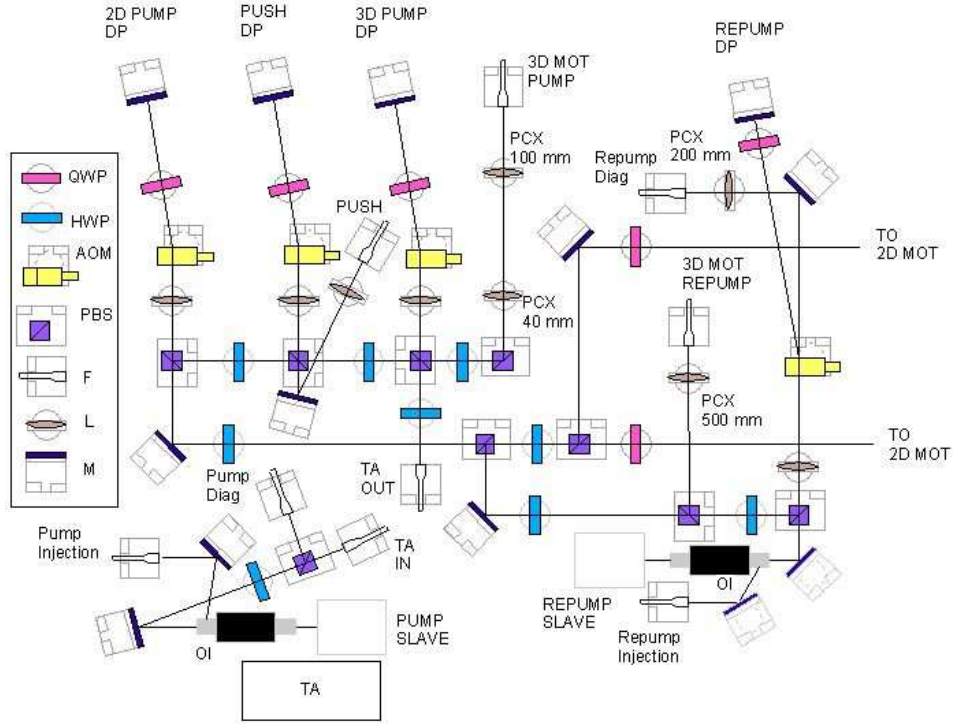


Figure 5.9: A schematic of the optical setup. QWP: quarter wave plate. HWP: half wave plate. AOM: acousto-optical modulator. L: plano-convex lens ( $f = 300$  mm unless otherwise noted). PBS: polarizing beam splitting cube. F: fiber output/input using a fiber collimator. M: mirror. The repump slave light frequency is set by an AOM in double pass configuration (REPUMP DP). The repump light is sent to a fiber (3D MOT repump) for use in the 3D MOT. The rest is sent to the 2D MOT to form the two arms of the 2D MOT. The pump slave light is sent to a fiber (TA IN) which is sent to the tapered amplifier (TA). The output of the tapered amplifier (TA OUT) is sent to three AOM double passes (2D PUMP DP, PUSH DP, and 3D PUMP DP). The 2D pump light produced by 2D PUMP DP is sent free space to the 2D MOT chamber and is combined with the repump light. Push light for the 2D MOT is produced by PUSH DP and is coupled into fiber PUSH. The 3D pump light is produced by 3D PUMP DP and is sent into a fiber labelled 3D MOT PUMP. The 3D MOT PUMP and 3D MOT REPUMP fibers are coupled to a 2 by 6 fiber splitter (Evanescence Optics) used for the 3D MOT. Pump diag and Repump diag: fibers to send slave light to a fabry-perot cavity and absorption signal from a Rb vapour cell to ensure the slaves are injected. OI: optical isolator. Irises (not shown) are used to block unwanted orders from the AOMs.

Table 5.1: Optical Components used in Fig. 5.9

Component	Part Number	Vendor
Quarter wave plate	WPL1212-L/4-780	Casix
Half wave plate	WPL1212-L/2-780	Casix
Acousto-optical modulator	ATD-801A2	IntraAction Corp.
Polarizing Beam Splitter	BPS0202	Casix
Fiber collimator	F230FC-B	Thorlabs
Mirror	45606	Edmund Optics
Optical Isolator	I-80-T4-H	Isowave
Tapered Amplifier	TEC-400-0780-2500	Sacher Lasertechnik
Laser diode	MLD780-100S5P	MeshTel
Lenses	various e.g. LA1484-B	Thorlabs
Irises	53914	Edmund Optics
Fiber collimator	F230FC-B	Thorlabs

The TA generates approximately 1W out of a high-power output fiber. A tapered amplifier is a semiconductor gain medium with a tapered shape. A small sized input beam to the tapered amplifier with reasonable powers can achieve significant amplification. The tapered amplifier (TA) is from Sacher Lasertechnik (TEC-400-0780-2500) with a fiber-coupled input and output.

The TA light is sent to three double pass AOMs. One double pass AOM is for the 3D MOT pump light, which is fiber-coupled into the 2 by 6 splitter. There is 15-18 mW 3D pump light in each of the six fibers. The 3D pump is operated at 11.2 MHz below resonance. A second double pass AOM is for the push beam for the 2D MOT, which is also fiber-coupled. The push beam has 0.4-0.6 mW power and is approximately 2 mm diameter. A third double pass is for the 2D MOT pump light. The 2D pump light is combined with the repump and is sent free space to the 2D MOT chamber. The next section describes the optics used to expand the 2D MOT pump and repump to the size needed for the 2D MOT.

### 5.8.1 2D MOT optics

There is 54 mW pump light in each 2D MOT arm (108 mW total). The 2D MOT pump operates 12 MHz below resonance and the push beam is 10.6 MHz above resonance. The 2D MOT beam for each arm of the 2D MOT is increased in size with several lenses to a size of approximately 25 mm diameter. Fig. 5.10 shows the lenses and mirrors used to expand the

2D MOT pump and repump beams and direct these beams into the 2D MOT chamber. Only one arm of the 2D MOT is shown, but the other arm has identical optics. The pump and repump beams for the 2D MOT are expanded using a -50 mm focal length plano concave lens (1 inch diameter lens), labelled L1 in Fig. 5.10, then a -75 mm focal length plano concave lens (1 inch diameter), labelled L2, and finally a 3 inch diameter plano convex +200 mm focal length lens, labelled L3. The mirrors used to direct the expanded laser beams to the 2D MOT chamber are 75 mm by 75 mm and are from Edmund optics (part number 45341). The direction of the push beam from a fiber collimator is shown in Fig. 5.10 as well.

The 2D MOT was aligned so that the outer edge of the beams clip on the entrance of the differential pumping tube. This ensures that the 2D MOT cloud is close to the tube. Looking down the axis of the atomic beam with a camera focused on the differential pumping tube entrance, we were able to see the fluorescence of the laser beams and atoms collected in the 2D MOT (see Fig. 5.11). With independent control of each of the four 2D MOT coils, we aligned the 2D MOT to visually overlap with the differential pumping tube entrance. With the camera removed, the push beam was sent down the atomic axis. The push beam was aligned to pass through the differential pumping tubes by sending a flashlight down from the other end of the apparatus and aligning the push beam to that.

### **5.8.2 3D MOT optics**

This section describes the optics used for the 3D MOT, as shown in Fig. 5.12. Setting up the 3D MOT turned out to be the best way to initially detect flux coming from the 2D MOT and to optimize the 2D MOT. The initial signals from methods to detect the flux, that are described in the next chapter, were too weak to detect the presence of the beam.

For the 3D MOT, three of the six fibers from the fiber-splitter were used to make a retroreflection MOT. The other three fibers were used for general purposes such as the beam divergence measurement described in the next chapter. Each arm of the 3D MOT consists of a bare fiber output followed by a lens (100 mm PCX) and a 1-inch quarter waveplate (see Fig. 5.12). The optics are mounted using cage mount components from Thorlabs. To provide a retroreflection, a quarter waveplate and mirror are placed on the opposite side of the cell. The 3D MOT optics are mounted on an 80 20 frame that is used to support the compensation coils. These coils are not currently in use, but would be for loading into an optical dipole trap, which may be implemented in the future. There are six compensation coils in total, two

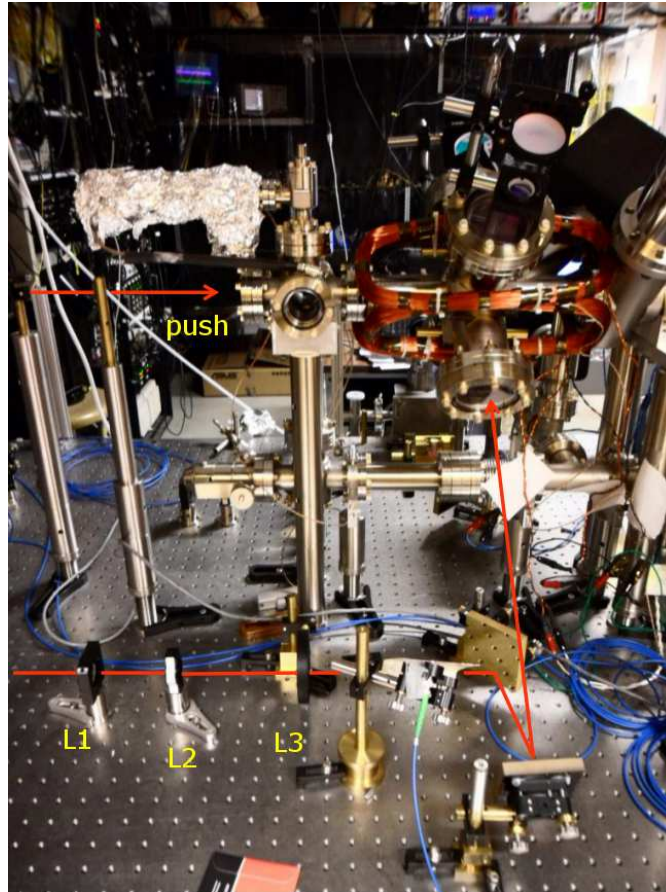


Figure 5.10: A picture of the lenses and mirrors used for expanding the 2D MOT pump and repump along one arm and sending them to the 2D MOT chamber. L1 is a  $f = -50$  mm plano concave lens, L2 is a  $f = -75$  mm plano concave lens and L3 is a  $f = + 200$  mm plano convex lens. On the opposite side is a quarter waveplate and a mirror for retroreflection. Only one arm of the 2D MOT beams is shown. The other arm is identical coming into the 2D MOT chamber perpendicularly to the laser beams depicted in this figure. The push beam orientation and path of travel is also shown.

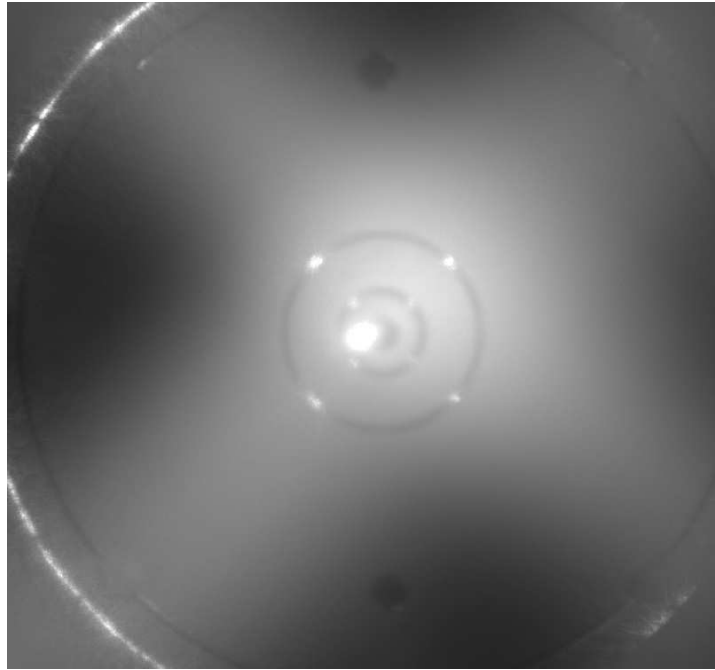


Figure 5.11: A picture of the 2D MOT cloud. The differential pumping tube can be seen in the background. The fluorescence from the laser beams can also be seen.

of which encircle the cell and had to be installed prior to the cell during the vacuum assembly. The 3D MOT loading rate was optimized using a parameter search over the 2D MOT coil currents, 3D MOT coil current, and the detuning and power of the 2D pump, repump, 3D pump and push light. Credit goes to Victor Barua for writing the optimization code.

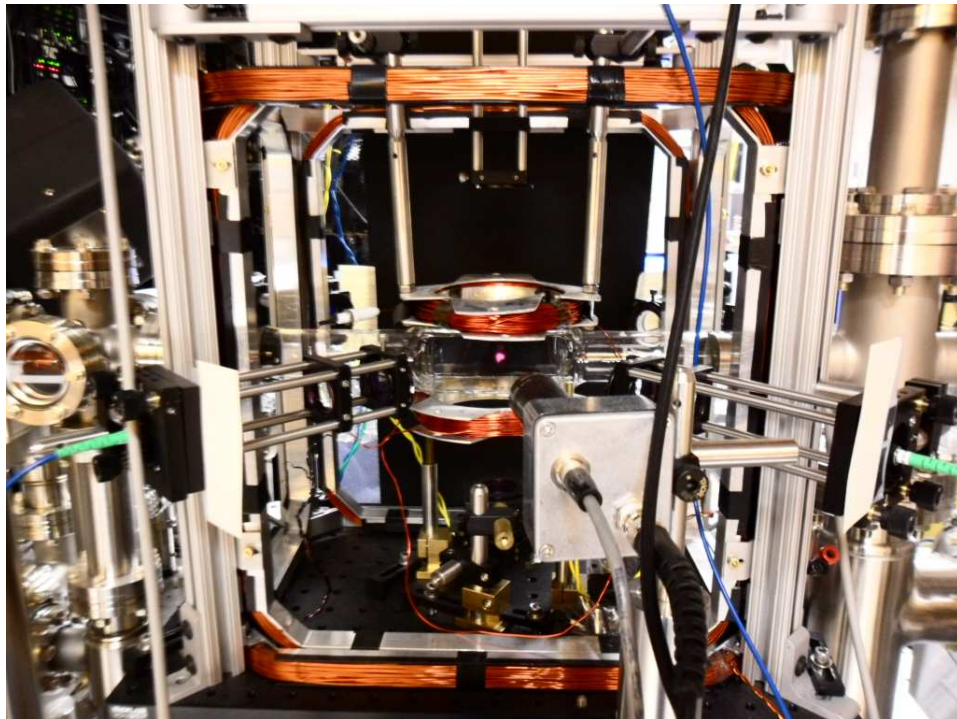


Figure 5.12: A picture of a 3D MOT loaded from the 2D MOT.

## Chapter 6

# 2D MOT characterization

This chapter provides some characterization of the Rb beam coming from the 2D MOT, such as the beam divergence, the flux in the atomic beam, and the capturable speed distribution.

### 6.1 Rubidium atomic beam divergence characterization

Fig. 6.1 shows a schematic of the experimental setup used to measure the beam divergence of the atomic beam. An approximately 5 mm diameter diagnostic probe laser beam with 18 mW pump and 0.7 mW repump was introduced perpendicular to the direction of the atomic beam and retroreflected. The purpose of the retroreflection is to decrease the deflection of the atomic beam by the probe laser. A camera (PixeLink PL-B741EF) was placed perpendicular to both the diagnostic laser beam and the atomic beam. This camera recorded the atomic beam fluorescence and an image of the background scattered light with no atomic beam present. The two images were subtracted using python code and an example result is shown in Fig. 6.2. A lens in a lens tube was attached to the camera to focus at roughly the intersection of the laser beam and the atomic beam, and to reduce stray light. A slice of the subtracted images taken going through the atomic cloud was fit to a gaussian,  $ae^{-\frac{((x-u)/w)^2}{2}}$ , giving  $w = 133$  pixels. The diameter of the atomic beam is  $2w = 266$  pixels. Based on taking a camera picture of an object of a known size, a 10 mm width corresponds to 372 pixels. This gives an atomic beam size of  $\approx 7$  mm in diameter at the place where the fluorescence picture was taken. The distance from the entrance of the differential pumping section to where the fluorescence picture was taken is 258 mm. This gives a full angle divergence of 28 mrad. The distance from the tube entrance to the 3D MOT center is 55 cm so that the atomic beam size at the 3D MOT is approximately 15 mm in diameter. The size of the probe beam is not critical, as long as it is not so small that it does not intersect the atomic beam fully. Ideally the probe beam would have been a

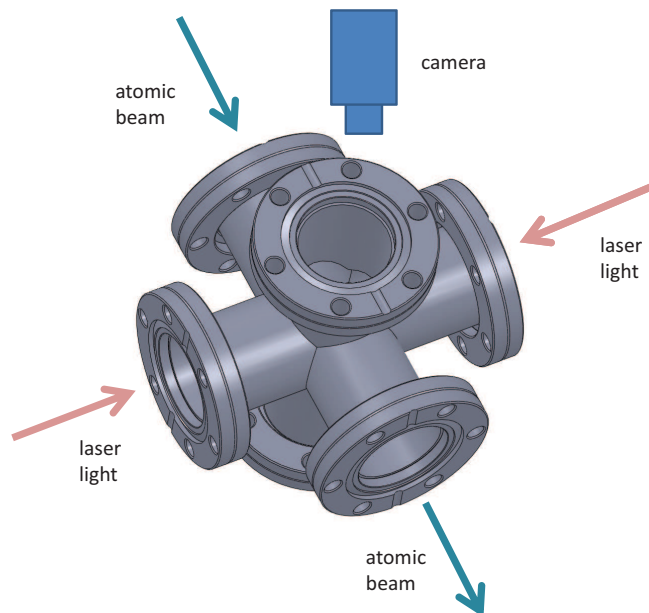


Figure 6.1: The setup used to measure the atomic beam divergence. Resonant laser light (pump and repump) was incident on the atomic beam perpendicular to the atomic beam motion. The laser beam was retroreflected. A picture with a camera was taken with and without the atomic beam present.

thin sheet that intersects the atomic beam in a narrow slice. It is noted that the probe beam intensity used here is larger than the saturation intensity. That is not expected to have an effect on the beam width measurements because even if all the atoms are saturated there is still more fluorescence in a region of space where the atomic density is higher.

## 6.2 Atomic speed distribution characterization

To measure the speed distribution coming from the 2D MOT we used the 3D MOT as a diagnostic tool. The fluorescence of the trapped atoms in the 3D MOT was recorded as a function of the time after the 2D MOT was

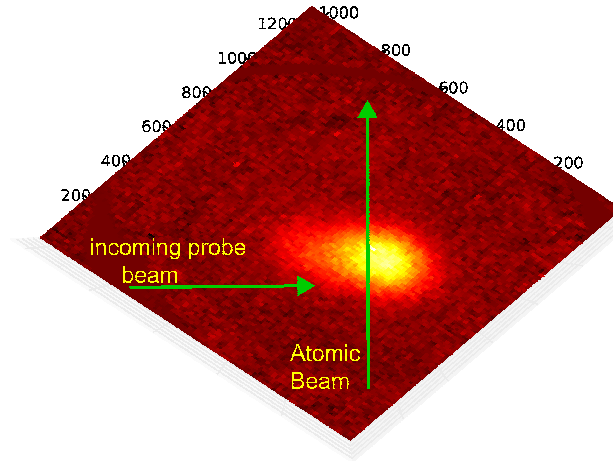


Figure 6.2: A fluorescence image of the Rb beam. The result of subtracting pictures taken with a camera as shown in Fig. 6.1, with and without the atomic beam present. A portion of the atomic beam is shown. The direction of travel of the atomic beam and the probe laser beam are labelled. Though not visible in the image shown, the center of the beam seemed to be pushed to the side slightly with reference to the viewport that the camera was looking through. This could be due to the push beam being aligned off center of the viewport and also possibly due to the camera perspective being at an angle with respect to the viewport.

turned on and the atomic beam established. The 2D MOT was turned on by energizing the 2D magnetic field coils with the 2D MOT light already on. The 3D MOT light and magnetic field were already on when the 2D MOT was turned on. Fig. 6.3 shows the resulting 3D MOT fluorescence data. The voltage on the photodiode from the fluorescence of the atoms trapped in the 3D MOT, as already given in Eq. 3.1, is

$$V(t) = \alpha \gamma_{sc} N. \quad (6.1)$$

As also given in Eq. 1.5 we have that the number of atoms in a 3D MOT,  $N(t)$ , from initial loading follows

$$\frac{dN}{dt} = R - \Gamma N - \beta \int n^2(\vec{r}, t) d^3\vec{r} \quad (6.2)$$

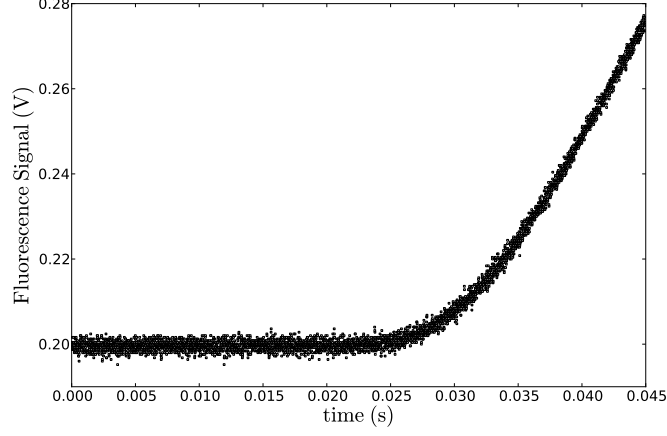


Figure 6.3: A plot of the 3D MOT fluorescence captured on a photodiode as a function of time from initial turn on of the 2D MOT. The 2D MOT was turned on with the 3D MOT light and magnetic field already on. The curvature gives information about the speed distribution of the atomic beam.

where  $\Gamma$  and  $\beta$  are loss rate constants due to background collisions and intra-trap collisions respectively. The density of the trapped atoms at position  $\vec{r}$  from the center of the trap at time  $t$  is  $n(\vec{r}, t)$ . For short times following initial loading of the 3D MOT the loss terms can be neglected since there are not many atoms accumulated yet, meaning both  $N$  and  $n(\vec{r}, t)$  are small. This means we can approximate

$$\frac{dN}{dt} \approx R. \quad (6.3)$$

Combining Eq. 6.3 with Eq. 6.1 we have

$$\frac{dV}{dt} = \alpha\gamma_{sc} \frac{dN}{dt} = \alpha\gamma_{sc}R. \quad (6.4)$$

This links a measurable quantity, the slope of the fluorescence voltage curve for small times from initial 3D MOT loading, to the loading rate,  $R$ .

The 3D MOT has some maximum capture speed,  $v_c$ , so that atoms travelling to the 3D MOT from the 2D MOT that are exceeding this speed will not be trapped. There is a distribution of speeds,  $f(v)$ , coming from

the 2D MOT. The loading rate,  $R$ , of the atoms into the trap will initially change as a function of time as atoms of different speeds arrive at the 3D MOT region. The curve in the fluorescence data shown in Fig. 6.3 relates to the speed distribution of the atomic beam arriving at the 3D MOT. If the speed probability distribution coming from the 2D MOT is  $f(v)$  then the loading rate as a function of time,  $t$ , from initial turn on of the 2D MOT will follow

$$R(t) = \phi \int_{d/t}^{v_c} f(v) dv. \quad (6.5)$$

In Eq. 6.5,  $d$  is the distance from the exit tube of the 2D MOT to the 3D MOT capture region, and  $t \geq (t_c = d/v_c)$ . The total number per second from the 2D MOT is  $\phi$ . When the curve in Fig. 6.3 becomes linear then

$$R_{\max} \approx \phi \int_0^{v_c} f(v) dv \quad (6.6)$$

meaning that the majority of all speed classes have reached the 3D MOT region from initial turn on of the 2D MOT.

To determine the shape of  $f(v)$  a few mathematical rearrangements are needed. First the derivative of  $R(t)$  from Eq. 6.5 is taken giving

$$\frac{dR(t)}{dt} = \phi f(d/t) \left( \frac{d}{t^2} \right). \quad (6.7)$$

Next  $\frac{dR(t)}{dt}$  is obtained from Eq. 6.4 and inserted into Eq. 6.7 giving

$$\frac{1}{\alpha \gamma_{sc}} \frac{d^2 V}{dt^2} = \phi f(d/t) \frac{d}{t^2}. \quad (6.8)$$

Now we divide both sides by  $R_{\max}$  given in Eq. 6.6

$$\frac{1}{R_{\max} \alpha \gamma_{sc}} \frac{d^2 V}{dt^2} = \frac{f(d/t) \frac{d}{t^2}}{\int_0^{v_c} f(v) dv} \quad (6.9)$$

Finally we apply Eq. 6.4 again to write  $R_{\max}$  in terms of voltage giving

$$\frac{1}{\left( \frac{dV}{dt} \right)_{\max}} \frac{d^2 V}{dt^2} = \frac{f(d/t) \frac{d}{t^2}}{\int_0^{v_c} f(v) dv} \quad (6.10)$$

Solving for  $f(d/t)$  gives

$$f(d/t) = \frac{V''}{V'_{\max}} \frac{t^2}{d} \int_0^{v_c} f(v) dv \quad (6.11)$$

where the prime indicates differentiation with respect to time and the integral involving  $f(v)$  is a constant.

The goal now is to extract the speed probability distribution,  $f(v)$ , from the data shown in Fig. 6.3. A python script was used to numerically extract the second derivative,  $V''$ , and the maximum slope,  $V'_{\max}$ , from the 3D MOT fluorescence data as a function of time from the 2D MOT turn on. The method used in the python script was to fit the 3D MOT fluorescence data shown in Fig. 6.3 to a line over a time interval of 0.007 s starting at  $t=0$ . The time interval was then shifted by 300  $\mu\text{s}$  and then the 3D MOT fluorescence data was fit again. The slope of the linear fits was recorded and assigned a time at the center of each interval. This provided the first derivative,  $V'$ , of the 3D MOT fluorescence data. The second derivative,  $V''$ , was obtained by repeating this procedure on the first derivative results. A plot of  $\frac{V''}{V'_{\max}} \frac{t^2}{d}$  versus speed  $v = d/t$  is given in Fig. 6.4. The cutoff in the plot at low velocities is due to the fact that for the data shown in Fig. 6.3 times only up to  $t = 0.06$  s were used (not shown in that figure). After this time the atom number is sufficiently large that the approximation used in Eq. 6.3 is no longer valid.

Looking at Fig. 6.3 the 3D MOT fluorescence starts to rise approximately at 0.021 sec from initial turn on of the 2D MOT. The distance from the entrance of the differential pumping tube on the 2D MOT side to the 3D MOT center is 55 cm. This gives an approximate capture speed,  $v_c$ , of the 3D MOT as 26 m/s. From Fig. 6.4 one can see the bulk of the speed probability distribution of the atomic beam lies below 26 m/s so that we approximate  $\int_0^{v_c} f(v) dv \approx 1$ . With this approximation Eq. 6.6 gives  $R_{\max} \approx \phi$ . Using  $R_{\max} = \frac{1}{\alpha\gamma_{\text{scat}}} \left(\frac{dV}{dt}\right)_{\max} \approx \phi$  we can find an approximate value for  $\phi$ . The maximum slope  $\left(\frac{dV}{dt}\right)_{\max}$  was taken as the slope in the linear portion of the 3D MOT fluorescence data. The coefficient  $\alpha$  can be given as

$$\alpha = \frac{(r_{\text{lens}})^2}{4(d_{\text{MOT}})^2} \eta \frac{hc}{\lambda} \epsilon. \quad (6.12)$$

The first part of the expression for  $\alpha$  gives the fraction of the total solid angle collected by a plano-convex lens of focal length 60 mm with radius,  $r_{\text{lens}}$ , placed a distance  $d_{\text{MOT}}$  from the 3D MOT. The power to voltage conversion factor of the photodiode is  $\eta$  and  $\frac{hc}{\lambda}$  is the energy of a fluoresced photon.  $\epsilon$  describes the transmitted fraction of photons as the fluorescent light travels through the cell once. In our case  $r_{\text{lens}} = 11.5$  mm,  $d_{\text{MOT}} = 14.5$  cm,  $\eta = 4.68\text{V}/\mu\text{W}$ , and  $\epsilon = \sqrt{11.2/11.5}$ . The  $\epsilon$  was determined by measuring one of the 3D MOT incoming beams as having 11.5 mW power

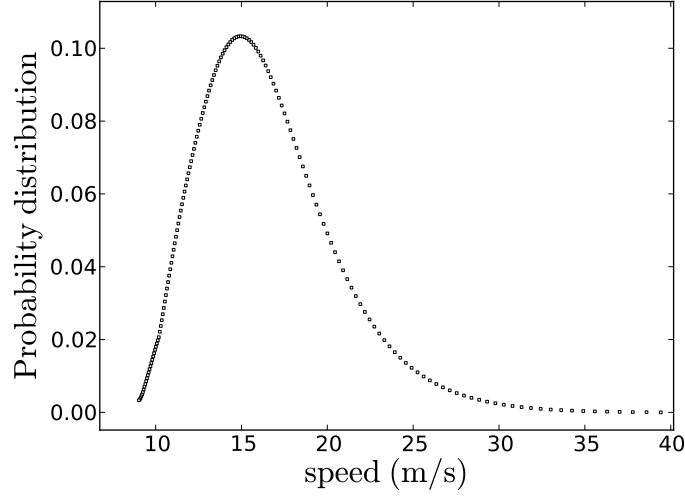


Figure 6.4: The speed distribution of atoms in the atomic beam from the 2D MOT that is capturable by the 3D MOT. This distribution is extracted from the fluorescence of the 3D MOT recorded from initial turn on of the 2D MOT.

before it entered the cell and having 11.2 mW power after it exited the cell after passing through two sides of the cell. This gives  $11.5\epsilon^2 = 11.2$ .

The scattering rate (number of photons emitted per atom per second) can be expressed as

$$\gamma_{\text{sc}} = \frac{\Gamma}{2} \left( \frac{s}{1 + s + \left(\frac{2\delta}{\Gamma}\right)^2} \right) \quad (6.13)$$

where  $\delta$  is the detuning of the MOT pump light from resonance which for our experiment was 12 MHz.  $\Gamma$  is the natural line width of the pump transition [23] which is  $2\pi \times 6.07$  MHz. The parameter  $s = \frac{I}{I_{\text{sat}}}$  where  $I$  is the total intensity of the MOT pump beams and  $I_{\text{sat}}$  is the saturation intensity of the pump transition which is  $3.9 \text{ mW/cm}^2$  [23]. In the pressure sensor experiment, with each of the three arms having 18 mW initially travelling to the cell and getting retroreflected, the total pump power in the MOT is  $P_{\text{tot}} = 3(18 \times \epsilon) + 3(18 \times \epsilon^3)$ . The intensity is taken as  $I = \frac{P_{\text{tot}}}{A}$  with  $A = \pi r_{\text{MOT}}^2$ , where  $r_{\text{MOT}}$  is the radius of the MOT pump beams. For our experiment the 3D MOT beams were roughly 23 mm in diameter.

Combining our values for  $\alpha$  and  $\gamma_{sc}$  gives  $\alpha\gamma_{sc} = 2.9 \times 10^{-8}$  V. The value of  $(\frac{dV}{dt})_{\max} = 6.13$  so that  $R_{\max} \approx \phi = 2 \times 10^8$  atoms/s total comes from the 2D MOT beam. This number could be increased, for example, by making the 2D MOT beams larger in diameter [93, 95]. The speed distribution data in this section was taken with  $^{85}\text{Rb}$  but similar results were obtained with  $^{87}\text{Rb}$ .

The speed distribution measured here is only for speeds capturable by our 3D MOT. Schoser et al. [93] measured the total speed distribution from their 2D MOT with and without a push beam. Without a push beam their speed distribution was quite broad, peaking around 50 m/s and extending to around 200m/s. The peak of the distribution and the total flux was shown to depend on factors such as the volume of the 2D MOT cooling region, the power and detuning of the 2D pump light, and the pressure of the Rb gas. The speed distribution from the 2D MOT is not a Maxwell-Boltzmann distribution. They showed that the presence of a push beam added a narrow and tall peak to the broad velocity distribution, centered at around 20 m/s. The peak position due to the push beam depended on the push power and detuning. For our speed distribution measurement, we are likely only seeing the narrow distribution due to the push beam because we are only detecting speeds lower than the capture velocity of the 3D MOT.

## Chapter 7

# Loss rate measurements in a 3D MOT

This chapter describes two experiments where the loss rate  $\Gamma$  due to background collisions was measured in a MOT as pressure in the 3D MOT chamber varied. The first experiment was when the residual background pressure was varied and the second was when Ar was introduced into the system.

### 7.1 Loss rate variation with the total pressure of residual background gas

Pressure measurements were taken with the Stabil-Ion gauge installed on our apparatus as the pressure varied due to outgassing of a residual gas analyzer (RGA 200, Stanford Research Systems) installed on the bakeout system which was connected to our apparatus. When the SRS RGA was turned on it caused the pressure to rise significantly. With the UHV pumps closed off the base pressure was around  $1 \times 10^{-6}$  Pa ( $1 \times 10^{-8}$  Torr). When the RGA was turned on from the bakeout station the pressure rose to around  $2.7 \times 10^{-5}$  Pa ( $2 \times 10^{-7}$  Torr) and over the period of 5 hours dropped to  $6.0 \times 10^{-6}$  Pa ( $4.5 \times 10^{-8}$  Torr). The SRS RGA was then shut off and the system pressure decreased down to the  $1 \times 10^{-6}$  Pa ( $1 \times 10^{-8}$  Torr) range after another 3 hours.

As the pressure in the system was varying loading curves of the 3D MOT were recorded. The loading curves were recorded by turning off the 3D MOT magnetic field and then turning it back on. With the 3D MOT light on at all times, the 3D MOT would start to fill again when the 3D MOT coils were turned back on. The fluorescence was captured onto a photodetector in the same way as described in section 3.2.1. The loading curve voltage was fit to  $V(t) = A(1 - e^{-\Gamma t}) + B$ . Fig. 7.1 shows an example loading curve taken with the fit superimposed. The coefficient  $A = \alpha\gamma_{\text{scat}}\frac{R}{\Gamma}$  converts the steady state atom number  $\frac{R}{\Gamma}$  to a steady state voltage. The coefficient  $B$  accounts for any offsets which commonly occur in experimental data due to,

for example, scattered laser light and background light in the room. Fig. 7.2

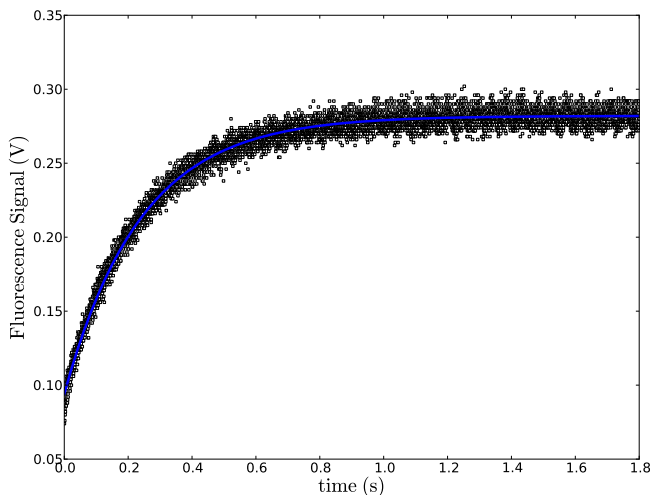


Figure 7.1: An example loading curve taken with a 3D magneto-optical trap at a residual background pressure of  $1.79 \times 10^{-5}$  Pa ( $1.34 \times 10^{-7}$  Torr). The y axis is the fluorescence signal captured on a photodiode as a function of time from initial 3D MOT turn on. The curve is fit to  $V(t) = A(1 - e^{-\Gamma t}) + B$  to extract  $\Gamma$ , which in this case gave  $\Gamma = 4.17 \pm 0.01 \text{ s}^{-1}$  as the fit result.

shows a plot of  $\Gamma$  versus pressure from fitting the loading curves taken while the pressure varied.

Arpornthip et al. [46] performed semi-classical calculations for the slope of  $\Gamma$  versus  $P$  for a 1K trap of Rb atoms and various background gases at a temperature of 300K. The results were  $2.0 \times 10^5 \text{ Pa}^{-1} \text{ s}^{-1}$  or  $2.6 \times 10^7 \text{ Torr}^{-1} \text{ s}^{-1}$  for  $\text{N}_2$  and for  $\text{CO}_2$  while  $\text{H}_2$  was  $3.7 \times 10^5 \text{ Pa}^{-1} \text{ s}^{-1}$  or  $4.9 \times 10^7 \text{ Torr}^{-1} \text{ s}^{-1}$ . RGA scans taken with the Pfeiffer RGA installed on our apparatus showed that when the SRS RGA was first turned on the dominant species were  $\text{N}_2$  or  $\text{CO}$ ,  $\text{CO}_2$  and  $\text{H}_2$ . As the pressure decreased  $\text{H}_2$  became the dominant species. This means as the background pressure decreased in our system and hydrogen became the dominant species the slope of  $\Gamma$  versus pressure  $P$  became steeper. Fitting the low pressure data to a line gives a slope of  $2.5 \times 10^5 \text{ Pa}^{-1} \text{ s}^{-1}$  ( $3.4 \times 10^7 \text{ Torr}^{-1} \text{ s}^{-1}$ ) and for the higher pressure data the slope was  $1.7 \times 10^5 \text{ Pa}^{-1} \text{ s}^{-1}$  ( $2.3 \times 10^7 \text{ Torr}^{-1} \text{ s}^{-1}$ ) which is

reasonable compared to the slopes calculated by Arpornthip et al. mentioned above. Comparing their calculation of the velocity averaged collisional loss cross section to ours for a temperature of 295K background gas and a  $C_6$  value of 336.4 a.u. [44] gives a difference of at most 5 percent in the range of trap depths from 1 to 2 K.

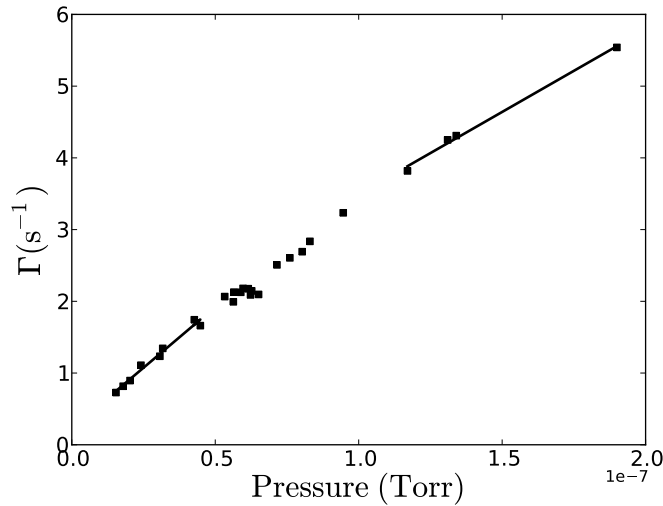


Figure 7.2: The loss rate constant,  $\Gamma$ , due to background collisions versus total background pressure. The pressure increased after a residual gas analyzer was turned on and then decreased. As the pressure decreased loading curves of the 3D MOT were taken. The loading curves (photodiode fluorescence) were fit to  $V(t) = A(1 - e^{-\Gamma t}) + B$  to extract  $\Gamma$ .

## 7.2 Loss rate variation with the pressure of Ar background gas

The loss rate constant,  $\Gamma$ , due to background collisions was measured for various Ar pressures. While the 3D MOT conditions were on, the 2D pump light and push light were turned off and the push shutter was closed. The atom number in the 3D MOT then decayed exponentially and a fluorescence signal of the 3D MOT was recorded using a photodiode. The fluorescence voltage signal was fit to extract  $\Gamma$ . Fig. 7.3 shows an example of the data

taken at a total pressure of  $2.1 \times 10^{-5}$  Pa ( $1.61 \times 10^{-7}$  Torr). The data was fit from a time of 30 ms after initial turn off of the 2D MOT to account for the time needed for the atomic beam to stop travelling to the 3D MOT. A

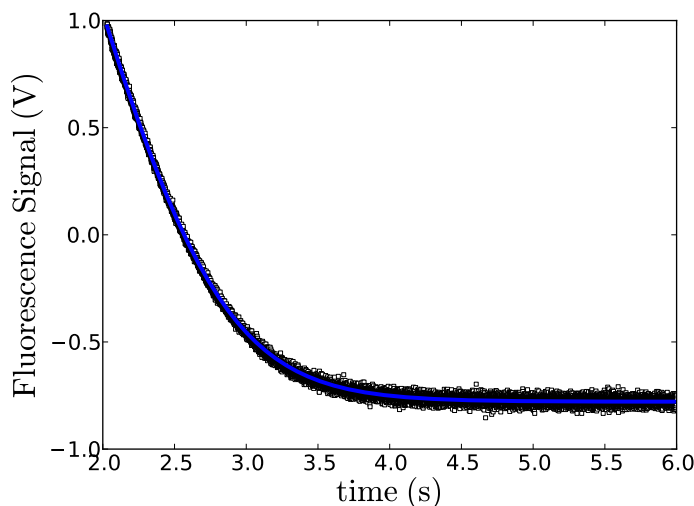


Figure 7.3: An example decay curve taken with the 3D MOT after the 2D MOT had been turned off. The total pressure of the system with Ar present in this case was  $2.1 \times 10^{-5}$  Pa ( $1.61 \times 10^{-7}$  Torr). The curve was fit to a decaying exponential and the loss rate constant  $\Gamma$  determined for this case to be  $2.60 \text{ s}^{-1}$ .

decay curve was used to determine the loss rate constant,  $\Gamma$ , rather than a loading curve. This is to avoid the loss mechanism of the 2D MOT beam itself colliding with the trapped atoms and causing loss.

The total pressure in the system as Ar was added was measured using the Stabil-Ion gauge installed on the apparatus. The background pressure before Ar was added was  $3.95 \times 10^{-7}$  Pa ( $2.97 \times 10^{-9}$  Torr). Ar was added through a leak valve installed on the bakeout station which was connected to the apparatus. The original leak valve on the apparatus failed and needs replacing. The ion gauge and SRS RGA on the bakeout station were turned off during measurement. The Pfeiffer RGA on our apparatus generally increases the residual background pressure by 1.5 to 2 times so it was also turned off to keep the residual background pressure as low as possible. The measurements of  $\Gamma$  in the 3D MOT as a function of Ar pressure are shown

in Fig. 7.4 on a log-log plot. At each Ar pressure, five decay traces were taken at each pressure and averaged and then fit. The loss rate constant  $\Gamma$  versus the pressure of Ar was fit to a line and the slope extracted giving a velocity averaged collisional loss cross section of  $0.634 \times 10^{-9} \text{ cm}^3/\text{s}$ . Victor Barua is credited with developing the software system that made taking the measurements displayed in Fig. 7.4 possible. Adrian Cavailles wrote the original code to take this data. Both helped make the gas manifold to add gases into the system, and also optimized and improved the performance of the magneto-optical traps.

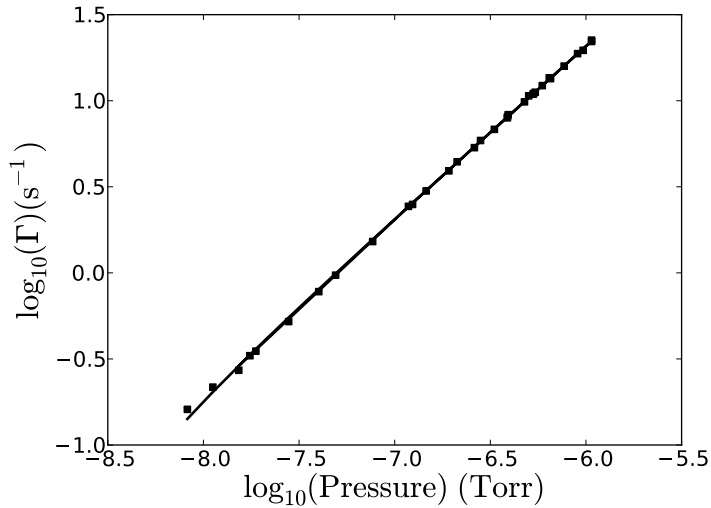


Figure 7.4: Measurements of loss rate constant,  $\Gamma$ , in a MOT at various Ar pressures. The Ar pressure was measured with an ion gauge.

The velocity averaged collisional loss cross section, from the measurement of  $\Gamma$  vs  $P_{\text{Ar}}$  described here, corresponds to a trap depth of approximately 2.95 K for the 3D MOT in its present setup. This is based on calculation of the velocity averaged collisional loss cross section as a function of trap depth. The capture speed,  $v_c$ , of 26 m/s given in section 6.2 can also be used for a rough estimate of trap depth measurement. The trap depth is given by  $\frac{1}{2}mv_e^2$ , where  $v_e$  is the escape speed. The capture speed will be larger than the escape speed because the effective length over which an atom can be slowed down is the whole diameter of the laser beams. To

escape, the atoms start off at the middle of the laser beams and only have to travel the radius of the laser beams. For an estimate of the relationship between  $v_c$  and  $v_e$ , the kinetic energy for escape (or trap depth) can be expressed as  $\frac{1}{2}mv_e^2 = Fr$  where  $F$  is the average force on an atom over the radius  $r$  of the beam. The maximum kinetic energy that an atom entering into the 3D MOT can have and be trapped can similarly be expressed as  $\frac{1}{2}mv_c^2 = F(2r)$ . Taking the ratio of these two expressions gives  $v_c = \sqrt{2}v_e$ . For  $v_c = 26$  m/s, a trap depth of 1.8 K is predicted along the radial direction of the 3D MOT (the atomic beam axis direction). The MOT trap depth is anisotropic and was found to be approximately double along the axial direction [53]. This gives an estimate of the average trap depth of our 3D MOT to be  $(1.8 + 1.8 + 2 \times 1.8)/3 = 2.4$  K. This is in reasonable agreement with the trap depth estimate based on calculation given above as a rough estimate of trap depth.

## Chapter 8

# Future outlook and conclusions

### 8.1 Future outlook

So far the work on the atom pressure sensor has shown that the 2D MOT is operational and that a 3D MOT can be loaded from it. Preliminary data of the dependence of the loss rate constant,  $\Gamma$ , with argon pressure has been measured with a 3D MOT. An ion gauge was used to measure the argon pressure. Further experimental goals are to trap atoms in a magnetic trap, introduce gases into the system, and take measurements of pressure with the trapped atoms. These pressure measurements would be compared with pressure readings from commercial gauges and calibrated gauges sent from the National Institute of Standards and Technology.

#### 8.1.1 Magnetic trapping coils

The same magnetic coils used for the 3D MOT of the pressure sensor apparatus will be used for magnetic trapping. The 3D MOT coils currently in place do not provide a gradient deep enough for magnetic trapping of atoms from the 3D MOT. To perform pressure measurements using the loss rate in a magnetic trap, another set of coils have been made from PVC coated hollow core copper tubing. The hollow core allows water to be run through the tubing for cooling.

The replacement coils have 8 axial windings and 8 radial windings. They are constructed from quarter inch outer diameter copper tubing with a quoted 0.03 inch wall thickness and a 0.032 inch thick PVC coating. The measured outer diameter of the copper tubing including the PVC is approximately 8.3 mm and the inner hollow core is 4.5 mm. The coil has a 188 mm outer diameter and 38 mm inner diameter. The height of each coil is 73 mm. The coil windings are secured by wrapping fiber glass tape around the cross section (see Fig. 8.1). The PVC coating is so that the coil windings do not short on each other. The tubing is from Alaskan Copper (part number

142797). The coils will be driven using a 60 V, 250 A power supply. The resistance of each coil is 38.5 m $\Omega$ .

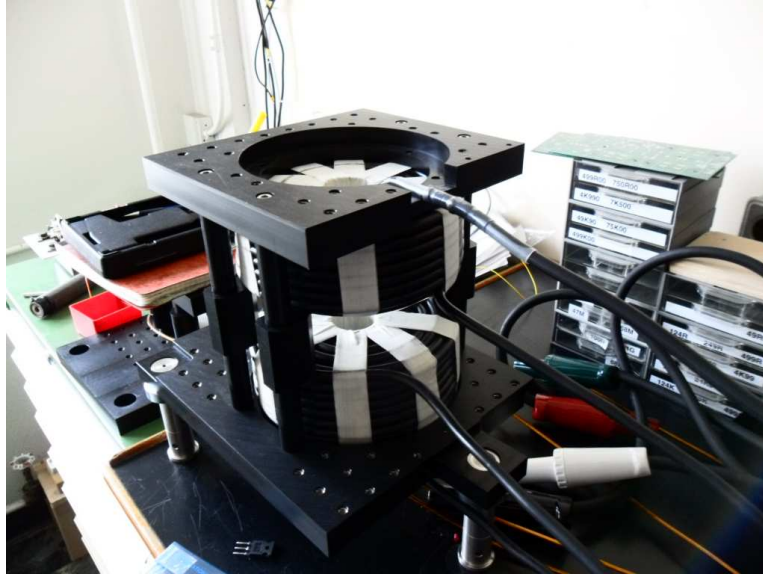


Figure 8.1: The new magnetic coils and mount for the 3D MOT and magnetic trap of the atom pressure sensor experiment.

Running water at 70-80 psi from the tap in parallel through the coils gave a flow rate of 36 seconds per litre for one coil and 29 seconds per litre for the other. At 230 A, the temperature of the water exiting the coils was 28°C . The incoming water temperature was 11°C . Ref. [97] was invaluable for designing magnetic coils using water cooled hollow core tubing. The coils will be mounted by sandwiching them in between delrin plates with the top coil sitting on spacers in between the two coils (see Fig. 8.1).

The predicted magnetic field gradient is approximately 0.57 G/cm ( $5.7 \times 10^{-5}$  T/cm) per A radially which would lead to a maximum radial magnetic field gradient of 125 G/cm ( $1.25 \times 10^{-2}$  T/cm) at 250 A. From the center of the cell, where the magnetic field zero is located, to the outer edge of the cell is 2 cm. The maximum magnetic field occurring radially at the edge of the cell would then be 250 G . The trap depth, as given in section 1.2.2, can be estimated as  $\Delta E = g_F m_F \mu_B B$  for the  $m_F = -1$ ,  $F = 1$  , level of the  $5^2S_{1/2}$  ground state for  $^{87}\text{Rb}$ . Using  $g_F = -1/2$  and  $\mu_B = 9.274 \times 10^{-24}$  J/T from [21] and  $B = 250$  G this gives a maximum radial trap depth of around

8 mK. The measured coil gradient in anti-helmholtz configuration is 0.58 G/cm ( $5.8 \times 10^{-5}$  T/cm) per A along the radial direction and approximately double along the axial direction.

To trap atoms in a magnetic trap, coils for magnetic trapping and the supporting infrastructure such as breadboards, mounts, electrical and water connections, must be installed.

### 8.1.2 NIST gauges

Towards the completion of this writing the NIST gauges arrived and have been installed on the apparatus. This required removing Rb D in Fig. 5.1 and installing the gauges, as in Fig. 8.2. NIST sent two spinning rotary gauges (MKS SRG-2), labelled SRG2 and SRG3 in Fig. 5.1, and one ion gauge (370 Stabil Ion), labelled IG2 in Fig. 5.1.

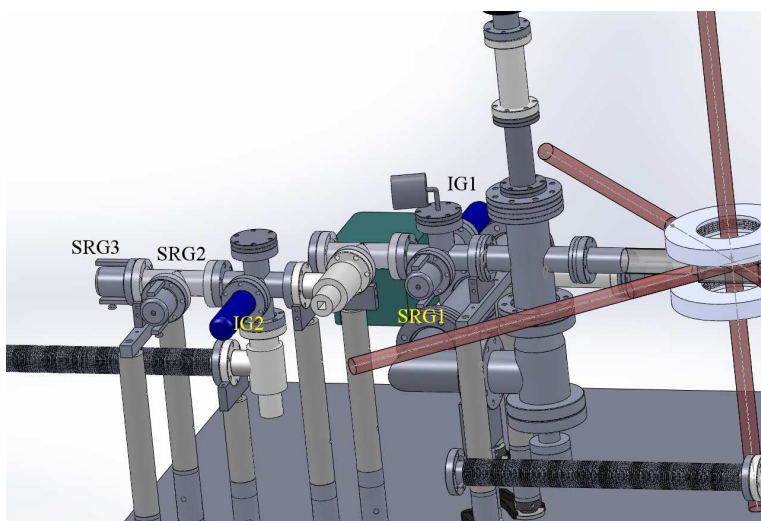


Figure 8.2: The experimental apparatus with the NIST gauges installed. Two spinning rotary gauges (labelled SRG3 and SRG2) and one ion gauge (labelled IG2) were added to the system. They will be calibrated using our apparatus with trapped Rb atoms and then shipped back to NIST and recalibrated on their orifice flow standard. Our spinning rotary gauge and ion gauge are labelled SRG1 and IG1, respectively.

### 8.1.3 Technical challenges

A leak valve is used to introduce the gas into the apparatus. For the leak valve used in the flowmeter at NIST a wait time of approximately 5 hours is given once setting the leak valve to allow creep to settle [77]. If the pressure is changing during measurement that would add error to the pressure measurement using trapped atoms. This becomes more of an issue at low pressures ( $< 10^{-7}$  Pa or  $10^{-9}$  Torr) where the decay time  $\tau = 1/\Gamma$  is greater than 10 s. The time to take multiple sets of pressure measurements with the magnetic trap would take around 20 min.

Another difficulty may be the presence of pressure gradients in the apparatus so that the pressure at the gauges is different than at the atoms. An attempt has been made to minimize this by being able to valve off any pumps which may cause pressure gradients and by situating the gauges as close to the region where the atoms are trapped as possible. The gauge readings with and without pumps present will give an indication of the contribution of a pressure differential due to pumping. The distance between the NIST ion gauge and our ion gauge installed on our apparatus is approximately the same distance between our ion gauge and the trapped atom location. This should be incorporated into the calibration of the ion gauges with the trapped atoms. We could also explore taking measurements with all the pumps closed off to decrease pressure gradients. This would be possible as long as the residual background gas is significantly smaller than the pressure of Ar to be measured.

## 8.2 Conclusions

This thesis started with a brief description of magneto-optical trapping and magnetic traps. These traps are the tools we used to prepare and study samples of ultra cold atoms. A key parameter of interest for these traps is the loss rate constant due to background collisions,  $\Gamma$ . The loss rate constant was related to the density of the background gas species. This relation involves the velocity averaged collisional loss cross section between the trapped atoms and the different background species. Quantum scattering calculations for the loss cross section were described and performed earlier in our group. The loss cross section depends on the trap depth and experimental verification of this dependence was shown previously for trap depths attainable with the magnetic trap used (up to 10 mK). This work provided verification for trap depths for a MOT ( $\approx 1$ K). For this verification, a measurement of trap depth adapted from Hoffmann et al. [16] using photoassociative loss was

used. The dependence of the velocity averaged collisional loss cross section on trap depth can be applied to trap depth measurements. This is desirable because trap depth is a difficult parameter to determine, especially for a MOT. Laser beam imperfections in shape, polarization, and alignment, as well as the presence of interference fringes prevent accurate calculation of MOT trap depth. The ‘catalysis’ method described in this work to measure trap depth requires specialized equipment such as tunable lasers and is quite involved. Another application proposed in this work is density measurement of a background gas species based on measurements of  $\Gamma$  for an atomic trap and calculation of the velocity averaged collisional loss cross section.

Part of the apparatus for the pressure sensor experiment was designed, assembled, baked out, and a 2D MOT was shown to be operational. Future directions are to get a magnetic trap working and to make pressure measurements comparing these measurements with commercial gauges and gauges sent from NIST. The pressure sensor experiment is important because it may allow a standard for pressure using ultracold atoms which has several benefits over existing standards. Those benefits are the possibility of not needing pressure gauges calibrated on a higher pressure standard, reproducibility of standards from lab to lab, and a possibly simpler and more portable experimental setup. In addition the proposed technique may be able to perform differential pressure measurement and measurement of pressure for gases that are currently not used in existing standards.

# Bibliography

- [1] J Blicek, X Flchard, A Cassimi, H Gilles, S Girard, and D Hennecart. A new motrims apparatus for high resolution measurements in ion-atom collisions and trapped atoms studies. *Journal of Physics: Conference Series*, 163(1):012070, 2009.
- [2] Andrew T. Grier, Marko Cetina, Fedja Oručević, and Vladan Vuletić. Observation of cold collisions between trapped ions and trapped atoms. *Phys. Rev. Lett.*, 102:223201, Jun 2009.
- [3] Christoph Zipkes, Stefan Palzer, Lothar Ratschbacher, Carlo Sias, and Michael Köhl. Cold heteronuclear atom-ion collisions. *Phys. Rev. Lett.*, 105:133201, Sep 2010.
- [4] R. S. Schappe, T. Walker, L. W. Anderson, and Chun C. Lin. Absolute electron-impact ionization cross section measurements using a magneto-optical trap. *Phys. Rev. Lett.*, 76:4328–4331, Jun 1996.
- [5] P Würtz, T Gericke, A Vogler, and H Ott. Ultracold atoms as a target: absolute scattering cross-section measurements. *New Journal of Physics*, 12(6):065033, 2010.
- [6] K. J. Matherson, R. D. Glover, D. E. Laban, and R. T. Sang. Absolute metastable atom-atom collision cross section measurements using a magneto-optical trap. *Review of Scientific Instruments*, 78(7):–, 2007.
- [7] K. J. Matherson, R. D. Glover, D. E. Laban, and R. T. Sang. Measurement of low-energy total absolute atomic collision cross sections with the metastable  $^3P_2$  state of neon using a magneto-optical trap. *Phys. Rev. A*, 78:042712, Oct 2008.
- [8] R D Glover, D E Laban, K J Matherson, W Wallace, and R T Sang. Experimental investigation of atomic collisions in time scales varying from nanosecond to microseconds. *Journal of Physics: Conference Series*, 212(1):012013, 2010.

## Bibliography

---

- [9] T. V. Tscherbul, Z. Pavlovic, H. R. Sadeghpour, R. Côté, and A. Dalgarno. Collisions of trapped molecules with slow beams. *Phys. Rev. A*, 82:022704, Aug 2010.
- [10] Brian C. Sawyer, Benjamin K. Stuhl, Dajun Wang, Mark Yeo, and Jun Ye. Molecular beam collisions with a magnetically trapped target. *Phys. Rev. Lett.*, 101:203203, Nov 2008.
- [11] B. J. Claessens, J. P. Ashmore, R. T. Sang, W. R. MacGillivray, H. C. W. Beijerinck, and E. J. D. Vredenburg. Measurement of the photoionization cross section of the  $(2p)^5(3p) \ ^3D_3$  state of neon. *Phys. Rev. A*, 73:012706, Jan 2006.
- [12] K.-A. Brickman, M.-S. Chang, M. Acton, A. Chew, D. Matsukevich, P. C. Haljan, V. S. Bagnato, and C. Monroe. Magneto-optical trapping of cadmium. *Phys. Rev. A*, 76:043411, Oct 2007.
- [13] D N Madsen and J W Thomsen. Measurement of absolute photoionization cross sections using magnesium magneto-optical traps. *Journal of Physics B: Atomic, Molecular and Optical Physics*, 35(9):2173, 2002.
- [14] David E. Fagnan, Jicheng Wang, Chenchong Zhu, Pavle Djuricanin, Bruce G. Klappauf, James L. Booth, and Kirk W. Madison. Observation of quantum diffractive collisions using shallow atomic traps. *Phys. Rev. A*, 80:022712, Aug 2009.
- [15] D. Fagnan. Study of collision cross section of ultra-cold rubidium using a magneto-optic and pure magnetic trap. Honours Thesis, University of British Columbia, 2009.
- [16] D. Hoffmann, S. Bali, and T. Walker. Trap-depth measurements using ultracold collisions. *Phys. Rev. A*, 54:R1030–R1033, Aug 1996.
- [17] J. Van Dongen, C. Zhu, D. Clement, G. Dufour, J. L. Booth, and K. W. Madison. Trap-depth determination from residual gas collisions. *Phys. Rev. A*, 84:022708, Aug 2011.
- [18] J. Weiner and P.-T. Ho. *Light-Matter Interaction*, volume 1. John Wiley and Sons, Inc., New Jersey, 2003.
- [19] H. J. Metcalf and P. van der Straten. *Laser Cooling and Trapping*. Springer-Verlag, New York, 1999.

## Bibliography

---

- [20] T. P. Meyrath. Electromagnet design basics for cold atom experiments. <http://george.ph.utexas.edu/~meyrath/informal/electromagnets.pdf>.
- [21] D. A. Steck. Rubidium 87 D line data. Available online at <http://steck.us/alkalidata> (revision 2.1.4), 2010.
- [22] A. Corney. *Atomic and Laser Spectroscopy*. Oxford University Press, Oxford, 1977.
- [23] D. A. Steck. Rubidium 85 D line data. Available online at <http://steck.us/alkalidata> (revision 2.1.6), 2013.
- [24] T. Bergeman, Gidon Erez, and Harold J. Metcalf. Magnetostatic trapping fields for neutral atoms. *Phys. Rev. A*, 35:1535–1546, Feb 1987.
- [25] S. Martellucci, A. N. Chester, A. Aspect, and M. Inguscio. *Bose-Einstein Condensates and Atom Lasers*. Springer Link, 2002.
- [26] John Weiner, Vanderlei S. Bagnato, Sergio Zilio, and Paul S. Julienne. Experiments and theory in cold and ultracold collisions. *Rev. Mod. Phys.*, 71:1–85, Jan 1999.
- [27] J. Weiner, V. S. Bagnato, S. Zilio, and P. S. Julienne. Experiments and theory in cold and ultracold collisions. *Rev. Mod. Phys.*, **71**, 1999.
- [28] B. L. Lev. *Magnetic Microtraps for Cavity QED, Bose-Einstein Condensates, and Atom Optics*. PhD thesis, California Institute of Technology, 2006.
- [29] K. Overstreet, P. Zabawa, J. Tallant, A. Schwettmann, and J. Shaffer. Multiple scattering and the density distribution of a Cs mot. *Opt. Express*, 13(24):9672–9682, Nov 2005.
- [30] G L Gattobigio, T Pohl, G Labeyrie, and R Kaiser. Scaling laws for large magneto-optical traps. *Physica Scripta*, 81(2):025301, 2010.
- [31] Frederick. H. Mies, W. Williams, P. S. Julienne, and M. Krauss. Estimating bounds on collisional relaxation rates of spin-polarized  $^{87}\text{Rb}$  atoms at ultracold temperatures. *J. Res. Natl. Inst. Stand. Technol.*, 101:521, Jul 1996.
- [32] A. M. Steane, M. Chowdhury, and C. J. Foot. Radiation force in the magneto-optical trap. *J. Opt. Soc. Am. B*, 9(12):2142–2158, Dec 1992.

## Bibliography

---

- [33] Carl Wieman, Gwenn Flowers, and Sarah Gilbert. Inexpensive laser cooling and trapping experiment for undergraduate laboratories. *American Journal of Physics*, 63(4):317–330, 1995.
- [34] L. D. Landau and E. M. Lifshitz. *Quantum Mechanics Non-Relativistic Theory*. Addison-Wesley Publishing Company Inc., Reading, Massachusetts, 1958.
- [35] D. E. Manolopoulos. Quantum scattering dynamics. Internal Publication.
- [36] L. S. Rodberg and R. M. Thaler. *Introduction to the Quantum Theory of Scattering*. Academic Press, New York, 1967.
- [37] R. L. Liboff. *Introductory Quantum Mechanics*. Addison-Wesley Publishing Company, Inc., second edition, 1992.
- [38] L. E. Ballentine. *Quantum Mechanics*. Prentice Hall, Englewood Cliffs, N.J., 1990.
- [39] B.R Johnson. The multichannel log-derivative method for scattering calculations. *Journal of Computational Physics*, 13(3):445 – 449, 1973.
- [40] Wikipedia. Lennard-Jones potential. Available online at [http://en.wikipedia.org/wiki/Lennard-Jones\\_potential](http://en.wikipedia.org/wiki/Lennard-Jones_potential), 2014.
- [41] F. Ercolessi. The Lennard-Jones potential. <http://www.fisica.uniud.it/ercolessi/md/md/node15.html>, 1997.
- [42] M. Fowler. Van der Waals forces between atoms. Internal Publication, 2007.
- [43] Andrei Derevianko, Sergey G. Porsev, and James F. Babb. Electric dipole polarizabilities at imaginary frequencies for hydrogen, the alkali metal, alkaline earth, and noble gas atoms. *Atomic Data and Nuclear Data Tables*, 96(3):323 – 331, 2010.
- [44] J. Mitroy and J.-Y. Zhang. Long-range dispersion interactions. ii. alkali metal and rare-gas atoms. *Phys. Rev. A*, 76:032706, Sep 2007.
- [45] A. Dalgarno and W.D. Davison. Long-range interactions of alkali metals. *Molecular Physics*, 13(5):479–486, 1967.

## Bibliography

---

- [46] T. Arpornthip, C. A. Sackett, and K. J. Hughes. Vacuum-pressure measurement using a magneto-optical trap. *Phys. Rev. A*, 85:033420, Mar 2012.
- [47] W. Kruithof. Laser trapping of sodium isotopes for a high-precision  $\beta$ -decay experiment. Ph.D. Thesis, University of Groningen, 2012.
- [48] M. S. Child. *Molecular Collision Theory*. Academic Press, London, 1974.
- [49] S. Bali, K. M. O'Hara, M. E. Gehm, S. R. Granade, and J. E. Thomas. Quantum-diffractive background gas collisions in atom-trap heating and loss. *Phys. Rev. A*, 60:R29–R32, Jul 1999.
- [50] S. Singh. Progress towards ultra-cold ensembles of rubidium and lithium. Master's thesis, University of British Columbia, 2007.
- [51] J. Van Dongen. Simultaneous cooling and trapping of  $^6\text{Li}$  and  $^{85/87}\text{Rb}$ . Master's thesis, University of British Columbia, 2007.
- [52] D. J. McCarron. A guide to acousto-optic modulators. Internal Publication, Durham Atomic and Molecular Physics. <http://massey.dur.ac.uk/resources/slcornish/AOMGuide.pdf>, 2007.
- [53] J. Kawanaka, K. Shimizu, H. Takuma, and F. Shimizu. Quadratic collisional loss rate of a  $^7\text{Li}$  trap. *Phys. Rev. A*, 48:R883–R885, Aug 1993.
- [54] L. Peksa, D. Pražák, T. Gronych, P. Řepa, M. Vičar, J. Tesař, Z. Krajčůček, and F. Staněk. Primary vacuum standard for uhv range - standing experience and present problems. *Mapan*, **24**, 77-88, 2009.
- [55] B.I.P.M (Bureau International des Poids et Mesures). International vocabulary of metrology - basic and general concepts and associated terms, 3rd ed. jcgM 200:2012. Internal publication, 2008.
- [56] MKS Instruments. MKS Baratron<sup>®</sup> types 615A/616A/617A high accuracy sensor heads manual. Internal Publication, 2009.
- [57] A. P. Müller. Measurement performance of capacitance diaphragm gages and alternative low-pressure transducers. Internal Publication, 1997.
- [58] MKS Instruments. MKS SRG-3 spinning rotor vacuum gauge instruction manual. Internal Publication, 2009.

## Bibliography

---

- [59] Sharrill Dittmann, Bernd E. Lindenau, and C. R. Tilford. The molecular drag gauge as a calibration standard. *Journal of Vacuum Science & Technology A: Vacuum, Surfaces, and Films*, 7(6):3356–3360, 1989.
- [60] Ren Fang Chang and Patrick J. Abbott. Factors affecting the reproducibility of the accommodation coefficient of the spinning rotor gauge. *Journal of Vacuum Science & Technology A: Vacuum, Surfaces, and Films*, 25(6):1567–1576, 2007.
- [61] G. F. Weston. *Ultrahigh Vacuum Practice*. Butterworth & Co. (Publishers) Ltd., United Kingdom, 1985.
- [62] Stanford Research Systems. Hot vs. cold ionization gauges. Internal Publication, 2008.
- [63] Detian Li and Karl Jousten. Comparison of the stability of hot and cold cathode ionization gauges. *Journal of Vacuum Science & Technology A*, 21(4):937–946, 2003.
- [64] Brooks Automation. Granville-Phillips series 370 Stabil-Ion<sup>®</sup> vacuum gauge and controller datasheet. Internal Publication, 2008.
- [65] J. F. O’Hanlon. *A user’s guide to vacuum technology, 2nd Ed.* John Wiley & Sons, 1989.
- [66] D. G. Bills. Causes of nonstability and nonreproducibility in widely used bayard–alpert ionization gauges. *Journal of Vacuum Science & Technology A: Vacuum, Surfaces, and Films*, 12(2):574–579, 1994.
- [67] Stanford Research Systems. Bayard-Alpert gauge filaments: Tungsten or thoria? Internal Publication, 2012.
- [68] James A. Fedchak and Dana R. Defibaugh. Long-term stability of metal-envelope enclosed bayardalpert ionization gauges. *Journal of Vacuum Science & Technology A*, 30(6), 2012.
- [69] Brooks Automation. Granville-Phillips series 370 Stabil-Ion<sup>®</sup> vacuum measurement controller instruction manual. Internal Publication, 2007.
- [70] Pfeiffer Vacuum. Prisma Plus<sup>TM</sup> QMG 220 operating instructions. Internal Publication, 2007.
- [71] K F Poulter. The calibration of vacuum gauges. *Journal of Physics E: Scientific Instruments*, 10(2):112, 1977.

- [72] D. Li, G. Zhao, M. Guo, J. Xu, and Y. Cheng. Static expansion vacuum standard with extended low pressure range. *Mapan*, **24**, 95-100, 2009.
- [73] Detian Li, Meiru Guo, Yongjun Cheng, Yan Feng, and Dixin Zhang. Vacuum-calibration apparatus with pressure down to  $10^{-10}$  Pa. *Journal of Vacuum Science & Technology A: Vacuum, Surfaces, and Films*, 28(5):1099–1104, 2010.
- [74] B. W. Rossiter and R. C. Baetzold. *Physical Methods of Chemistry, Second Edition, Volume Six: Determination of Thermodynamic Properties*. John Wiley & Sons Inc., 1992.
- [75] H. M. Akram, M. Maqsood, and H. Rashid. Techniques used for vacuum standardization. *World Applied Sciences Journal* 7(1): 76-85, 2009.
- [76] Li Detian, Cheng Yongjun, and Feng Yan. Extension of the range of a constant-conductance flowmeter by a flow divider. *Measurement Science and Technology*, 22(12):125405, 2011.
- [77] K. E. McCulloh, C. R. Tilford, C. D. Ehrlich, and F. G. Long. Low-range flowmeters for use with vacuum and leak standards. *Journal of Vacuum Science & Technology A: Vacuum, Surfaces, and Films*, 5(3):376–381, 1987.
- [78] James A. Fedchak and Dana R. Defibaugh. Accurate conductance measurements of a pinhole orifice using a constant-pressure flowmeter. *Measurement*, 45(10):2449 – 2451, 2012. Special Volume.
- [79] J. Fedchak. Private communication., 2014.
- [80] S. D. Gensemer, V. Sanchez-Villicana, K. Y. N. Tan, T. T. Grove, and P. L. Gould. Trap-loss collisions of  $^{85}\text{rb}$  and  $^{87}\text{rb}$  : Dependence on trap parameters. *Phys. Rev. A*, 56:4055–4063, Nov 1997.
- [81] Christopher D. Wallace, Timothy P. Dinneen, Kit-Yan N. Tan, Timothy T. Grove, and Phillip L. Gould. Isotopic difference in trap loss collisions of laser cooled rubidium atoms. *Phys. Rev. Lett.*, 69:897–900, Aug 1992.
- [82] C. Monroe, W. Swann, H. Robinson, and C. Wieman. Very cold trapped atoms in a vapor cell. *Phys. Rev. Lett.*, 65:1571–1574, Sep 1990.
- [83] B. Savernin, X. Baillin, E. Blanquet, I. Nuta, D. Saint Patrice, P. Nicolas, P.L. Charvet, and J.L. Pornin. New method to evaluate materials

- outgassing used in {MEMS} thin film packaging technology. *Microelectronic Engineering*, 107(0):97 – 100, 2013.
- [84] Ronald C. Johnson, Randy Tysinger, and Paul Arnold. Pressure measurement repeatability in high current ion implanters using hot cathode ionization gauge with design and operation optimized for stabilitya). *Journal of Vacuum Science & Technology A*, 22(5):2191–2194, 2004.
- [85] Kjell Knapas and Mikko Ritala. In situ studies on reaction mechanisms in atomic layer deposition. *Critical Reviews in Solid State and Materials Sciences*, 38(3):167–202, 2013.
- [86] Laurent Henn-Lecordier, Wei Lei, Mariano Anderle, and Gary W. Rubloff. Real-time sensing and metrology for atomic layer deposition processes and manufacturing. *Journal of Vacuum Science & Technology B*, 25(1):130–139, 2007.
- [87] Robert E. Ellefson. Methods for in situ QMS calibration for partial pressure and composition analysis. *Vacuum*, 101(0):423 – 432, 2014. Including rapid communications, original articles and a special section: Measurement Characteristics and Use of Quadrupole Mass Spectrometers for Vacuum Applications.
- [88] Jin-Peng Yuan, Zhong-Hua Ji, Yan-Ting Zhao, Xue-Fang Chang, Lian-Tuan Xiao, and Suo-Tang Jia. Simple, reliable, and nondestructive method for the measurement of vacuum pressure without specialized equipment. *Appl. Opt.*, 52(25):6195–6200, Sep 2013.
- [89] R. W. G. Moore, L. A. Lee, E. A. Findlay, L. Torralbo-Campo, and D. Cassettari. Measurement of Vacuum Pressure with a Magneto-Optical Trap: a Pressure-Rise Method. *ArXiv e-prints*, January 2014.
- [90] National Institute of Science and Technology. Available online at: [http://www.nist.gov/calibrations/low\\_pressure\\_vacuum\\_leak.cfm](http://www.nist.gov/calibrations/low_pressure_vacuum_leak.cfm), 2014.
- [91] Agilent. SH-100 dry scroll vacuum pump. Manual (Revision A, 2005).
- [92] H. Pang I. Mout, W. Wang. Design of a magneto-optical trapping system. APSC 459 final report, 2010.
- [93] J. Schoser, A. Batär, R. Löw, V. Schweikhard, A. Grabowski, Yu. B. Ovchinnikov, and T. Pfau. Intense source of cold Rb atoms from a pure

## Bibliography

---

- two-dimensional magneto-optical trap. *Phys. Rev. A*, 66:023410, Aug 2002.
- [94] K. Dieckmann, R. J. C. Spreeuw, M. Weidemüller, and J. T. M. Walraven. Two-dimensional magneto-optical trap as a source of slow atoms. *Phys. Rev. A*, 58:3891–3895, Nov 1998.
- [95] Saptarishi Chaudhuri, Sanjukta Roy, and C. S. Unnikrishnan. Realization of an intense cold Rb atomic beam based on a two-dimensional magneto-optical trap: Experiments and comparison with simulations. *Phys. Rev. A*, 74:023406, Aug 2006.
- [96] H. J. Lewandowski, D. M. Harber, D. L. Whitaker, and E. A. Cornell. Simplified system for creating a Bose-Einstein condensate. Internal Publication, 2003.
- [97] T. Zickler. Basic design and engineering of normal-conducting, iron-dominated electromagnets. Internal Publication at CERN, 2009.
- [98] Magnus Haw, Nathan Evetts, Will Gunton, Janelle Van Dongen, James L. Booth, and Kirk W. Madison. Magneto-optical trap loading rate dependence on trap depth and vapor density. *J. Opt. Soc. Am. B*, 29(3):475–483, Mar 2012.
- [99] F. Reif. *Fundamentals of Statistical and Thermal Physics*. McGraw-Hill, New York, 1965.

# Appendix A

## Loading rate investigation

### A.1 Reif model

This appendix describes an investigation of the loading rate of a vapour loaded MOT performed in our lab by Magnus Haw, Nathan Evetts and Dr. James Booth described in [98]. It is included because many of the measurement techniques used in this investigation are described in detail in this thesis. The trap loading rate,  $R$ , for a magneto-optical trap loaded from a vapour can be modeled by what we call the ‘Reif model’ [82, 99]. The Reif model states that any atom entering the trap volume with speed less than the ‘capture velocity’,  $v_c$ , will be cooled and trapped. This model leads to a prediction of loading rate as

$$R = \frac{2Av_c^4 n}{\pi^2 v_{\text{th}}^3} \quad (\text{A.1})$$

where  $v_{\text{th}} = \sqrt{\frac{8k_B T}{\pi m}}$  is the mean thermal velocity of the background particles,  $A$  is the surface area of the trap region, and  $n$  is the background density of the species being trapped. The trapping volume is taken as the region of intersection of the laser beams forming the MOT.

The depth of a trap can be written as  $U = \frac{1}{2}mv_e^2$ , where  $v_e$  is the escape velocity. We make the assumption that the capture velocity is proportional to the escape velocity,  $v_c = bv_e$ . This allows us to write the loading rate,  $R$ , as

$$R = \left( \frac{8b^4 A}{\pi^2 m^2 v_{\text{th}}^3} \right) U^2 n. \quad (\text{A.2})$$

This model had never been tested experimentally and has several attractive features such as relating the loading rate to difficult to find parameters such as  $n$ , and  $U$ . There were four main goals of this work. The first and second were to test that the loading rate,  $R$ , is proportional to  $n$  and to  $U^2$  as predicted in Eq. A.2. The third goal involves a determination of trap depth for different settings of MOT pump detuning and intensity based on knowledge of the trap depth for one particular pump detuning and intensity

setting. The fourth goal of this work was to estimate the proportionality constant,  $b$ , between the escape and capture velocity.

## A.2 Experimental observables

As seen previously in section 3.2.1, a portion of the photons being emitted by the atoms in a MOT can be collected onto a photodetector. The voltage output by the photodetector,  $V(t)$ , will be proportional to the number of atoms in the trap,  $N(t)$ . Specifically,

$$V(t) = \alpha\gamma_{sc}N(t). \quad (\text{A.3})$$

$\gamma_{sc}$  is the rate at which an atom scatters photons and depends on the detuning and the intensity of the light.  $\alpha$  is the proportionality constant between the number of photons emitted per second by the trapped atoms and the photodiode voltage produced, and can be expressed as  $\alpha = \frac{hc}{\lambda}(\frac{r^2}{4d^2})\epsilon\eta$ . The factor  $\eta$  is the optical power to voltage conversion factor of the photodiode.  $\epsilon$  describes the transmission of the glass and lens which the photons travel through to arrive at the photodetector.  $r$  is the radius of the lens that focuses the fluorescent light onto the photodetector.  $d$  is the distance from the trapped atoms to the lens. The ratio  $(\frac{r^2}{4d^2})$  involving  $r$  and  $d$  accounts for the solid angle of photons that are collected onto the detector.

The loading rate equation of a MOT is usually modelled as (see Eq. 1.5 in section 1.3)

$$\frac{dN}{dt} = R - \Gamma N - \beta \int n^2(\vec{r}, t) d^3\vec{r}. \quad (\text{A.4})$$

This work focuses on the loading rate of the MOT,  $R$ . For short times from initial loading the number of atoms trapped is very small so that one can approximate

$$\frac{dN}{dt}|_0 = R. \quad (\text{A.5})$$

In terms of photodetector voltage Eq. A.5 becomes

$$\frac{dV}{dt}|_0 = \dot{V}_0 = \alpha\gamma_{sc}R \quad (\text{A.6})$$

where  $\dot{V}_0$  is the rate of change of  $V$  for small times after the initial turn on of the MOT.  $\dot{V}_0$  is proportional to  $R$  which changes with different MOT settings, such as different pump light detunings and intensities, different geometries (e.g. beam sizes), and background gas density.

To eliminate uncertainties in the quantities  $\alpha$  and  $\gamma_{sc}$ , we define a new experimental parameter

$$M_i = \left( \frac{V_{std}}{V_i} \right) \dot{V}_0^i \quad (\text{A.7})$$

where  $V_i$  is the steady state voltage when the MOT is fully loaded with settings  $i$ .  $V_{std}$  is taken by switching quickly from MOT setting  $i$  to some pre-selected ‘standard’ setting. The voltage immediately after the switch,  $V_{std}$ , is recorded before the atom number has had time to change.  $\dot{V}_0^i$  is the voltage rise after initial turn on for MOT setting  $i$ . Using the fact that the atom number is the same for  $V_i$  and  $V_{std}$ , Eq. A.3 gives

$$\frac{V_{std}}{V_i} = \frac{\gamma_{sc}^{std}}{\gamma_{sc}^i}. \quad (\text{A.8})$$

Substitution of Eq. A.8 and Eq. A.6 into Eq. A.7 gives

$$M_i = \left( \frac{V_{std}}{V_i} \right) \dot{V}_0^i = \frac{\gamma_{sc}^{std}}{\gamma_{sc}^i} (\alpha \gamma_{sc}^i R_i) = \alpha \gamma_{sc}^{std} R_i \quad (\text{A.9})$$

so that  $M_i \propto R_i$  with the same proportionality constant for different MOT settings  $i$ .

The MOT apparatus used was the same one described in section 3.1.  $^{85}\text{Rb}$  was used as the trapped species. The total standard six beam pump power was 18.3 mW and 0.56 mW for the repump. The beams had a  $1/e^2$  horizontal (vertical) diameter of 7.4 (8.4) mm. This corresponds to a pump intensity of 37.5 mW cm<sup>-2</sup>. The MOT was operated with an axial gradient of 27.9(0.3) G/cm ( $2.79(0.03) \times 10^{-3}$ ) T/cm. This maximum pump intensity and a 12 MHz pump detuning was used as the standard MOT setting.

### A.3 The dependence of loading rate on MOT trap depth

To determine if the loading rate,  $R$ , is proportional to  $U^2$  measurements of  $M_i$  were taken for various MOT settings,  $i$ .  $U_i$  were measured independently for the various MOT settings via the catalysis method described in section 3.3. The results, shown in Fig. A.1, support a linear relationship between  $M_i \propto R_i$  and  $U_i^2$ . Table A.1 gives the measured values of trap depth for various MOT pump detunings and intensities.

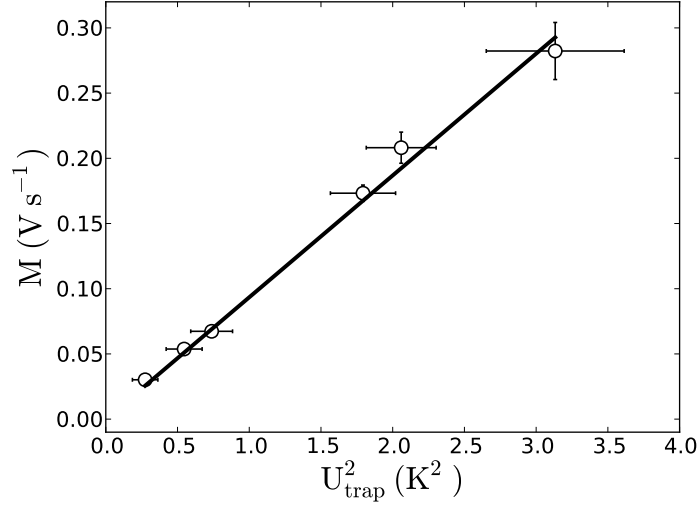


Figure A.1: Evidence that the loading rate of a MOT is proportional to the square of trap depth. The quantity  $M_i$  for different MOT settings  $i$  is proportional to the loading rate  $R_i$ . Plotting  $M_i$  versus the trap depth of each MOT setting  $U_i^2$  indicates a linear relationship.

#### A.4 Trap depth determination using loading rates

It is proposed that the trap depth for different settings of MOT pump detuning and intensity can be determined based on knowledge of the trap depth for one particular pump detuning and intensity setting. The approach for this goal makes several assumptions. The surface area of the trap region is assumed to stay the same for different MOT pump detuning and intensity settings. It is also assumed that the proportionality constant,  $b$ , between  $v_c$  and  $v_e$  stays the same for different settings. Finally it is assumed that the background density,  $n$ , also is a constant. With these assumptions the ratio of Eq. A.2 for two different MOT settings gives

$$U_2 = U_1 \sqrt{\frac{R_2}{R_1}}. \quad (\text{A.10})$$

To determine the trap depth of MOT setting 2, a measurement of the ratio of loading rates for setting 2 and another setting 1 is needed. The additional

Table A.1: MOT trap depths measured using the ‘catalysis method’ for various MOT settings.

Pump Detuning (MHz)	Pump Intensity (mW cm <sup>-2</sup> )	$U$ (K)
-5	2.9	0.52 (0.12)
-8	2.9	0.74 (0.12)
-10	2.9	0.86 (0.12)
-12	7.5	1.34 (0.12)
-12	10.4	1.44 (0.12)
-12	37.5	1.77 (0.19)

knowledge of the trap depth for setting 1 provides the trap depth,  $U_2$ .

Using measurements of  $M_1$  and  $M_2$  for two MOT settings and a catalysis measurement of trap depth for setting 1 we can find the trap depth for MOT setting 2 using

$$U_2 = U_1 \sqrt{\frac{R_2}{R_1}} = U_1 \sqrt{\frac{M_2}{M_1}}. \quad (\text{A.11})$$

Fig A.2 shows agreement between the predicted trap depth,  $U_{\text{pred}}$ , determined from Eq. A.11 and the measured trap depth,  $U_{\text{meas}}$ , from the catalysis method, also given in table A.1.

Note that one should not extrapolate this trap depth determination for a MOT too far from the known trap depth.

## A.5 The dependence of loading rate on rubidium density

To show that  $R_i$  is proportional to  $n_{\text{Rb}}$  we show  $M_i \propto n_{\text{Rb}}$ . To do this we measure the loss rate constant,  $\Gamma_{\text{MT}}$ , due to background collisions between the background gas and the trapped Rb atoms in a magnetic trap. The  $|F = 2, m_F = -2\rangle$  state was used for the  $5^2S_{1/2}$  ground state of  $^{85}\text{Rb}$ . As described previously in chapter 2,  $\Gamma_{\text{MT}}$  can be expressed as

$$\Gamma_{\text{MT}} = \sum_j n_j \langle \sigma v_j \rangle_{\text{Rb},j} \quad (\text{A.12})$$

where  $n_j$  is the density of background species  $j$ . The term  $\langle \sigma v_j \rangle_{\text{Rb},j}$  is the velocity averaged collisional loss cross section between the trapped Rb and background species  $j$ . Isolating the dependence of  $\Gamma_{\text{MT}}$  on the background

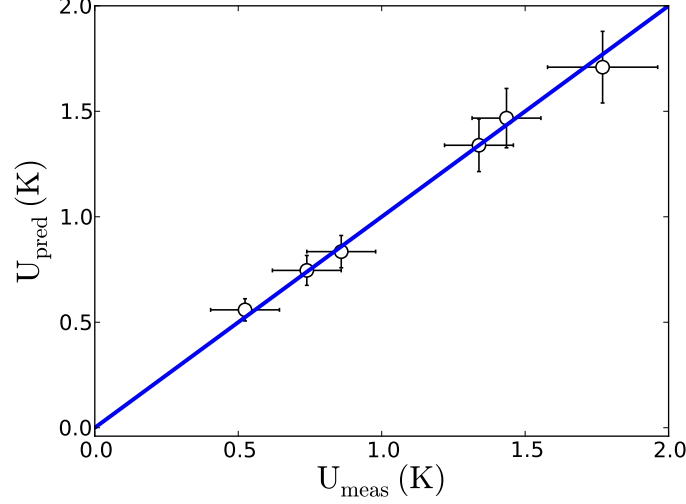


Figure A.2: MOT trap depth is predicted based on the ratio of loading rates and the knowledge of a comparison trap depth. The predicted trap depth for various MOT settings is plotted versus the measured trap depths showing good agreement between the two.

density of Rb,  $n_{\text{Rb}}$ , we have

$$\Gamma_{\text{MT}} = n_{\text{Rb}} \langle \sigma v_{\text{Rb}} \rangle_{\text{Rb,Rb}} + \Gamma_a \quad (\text{A.13})$$

where  $\Gamma_a$  is the contribution to  $\Gamma_{\text{MT}}$  due to background species other than Rb.

From Eq. A.2 and Eq. A.9 our model states  $M_i = k_i n_{\text{Rb}}$  where  $k_i$  is a proportionality constant. Rearranged slightly we have  $n_{\text{Rb}} = \frac{M_i}{k_i}$  and inserting this into Eq. A.13 gives

$$\Gamma_{\text{MT}} = \frac{M_i}{k_i} \langle \sigma v_{\text{Rb}} \rangle_{\text{Rb,Rb}} + \Gamma_a. \quad (\text{A.14})$$

Measurements of  $\Gamma_{\text{MT}}$  in a magnetic trap and  $M_i$  for one particular MOT setting,  $i$ , at various Rb densities should give a linear relationship for  $\Gamma_{\text{MT}}$  versus  $M_i$ . The MOT setting,  $i$ , chosen was the standard setting. The Rb density was varied by filling the MOT region by running current through a Rb dispenser and then letting the density decay over time.  $\Gamma_{\text{MT}}$  was

## Appendix A. Loading rate investigation

---

measured as described in section 3.2.2.  $M_{\text{std}}$  for the standard MOT setting was also measured at the same time. Fig. A.3 shows the results and verifies that  $M_{\text{std}} \propto n_{\text{Rb}}$  so that  $R_{\text{std}} \propto n_{\text{Rb}}$ .

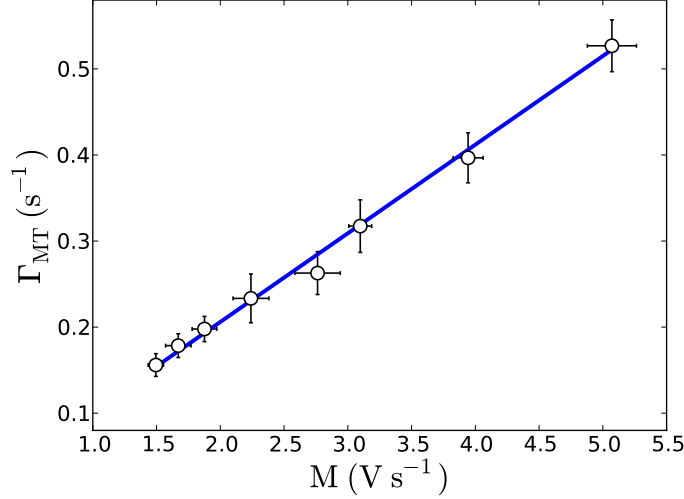


Figure A.3: Evidence that the loading rate of a vapour loaded Rb MOT is proportional to the background density of Rb,  $n_{\text{Rb}}$ . The loss rate constant of a magnetic trap,  $\Gamma_{\text{MT}}$ , varies linearly with Rb background density. If the measure  $M$ , which is proportional to the loading rate of a MOT, is also proportional to the Rb background density then  $\Gamma_{\text{MT}}$  will vary linearly with  $M$ . For this measurement the ‘standard’ setting of the MOT was used for  $M$ .

### A.6 Determination of $b$

The last part of this investigation is to determine the proportionality constant  $b$ . Using Eq. A.2 and Eq. A.9 and dividing by the background rubidium density,  $n_{\text{Rb}}$ , we have

$$\frac{M_i}{n_{\text{Rb}}} = \alpha \gamma_{\text{sc}}^{\text{std}} \frac{R_i}{n_{\text{Rb}}} = \alpha \gamma_{\text{sc}}^{\text{std}} \left( \frac{8b^4 A}{\pi^2 m^2 v_{\text{th}}^3} \right) U_i^2. \quad (\text{A.15})$$

## Appendix A. Loading rate investigation

---

This equation predicts that  $\frac{M_i}{n_{\text{Rb}}}$  should be linearly related to  $U_i^2$  with a slope from which  $b$  can be extracted.

To obtain  $\frac{M_i}{n_{\text{Rb}}}$  for different settings  $i$ ,  $M_i$  was measured as the density of rubidium changed. The MOT region was filled with Rb vapour. As the density of Rb was slowly decreasing from initial filling,  $\Gamma_{\text{MT}}$  for a magnetic trap was measured.  $M_{\text{std}}$  and  $M_i$  was also measured for various MOT settings as the density of Rb changed.

To determine the Rb densities, a plot of  $\Gamma_{\text{MT}}$  versus  $M_{\text{std}}$  was used. The slope is  $\frac{\langle \sigma v_{\text{Rb}} \rangle_{\text{Rb,Rb}}}{k_{\text{std}}}$  where  $M_{\text{std}} = k_{\text{std}} n_{\text{Rb}}$ . If  $\langle \sigma v_{\text{Rb}} \rangle_{\text{Rb,Rb}}$  is calculated, as described in chapter 2, then  $k_{\text{std}}$  can be determined and measurement of  $M_{\text{std}}$  provides the density of rubidium.  $M_{\text{std}}$  as a function of time as the Rb density decreased was fit so that  $n_{\text{Rb}}$  could be determined when each  $M_i$  measurement was made.

Fig. A.4 shows a plot of  $M_i$  vs  $n_{\text{Rb}}$ . The slopes of these plots are  $E_i = \frac{M_i}{n_{\text{Rb}}}$  which can be plotted versus  $U_i^2$  as shown in Fig. A.5. The slope of the plot in Fig. A.5 allows  $b$  to be estimated from Eq. A.15.

To determine  $b$  the values of  $\alpha$  and  $\gamma_{\text{sc}}^{\text{std}}$  are determined as described in section 6.2. The value of  $A$  was estimated as the surface area of the intersection of three perpendicular cylinders,  $A = 3(16 - 8\sqrt{2})r^2$ , where  $r$  is the laser beam radius averaged across the horizontal and vertical directions. The factor  $\frac{8}{\pi^2 m^2 v_{\text{th}}^3}$  was computed for  $^{85}\text{Rb}$  vapour of temperature  $T = 300$  K. Table A.2 gives the calculated values for all these quantities. From the

Table A.2: Parameters used in the calculation of  $b$ , the proportionality constant between the capture velocity  $v_c$  and the escape velocity  $v_e$ .

Parameter	Value	Uncertainty
A	2.08 cm <sup>2</sup>	10 %
$\alpha = \frac{(r_{\text{lens}})^2}{4(d_{\text{MOT}})^2} \eta \frac{hc}{\lambda} \epsilon$	$7.84 \times 10^{-15}$ V s	20 %
$\gamma_{\text{sc}}^{\text{std}} = \frac{\Gamma}{2} \left( \frac{s}{1+s+(\frac{2\delta}{\Gamma})^2} \right)$	$6.8 \times 10^6$ s <sup>-1</sup>	20 %
$\frac{8}{\pi^2 m^2 v_{\text{th}}^3}$	$3.85 \times 10^{-2}$ $\frac{\text{cm}}{\text{K}^2 \text{s}}$	5 %

quantities given in Table A.2 the proportionality constant  $b$  was determined. The relationship between the capture velocity,  $v_c$ , and the escape velocity,  $v_e$ , was found to be

$$v_c = 1.29(0.12)v_e. \tag{A.16}$$

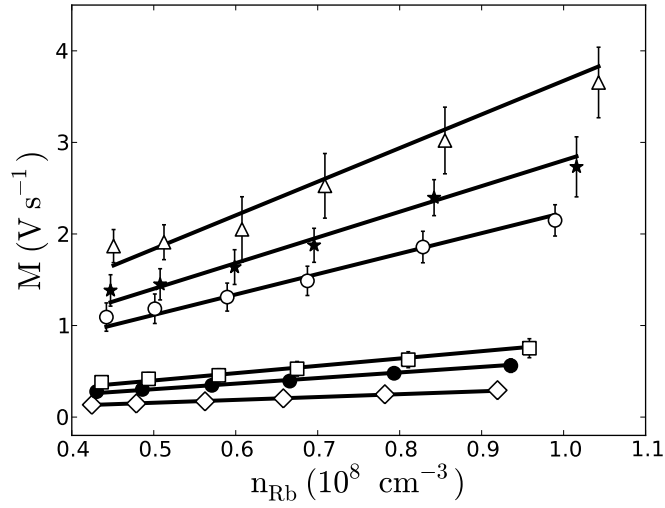


Figure A.4: Measurement of  $M_i$  for various MOT settings,  $i$ , versus the density of background gas,  $n_{\text{Rb}}$ . The slopes should be linearly related to the trap depth squared for the different MOT settings. The density of Rb was determined by measurement of the loss rate constant of a magnetic trap, measurement of  $M_{\text{std}}$ , and calculation of the velocity averaged collisional loss cross section,  $\langle \sigma v_{\text{Rb}} \rangle_{\text{Rb,Rb}}$ .

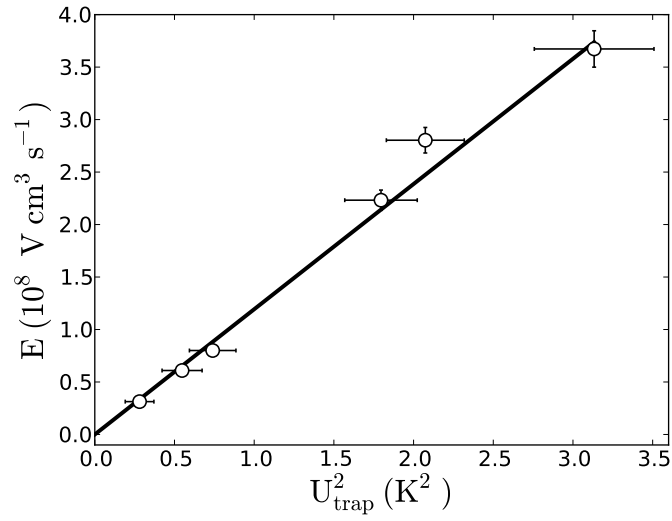


Figure A.5: A plot of  $\frac{M_i}{n_{\text{RB}}}$  versus  $U_i^2$ . The proportionality constant,  $b$ , between the capture and escape velocity can be extracted from the slope with the estimation of various coefficients.